2003

Dynamic and thermal circulations over the Tharsis region on Mars

Magdalena Rosario V Sta. Maria
San Jose State University

NOTE TO USERS

DYNAMIC AND THERMAL CIRCULATIONS OVER THE THARSIS REGION ON MARS

A Thesis

Presented to

The Faculty of the Department of Meteorology

San Jose State University

In Partial Fulfillment

of the Requirements for the Degree

Master of Science

by

Magdalena Rosario V. Sta. Maria

May 2003

ProQuest Information and Learning Company
300 North Zeeb Road
P.O. Box 1346
Ann Arbor, MI 48106-1346

APPROVED FOR THE DEPARTMENT OF METEOROLOGY

Alison F. C. Bridger

Dr. Alison Bridger

Eugene Cordero

Dr. Eugene Cordero

Robert M Haberle

Dr. Robert Haberle, NASA Ames Research Center

Scot Rafkin

Dr. Scot Rafkin, Southwest Research Institute

APPROVED FOR THE UNIVERSITY

ABSTRACT

DYNAMIC AND THERMAL CIRCULATIONS
OVER THE THARSIS REGION ON MARS

by Magdalena Rosario V. Sta. Maria

The Tharsis region on Mars, having some of the most complex terrain on the planet, is rife with small-scale atmospheric phenomena. Images from Viking orbiter and Mars Global Surveyor reveal afternoon cap clouds over Tharsis volcanoes, bore wave-like clouds, and wind streaks, among others. The effect of the extreme topography on the small-scale circulations, and its potential impact on the large-scale, is examined with emphasis on wind streak formation, bore wave phenomena, and thermal circulations.

The study shows that daytime thermal circulations are a possible major daily source of atmospheric dust loading and maintenance. Predicted cold spots over volcanoes during the daytime may be associated with the observed cap clouds. Nighttime downslope flows generate bore waves and results indicate a seasonality to their occurrence. Wind streak studies reveal high correlations to observations in certain regions, though results imply more complicated processes involved in streak formation than is currently thought.

ACKNOWLEDGMENTS

I would like to express my deepest gratitude to the people who have contributed to the completion of this thesis: Dr. Scot Rafkin for invaluable guidance, tireless patience, and the opportunity to learn about a whole new world; Mr. Timothy Michaels for enlightening discussions and valuable suggestions; Dr. Robert Haberle (NASA ARC) and Dr. Alison Bridger for valuable input and recommendations; Dr. Eugene Cordero for helpful recommendations and agreeing to be on my committee at the last minute; Dr. Bruce Cantor (MSSS) for graciously answering all my questions regarding MOC images; and to all the members of the Meteorology department at San Jose State University – faculty, staff, and students – who have, in one way or another, helped me make it this far. I would also like to thank my family for their unfailing support and prayers.

This work was supported by the NASA Planetary Atmosphere Program Grant NAG5-9571 and the NASA Mars Data Analysis Program

TABLE OF CONTENTS

LIST OF FIGURES

1. Introduction

The climate of Mars has always been studied based on the basis that it is fundamentally similar to Earth climate and that examining the differences between the two planets will lead to a better understanding of Earth. Mars atmosphere quickly gained a character all its own, however, with a much thinner atmosphere (average surface pressure on Mars is 6.11 Pa versus 10^5 Pa on Earth), low surface temperatures ranging from about 140 K to 300 K, and considerably less water than on Earth. The significance of Mars atmospheric studies soon expanded from examining its implications for Earth to understanding both the past and present climates of Mars itself. Among the most interesting subjects are the small-scale circulations forced by the extreme topography found on the planet.

Some of the most complex topography on Mars can be seen in the Tharsis region (See Fig. 1 in the back). Four of the largest volcanoes are found here. The system of three volcanoes in the east of the region is called the Tharsis Montes. This extreme terrain has a large impact on local atmospheric circulations and may also affect large-scale circulations. Atmospheric phenomena on the order of tens of kilometers to hundreds of meters, generally classified as mesoscale phenomena, have been imaged in the Tharsis region. For example, the Mars Global Surveryor (MGS) (Albee 2002) Mars Orbiting Camera (MOC) (Sandoval *et al.* 2000) and Viking (Young 1978) images reveal afternoon cloud tops over the Tharsis volcanoes, bore waves along the volcano slopes, localized dust storms, cloud streets, and wind streaks (e.g., Hunt *et al.* 1981; Kahn and Gierasch 1982; Pickersgill 1984; Malin 1998; MSSS 2001). Many of these phenomena are be-

lieved to be forced by complex topography and variations in surface thermal characteristics, such as thermal inertia and albedo. At present, these phenomena are poorly understood. Mars global circulations models (MGCMs) do not adequately spatially resolve these forcing mechanisms, and cannot reproduce or resolve these small-scale phenomena. The goal of this thesis is to simulate and study the processes involved in some of these meteorological phenomena, as well as to determine the role extreme topography plays in forcing small and large-scale circulations. Using a mesoscale model, this study will focus on the wind streaks, atmospheric bores and thermal circulations of the Tharsis region.

1.1 Significance of Study

The Mariner 9 orbiter (Snyder and Moroz 1992) was the first to image atmospheric phenomena associated with localized forcing (e.g., local dust storms, wind streaks, etc.) (Zurek 1992). It was the first indication that the Martian atmosphere was active in the mesoscale. Until recently, the martian atmosphere has been studied mostly using Mars global circulations models (MGCMs). These models simulate large-scale circulations (on the order of hundreds of kilometers) over the entire planet and have time scales of a season or more. They are usually run at horizontal grid spacings of a few degrees. This large grid spacing is sufficient for general circulation studies and capturing the essential features of the Martian climate. The grid spacing is not sufficient, however, to fully capture the more localized forcing mechanisms, such as those associated with steep topography and rapid variations in surface thermal characteristics, that drive these observed mesoscale phenomena.

Aside from the large grid resolution, MGCMs assume a hydrostatic atmosphere to simplify computations. Circulations with large accelerations of vertical wind, such as large amplitude non-hydrostatic mountain waves, cannot be properly simulated. Several observed phenomena on Tharsis are associated with its extreme topography and MGCMs are not capable of fully capturing the processes forced by the volcanoes.

A typical mesoscale model has both the capacity for higher resolution and the ability to reproduce these non-hydrostatic circulations. Being able to more properly represent these small scale-forcing mechanisms will aid in understanding the dynamics involved in the development of the observed phenomena. This study will focus on the mechanisms that take place in bore wave and wind streak formation, as well as the thermal circulations driven by the Tharsis volcanoes. A better understanding of these processes will not only be an important contribution to the existing body of knowledge on the Martian atmosphere, but will also aid in the planning of future missions to the Red Planet.

1.2 Previous Research

1.2.1 Wind Streaks

Close-up images of the martian surface by Mariner 9, the Viking Orbiters, and most recently by MOC revealed linear albedo variations related to topographic barriers (Sagan *et al.* 1972; Thomas and Veverka 1979; Thomas *et al.* 1981). Termed "wind streaks" (Sagan et al. 1972), the shape and orientations of these markings suggest formation through aeolian processes (Fig. 2).

Wind streaks come in a wide variety of shapes and sizes and are associated with different kinds of topographic obstacles, such as craters, scarps and ridges. Thomas *et al.* (1981) proposed a classification of four types based on hypothesized formation mechanisms: 1) Type I(b), or bright streaks, 2) Type I(d), or dark streaks, 3) Type I(m), mixed-tone streaks, and 4) Type II streaks, which are also dark but believed to form by a different mechanism from Type I(d). All Type I streaks usually form on the lee side of an obstacle (Thomas *et al.* 1981, Lee et al 1982). Streaks are believed to be formed by one or more processes: deposition, erosion or deflation.

Deposition occurs when bright dust or sand suspended in the atmosphere is preferentially deposited on a darker surface in the lee of an obstacle. Type I(b) streaks are interpreted to be depositional streaks, created from suspended, bright dust particles – surplus perhaps from the last dust storm – that preferentially settle downwind of a topographic barrier. Bright streaks that are not clearly associated with any obstacles are commonly called I(b) sheet streaks.

Erosion involves the removal of a thin layer of the surface dust or sand by turbulence caused by flow over an obstacle, revealing an either brighter or darker substrate beneath. Type I(d) streaks are possibly erosional, formed by wind accelerating in the lee of a crater and eroding away the topmost layer of dust on the ground, exposing darker material beneath. Those that are not obviously related to topographic barriers are called I(d) coalesced streaks. Streaks falling under the classifications of I(b) and I(d) are the most studied, as they are the most common (see Fig. 3). Type I(m) streaks have been speculated to be a combination of Types I(b) and I(d), although the bright and dark parts of the

streak may have been formed at different times and under different meteorological conditions.

The third formation mechanism requires the deflation of wind-transportable dust or sand from an existing deposit contained in a depression. This deflation leaves a trail that forms the streak. This process differs from deposition in that the streaks formed by deflation have an identifiable ground source, whereas depositional streaks result from preferential sedimentation of the local background dust from the atmosphere. Streaks thought to form by the deflation of dark material are classifed as Type II.

For dust to be deflated from a deposit, or eroded away, dust must be lifted away from the surface. The mechanism for dust lifting is the generation of high surface stresses. Dust may be lifted once a stress threshold has been reached. Surface stresses are related to turbulence nearest the surface. Turbulence can be generated both by strong vertical wind shear and buoyancy forces (through buoyancy gradients). High wind shear can be generated by strong winds passing over a raised obstacle (e.g., ridges, or a crater rim). Buoyancy gradients form by thermal stratification near the surface. During the day, when the atmosphere is typically unstable, both buoyancy forces and wind shear contribute to the creation of surface stress. At night, high stability prevents buoyancy forces to generate turbulence. Thus, shear due to frictional interaction between the surface and the winds nearest the ground control the magnitude of surface stress.

Once a particle gets into the air, it can cause the ejection of other particles still on the ground through saltation. Saltation is a process wherein an already airborne particle impacts other stationary particles still on the surface causing the struck particles to be

ejected into the air, thus providing a feedback process (Bagnold 1941). The Viking landers provided evidence that saltation occurred on another planet other than Earth, and was a mechanism for particle motion (Sagan *et al.* 1977). The already airborne particles can either settle back down to the surface, or get transported in suspension by turbulence and wind.

There are few details on the specific meteorological conditions needed for streak formation. One hypothesis by Veverka et al (1981) suggests that atmospheric static stability and wind speeds are factors that determine the primary formation mechanism. The importance of static stability and wind speed is expressed by the ratio,

$$r = \frac{N^2 lh}{U^2} \tag{1}$$

where N is the Brunt Vaisalla frequency (s^{-1}), l is the half-width of the obstacle (see Fig. 4), h is the obstacle height, and U is wind speed (m/s). This ratio expresses the potential of an obstacle to block the flow of air. When $r < 1.0$, the wind has enough inertia to stream over the obstacle (e.g., kinetic energy, characterized by U^2, is greater than potential energy, N^2lh). When $r \geq 1.0$, the wind is blocked by the obstacle and is forced to flow around it, forming a pocket of relatively weak winds downwind. This condition is conducive for dust suspended in the air to settle behind the obstacle. Thus, according to this theory, depositional streaks form with high stability, and low, unidirectional wind speeds. In addition to the dynamical requirements, high dust opacities are also needed to supply the dust that is deposited. Some studies (e.g., Martin and Kieffer 1979; Conrath *et al.* 1973) predict that bright streaks form during global duststorms, when stability and dust opacities are high. In contrast, Veverka *et al.* (1981) argued that low stability and high

winds were required for the formation of dark streaks. Wind flowing over an obstacle could accelerate on the downslope side, increasing surface stress enough to perhaps be sufficient to cause erosion. Dark streaks were proposed to form before and after global duststorms when more solar radiation reaches the surface, thereby largely decreasing stability at a time when a veneer of dust is available for removal. The Veverka *et al.* hypothesis involves relatively simple processes and fails to take into consideration the full range of dynamic processes.

An opposing theory on the formation of dark streaks proposes that high stability is needed for the dust clearing (Magalhaes *et al.* 1982; Fenton and Richardson 2001). High stability coupled with strong winds over the obstacle can cause downslope windstorms in the lee of the obstacle, resulting in possible saltation and erosion. As wind flows over an obstacle, the high stability limits the rising motion of the air and forces it to flow back down the opposite side of the obstacle (Fenton and Richardson 2001). This scenario is most likely to occur during the night. During the day, the unstable atmosphere would permit air forced upward by an obstacle to continue rising and never reach the opposite side of the obstacle.

Streak types vary temporally. Type I(d) is the most variable, being observed to change over a relatively short period of time (Veverka 1975; Sagan *et al.* 1972, 1973) (see Fig. 5). Sagan *et al.* (1972) found dark streaks to be variable on a time scale of 38 days. Veverka (1975) stated that Type I(d) streaks were indeed formed by erosion on the basis of these observations. Dark streaks have been seen to appear after the large 1971 duststorm; the layer eroded away may have come from the duststorm fallout. Malin and

Cantor (2002) also observed rapidly evolving dark streaks on a dust-brightened Syrtis Major after the 2001 major duststorm.

Changes in Type I(b) streaks, although relatively rare, have been observed in the Syria Planum region and on the eastern flanks of the Tharsis Montes (Thomas and Veverka 1979). Some of these changes include the disappearance of long (on the order of 100 km), straight bright streaks, and the appearance of smaller crater-associated streaks. It was noted, however, that the overall wind patterns indicated by the streak orientations were virtually unchanged. Most of these changes occurred during a sequence of dust storms (Peterfreund 1981). Otherwise, bright streaks are known to be extremely stable. Type II streaks have also shown changes (Thomas and Veverka 1979; Thomas *et al.* 1981; Peterfreund 1981) although most of the variability was detected between the Mariner 9 and Viking missions. Increases in streak length and changes in the streak margins were observed. Irregular changes have also been seen following dust storms. These streaks, however, remained relatively stable during the latter part of the Viking Orbiter coverage. The variability of these streaks was found to be mostly secular rather than seasonal.

Variable streaks are found mostly at elevations above that corresponding to the global average surface pressure. They are also near, or on regions with strong surface thermal gradients, i.e., places with variable surface albedo and thermal inertia, which are conducive for generating strong local surface winds (Peterfreund 1981).

All the streaks are strongly latitude-dependent. Most of the streaks are confined to within ±60° (Thomas *et al.* 1981; Thomas *et al.* 1984; Peterfreund 1981). Bright

streaks are found scattered around the 40°N-30°S latitude range. Type II streaks are found at 20°N to 5°S, and 40°S to 65°S. Type I(d) streaks are mostly within two latitude belts: 10-40°S and 10-30°N. Most Type I(d) streaks are observed on regions with significant slopes and areas where dust storms are observed to originate.

Theoretical studies on the strength of slope winds, as well as effects of downslope windstorms, suggest that slope winds generate enough surface stress to lift dust (Magalhaes and Young 1995; Magalhaes and Gierasch 1982; Thomas *et al.* 1984). Several dark streaks interpreted as being oriented downslope were found on volcano slopes on Tharsis (Lee *et al.* 1982) (see Fig. 6). These are believed to be streaks eroded by nighttime katabatic winds.

Greeley *et al.* (1993, 1999, 2000) reported on theoretical and numerical experiments designed to investigate factors necessary for streak formation. Greeley *et al.* (1993) compared wind streak features with results from the NASA-Ames Mars general circulation model (MGCM). Surface stress vectors predicted by the MGCM were compared with azimuths of the wind features. It was found that during southern hemisphere summer, the stress vectors were largely well correlated with bright streak orientations. In contrast, correlation for dark dust streak orientation was low, although areas of high stresses matched locations of dark streaks, partially supporting the erosion theory for Type I(d) streaks. Also noteworthy is that although bright streaks in the Mars Pathfinder landing site matched up with MGCM results, other geologic features such as ventifacts – erosion marks on rocks – did not correlate well with the MGCM (Greeley *et al.* 1999).

This gave rise to the theory that the ventifacts at Pathfinder were formed during a period of a different wind regime on Mars (Greeley *et al.* 2000).

Greeley *et al.* (1980) also performed wind tunnel experiments to measure the saltation thresholds for dust and sand. It was found that at 5 hPa, friction velocity thresholds ranged from approximately 2 m s^{-1} to 5 m s^{-1}, depending on the particle size. Figure 7 summarizes the association of thresholds to particle sizes. Another wind tunnel study by Greeley *et al.* (1974) suggested that some crater-related light streaks are formed by deposition. They also showed that erosion caused dark zones to form behind a crater.

Observational studies of the correlations between albedo, thermal inertia, latitude, elevation, and topography in and around the streaks have been carried out (e.g., Peterfreund 1981; Thomas *et al.* 1984; Bridges 1994; Pelkey 2001). They used thermal inertia and albedo data, derived from Viking color images, Viking Infrared Thermal Mapper (IRTM), and the Mars Global Surveyor Thermal Emission Spectrometer (TES), were used to obtain the average particle sizes in the streak, as well as its surroundings, and to infer the transport and deposition processes involved in streak formation. The results showed that the material in both Type I(b) and Type I(d) streaks were thermally indistinct from their surroundings, which suggests that for Type I(b) streaks, the veneer of dust at the lee of the crater is too thin (less than 1-3 mm) to be thermally distinguished from the material beneath, but thick enough to change the albedo. Moreover, for Type I(d), the lack of thermal differences seemed to imply that there is a thin layer of material that thermally masks the darker underlying surface, but which is similar to the streak's sur-

roundings. These studies were not conclusive in terms of determining the mechanisms involved in formation.

On the other hand, Type II(d) streaks were found to be distinct, both optically and thermally, from their surroundings, with the layer of streak material thicker than approximately one centimeter. Thermal properties implied sand-sized (~80-900 microns) particles. Both the distinctive thermal characteristics and the particle size range support the theory that Type II(d) streaks form from the deflation of deposits within depressions, via saltation and short-term suspension.

In summary, several issues remain unresolved on the subject of streak formation. Two different hypotheses are suggested in the formation of Type I(d) streaks, and previous numerical simulations were unable to find a good correlation between their results and the observed dark streaks. The current formation hypotheses are relatively simple and, in regions where the slopes are large, other dynamic processes may come into play. These discrepancies and uncertainties are among the motivations for this research.

1.2.2 Bore Wave System

Long wave clouds presumed to be associated with atmospheric bore wave phenomena were observed by the Viking imaging system on the Tharsis plateau during the early morning (Hunt *et al.* 1980, 1981; Pickersgill 1984; Evans 1980; Kahn and Gierasch 1982). These clouds were seen along the flanks and in the saddle between volcanoes. Among the places they were observed were northwest of Pavonis Mons, east of Arsia Mons between Pavonis and Ascreus Mons, south of Olympus Mons, and southwest of Arsia (Kahn and Gierasch 1982). The most defined, however, was seen

Arsia (Kahn and Gierasch 1982). The most defined, however, was seen between Pavonis and Arsia Mons (see Fig. 8). These clouds were most evident between the late spring and early summer during the two martian years that Viking was orbiting Mars.

Martian seasons are specified based on the areocentric longitude of the sun, and are expressed as "L_s". $L_s = 0°$ or 360° corresponds to northern spring equinox, and L_s = 180° is northern fall (each season has a length of 90°). In this case, the clouds were seen specifically at L_s =69.8°-121.5° for the first year, and L_s = 33.6°-121.5° the second year.

Atmospheric bores are a type of solitary wave that transfers mass and propagates along a low-level temperature inversion. They are generated by density currents such as when a fluid moves through the bottom of another, less dense fluid (Rottman and Simpson 1989; Simpson 1997; Crook and Miller 1985). An idealized schematic of a bore is shown in Fig. 9. The bore begins as a smooth hump at the head of the density current. As the bore develops, it moves ahead of the gravity current, taking some of the denser fluid along with it. A new hump develops around the new gravity current head, and the process repeats itself. The result is a series of wave-like oscillations transporting both energy and mass away from the gravity current (Rottman and Simpson 1989; Hollyer and Huppert 1980). More intense bores are characterized by breaking waves at the leading edge (Simpson 1997). A bore's strength can be assessed by the ratio, $a = h_1/h_0$, where h_1 is the mean height of the bore, and h_0 is the height of the interface. When $1 < a < 2$, there is no turbulence and the bore is smoothly undular in form (see Fig. 10a). There is little or no mixing between the two fluids. If $2 < a < 4$, the bore, although still roughly undular, shows some turbulence downstream of the first wave and some mixing occurs (Fig. 10b).

When $a > 4$, turbulence dominates, wiping out further undulations upstream (Fig. 10c). The first kind of bore is called an undular bore, while the third kind is a turbulent bore (Locatelli, *et al.* 1998). Observations of the wave train clouds in the saddle of Arsia and Pavonis appear to be undular with wavelengths between 10 to 20 kilometers (Pickersgill 1984; Kahn and Gierasch 1982).

The behavior of undular bores ($1 < a < 2$) can be predicted by the classical two-layer theory for non-mixing bores, described by the equation

$$F_0^{\,2} = \frac{1}{2}\frac{h_1}{h_0}\left(1 + \frac{h_1}{h_0}\right) \tag{2}$$

where F_0 is the Froude number and is related to the propagation speed of the disturbance. Undular bores are observed to propagate ahead of the density current that generates them, taking some of the denser air and transporting it away from the current head. When there is mixing, i.e., $a > 2$, the behavior of a bore approaches that of a gravity current. Turbulent bores ($a > 4$) do not appear any different from density currents.

The generation of a bore from a density current is determined by the relative densities and heights of the current and the layer of fluid that the current flows into (Simpson 1997). The advancing front of dense fluid acts like a solid obstacle, and the resulting flow pattern becomes either supercritical, subcritical, partially blocked or completely blocked. If the height of the density current is small compared to that of the layer, the effect produced is only a simple displacement upward (as the current head passes through), or downward. A displacement upward corresponds to supercritical flow, while downward displacement is associated with subcritical flow. Bores are usually generated

when the flow is partially blocked. This occurs when the height of the obstacle approaches the depth of the layer, where the flow above the obstacle is reduced and some of the fluid is forced to move ahead of the obstacle.

Atmospheric bores on earth can result from katabatic drainage flows (e.g. Clark 1972), colliding fronts (e.g. Wakimoto and Kingsmill 1995), dissipating gust fronts (e.g. Koch *et al.* 1991), and hurricane outflows (Simpson 1997). On Mars, they are believed to be generated by the onset of katabatic winds forming a sharp gravity current front along the slopes of the volcanoes (Hunt et al. 1980; Hunt et al. 1981; Pickersgill 1984; Simpson 1997). Pickersgill (1984) estimated the speeds of these bores to be between 6.8-27.5 m/s. Observations of martian bore wave clouds flowing around large topographic barriers suggest the disturbances are confined near the surface (Hunt *et al.* 1981).

Kahn and Gierasch (1982) attempted to use simple mathematical models to explain the characteristics of the observed long wave clouds. They used four theoretical models: a slope wind model, a potential flow model, a hydraulic jump model, and an internal gravity wave model. Their study suggested alternative processes in the formation of the wave clouds. From the results of the slope flow model and hydraulic jump model, it was proposed that katabatic flows from the volcanoes were strong enough to cause the production of a hydraulic jump near the base of the slopes. The internal gravity wave model showed that it was possible for gravity waves to exist downstream of the jump. Kahn and Gierasch suggested that these gravity waves were what form the long wave clouds. However, despite the different processes presented, the clouds were still referred to as bore-wave clouds.

1.2.3 Thermal Circulations

Thermal circulations are an important mesoscale process on Mars. Ye *et al.* (1989) showed, using analytical methods and a 2D numerical model, that topographic slopes significantly affect atmospheric flows. Both analytical and numerical approaches confirm that steeper slopes lead to stronger upslope winds. The analysis also showed that sensible heat fluxes increased as wind increased, which forced the development of a slightly deeper martian boundary layer (MBL) than would have otherwise formed.

The sensitivity of sensible heat fluxes to wind speed controls the relative contribution of the sensible heat flux to the total heating of the MBL. When the winds are intense, sensible heat fluxes dominate over net longwave flux divergence and solar absorptivity – the two other contributors to MBL heating. When the winds are weak, the values for the sensible heat flux are comparable to the net longwave flux divergence. The heating of the MBL is mostly dominated by these two components. The solar absorptivity contributes only about 10% of the two other components combined.

In addition to slope effects, spatially varying thermal inertia and albedo have considerable impact on thermal circulations (Siili 1996). Using a 2D hydrostatic model, he showed that varying thermal inertia and albedo produce a sea-breeze like effect, with air rising over low albedo/high thermal inertia regions. Low albedos are associated with higher surface temperatures, relative to brighter regions, because more solar insolation is absorbed rather than reflected. This would cause the air to flow from high albedo regions to low albedo regions on Mars.

Thermal inertia has the opposite effect of albedo on surface temperature. Air flows from regions with low thermal inertia to those with high thermal inertia. Thermal inertia refers to how quickly temperatures on the surface adjust to changes in atmospheric thermal forcing and values depend on surface material. High thermal inertia means surface temperatures adjust more slowly. After the sun sets, low thermal inertia regions tend to cool more quickly than areas with higher thermal inertia. The resulting temperature gradient drives sea-breeze-like circulations. Siili found that the magnitude and phases of these surface induced circulations were highly sensitive to the signs and magnitudes of both thermal inertia and albedo variations.

The effect of these circulations on atmospheric dust loading has also been examined. In the regions studied by Siili (1996), albedo and thermal inertia-driven flows by themselves appeared to not be sufficient to significantly contribute to atmospheric dust load. Other numerical simulations, however, showed that high thermal contrasts associated with the polar cap edge drove high surface winds that can potentially lift dust (e.g., Toigo and Richardson 1999; Siili *et al.* 2000). Other factors that can affect the amount of dust loading include an increase in surface roughness (thereby increasing surface stresses), strong large-scale prevailing winds combining with mesoscale circulations, or combinations of other mesoscale flows such as slope winds.

Evidence of this potential dust lifting can be seen through observations that show dust from dark high thermal inertia regions tending to get displaced to relatively brighter and lower thermal inertia areas (e.g. Christensen 1988). The direction of the circulations

driven by thermal inertia and albedo gradients match this movement of mass and could be part of the reason for this displacement.

1.3 Current Approach

This research aims to simulate three specific regional atmospheric phenomena on Tharsis. The potentially large thermal forcing of extreme topography, the observed bore wave phenomena, and the uncertainties regarding the actual formation mechanisms of the different kinds of wind streaks require closer examination. All the processes thought to be involved in these small-scale phenomena are not resolved well by current MGCMs. In order to accurately capture the highly localized circulations, it is necessary to use a mesoscale model. The details of the model that was utilized in this study is given in the following chapter.

According to the study of Ye *et al.* (1989), steeply sloping topography has a significant effect on the strength of winds and the distribution of heating in the MBL. This study will examine how significantly topography can affect regional-scale air circulations, and determine how far-reaching these effects can be.

Among the effects of the slope flows are the generation of long wave clouds observed along volcano flanks, which are associated with nightly katabatic winds (Hunt *et al.* 1981; Kahn and Gierasch 1982; Pickersgill 1984). Hunt *et al.* (1981) characterize these clouds as an indication of a bore wave system. Kahn and Gierasch (1982) suggest that these long wave clouds were generated downstream of a hydraulic jump occurring at the base of the slopes, produced by the interaction of the downslope winds with down-

stream flow. This phenomenon has not been simulated using a full 3D mesoscale model, thus, it is not clear which processes are truly involved in the generation of these observed bore wave-like clouds. This study aims to determine how these wave clouds are generated.

With wind streaks, the simulations will attempt to determine the meteorological conditions required for both dark and bright streak formation. At present, there are two theories for dark streak formation and one for bright streaks. The first theory for dark streaks require an unstable atmosphere and strong winds (Veverka *et al.* 1981). The second theory also requires strong winds but states that a stable atmosphere would be more conducive for the occurrence of dark streaks (Fenton and Richardson 2001). Bright streaks are believed to form at high static stability and with steady, unilateral winds (Veverka *et al.* 1981).

Wind streaks also act like wind vanes, giving evidence to current, and possibly past, wind regimes. Many of these features are associated with topographical features; several wind streaks were observed to be oriented downslope of the Tharsis volcanoes (Lee *et al.* 1982). Matching the streak orientations to numerical simulation results should give an idea what dynamics dominate the flows prevailing on Tharsis.

2. Model Description and Simulation Design

2.1 Mars Regional Atmospheric Modeling System

The Mars Regional Atmospheric Modeling System (MRAMS) is the tool chosen to investigate the atmospheric phenomena on Tharsis discussed in Chapter 1. MRAMS was adapted for Mars from a widely used earth version, the Regional Atmsospheric Modeling System (RAMS). It is a non-hydrostatic model that simulates synoptic-scale, mesoscale and microscale atmospheric flows over complex topography. The use of this model is ideal since MRAMS runs at resolutions comparable to that of the data products obtained from the Mars Global Surveyor (e.g., MOC images). Rafkin *et al.* (2001) give a complete description of the model. MRAMS has been previously used for simulations over Mars Pathfinder (MPF) site and for large eddy simulations (Rafkin *et al.* 2001; Michaels 2002; Michaels and Rafkin 2002).

MRAMS dynamics is governed by the grid-volume Reynolds-averaged primitive equations. Turbulent mixing in the model is parameterized using mixing coefficients determined by schemes specified by the user. The four schemes included in the model are high order closures described by Deardorf (1972), Mellor and Yamada (1982), and two lower order closures described by Smagorinsky (1963).

For radiative transfer, MRAMS utilizes an algorithm directly derived from the NASA-Ames MGCM (Haberle *et al.* 1993, Haberle *et al.* 1999). Radiative effects of CO_2 gas and suspended dust at both infrared and thermal wavelengths are included (Rafkin *et al.* 2001). As of this writing, cloud microphysics are not yet active in the model, thus radiative effects due to water ice clouds has been neglected. Dust and CO_2

emissivity coefficients have been calculated offline and put into large, high resolution lookup tables to be utilized by the radiation parameterization package every radiation timestep. This timestep is specified by the user.

Effects on radiative transfer by topographic shadowing and slope angles have been taken into consideration in MRAMS. Due to the ease with which the Martian surface absorbs and emits heat, a shadowed region may create a significant temperature gradient with its sunlit surroundings, driving circulations that would otherwise not have developed (Michaels 2002). A similar effect is induced by the slope of the terrain. Tops of volcanoes receive solar heating earlier in the day than does the ground below, creating a temperature gradient that may force thermal circulations. The user can choose to activate either, or both, of these features. Topography data is derived from Mars Orbiter Laser Altimeter (MOLA) results; its resolution is 1/32 of a degree in latitude and longitude. This instrument is on board MGS.

MRAMS also employs a surface layer model and a multi-layer soil model. The surface layer model governs the transfer of heat and momentum between the surface and the atmosphere. The fluxes are derived using the Monin-Obukhov similarity theory. Below the surface layer, the soil model assumes energy transfer occurs through conduction. Changes in soil temperature are functions of both albedo and thermal inertia, together with fluxes provided by the radiation and surface layer parameterizations. For albedo and thermal inertia values, MRAMS uses data derived from the Thermal Emission Spectrometer (TES) on board MGS. This dataset is spatially varying, and has a resolution of 1/8 of a degree in latitude and longitude. Both datasets, however, degrade from the mid-

latitudes poleward and should, therefore, be used carefully at high latitudes (Michaels 2002).

Initial and boundary conditions are provided by the NASA Ames MGCM (Haberle *et al.* 1993). History files from the GCM are fed into a pre-processor to be mapped onto the MRAMS domain. The GCM data are on sigma-pressure levels and the pre-processor module interpolates these data onto the MRAMS sigma-z vertical grid. Both initial and boundary conditions are vary spatially. Boundary conditions can be supplied to the model as frequently as every 1.5 hours.

The model's horizontal grid is not regularly spaced in latitude and longitude. Instead, a polar-stereographic grid is utilized, with constant distances between grid points on the map projected grid (Rafkin *et al.* 2001). The resulting grid spacing in physical space is irregular, thus map scaling factors are used in taking horizontal derivatives. In the vertical, MRAMS uses a terrain-following sigma-z coordinate. The vertical spacing is not regular, but geometrically stretched with the finest grid spacing nearest the surface. The user specifies the height of the lowest vertical level, as well as a constant geometrical stretching factor. For example, a stretching factor of 1.0 provides uniform vertical grid spacing. A maximum vertical grid distance is also given by the user to prevent undesirably large grid spacing at higher levels. For those who prefer higher resolution at heights other than the surface can specify the model levels explicitly.

MRAMS makes use of two-way interactive nested grids. The parent grid values are used as boundary conditions for the finer grid, and after the physics for the finer grid has been solved, results are averaged back to the parent grid. In the original nesting algo-

rithm, the meteorological parameters from the fine grid were averaged back into the coarse grid using the density of the coarse grid, instead of the fine grid. This created a discrepancy between the values computed by the coarse grid and the resulting values averaged from the fine grid. Heat and mass were not conserved between grids. The difference between the two became significant enough to cause the model to become unstable. In order to correct this, modifications were made such that the density used in the averaging was that of the fine grid. The resulting average values were more representative of what the fine grid was able to resolve, and there was both heat and mass conservation.

2.2 Computational Grid Configuration

All simulations in this research are configured with four grids. The first grid has a horizontal grid spacing of 240 km. This grid is configured to provide a smooth transition from the MGCM spacing to mesoscale model spacing, and encompasses the entire Tharsis bulge. The second grid covers Olympus Mons and the Tharsis Montes, and has a 60 km grid resolution. The third and fourth grids differ in location depending on the region of interest; specific locations will be discussed in the following chapters. The third grid, however, always has a 15 km grid spacing, while the fourth has 3 km resolution. All grids have the same vertical resolution, with vertical grid intervals increasing with height. The lowest model level is at 25 m above the ground, with the maximum interval reaching 1200 m. The model top reaches approximately 60 km above the ground using 67 vertical points. All the runs have a dynamical timestep of 14 seconds for the first grid and 4.7 for the rest of the grids.

Examination of seasonal variations in the circulations was also an important part of this study. Thus, simulations were run for four different seasons: L_s 90°, 142°, 180°, and 360°. L_s 142° was the original test case, used with the LES runs and Mars Pathfinder simulations (see Rafkin *et al.* 2001; Michaels 2002; Michaels and Rafkin 2002), and the research expanded to include three cardinal seasons. The fourth, L_s 260°, was not included as there were some slope effects during that season that the current model grid configuration could not handle. Only by restoring the original nesting algorithm – where the density between grids was not consistent – did the simulation run for that season. A possible reason for this is that there was too large a difference in the predicted densities between grid 2 (at 60 km resolution) and grid 3 (with 15 km resolution) when using the modified nesting routine. The original nesting algorithm used the coarse grid densities and thus may have made the transition between grids smoother. Since this method would be not conserve mass and heat, however, the original nesting routine could not be a solution to the problem. A possible solution would be to nest down less rapidly, reducing the differences between grids.

Dust is also an important part of the study. A spiral dust cloud observed over Arsia (presented in the thermal circulation section below) hinted at intriguing circulations above volcanoes, and the dust distribution is especially significant in examining wind streak formation. Thus, dust was added as a tracer to determine from which areas dust could be lifted, where it would concentrate, and where it might settle. Dust was lifted at an arbitrary constant rate of 100 mass units of dust per kilogram of air per second whenever the surface stress reached a threshold of 14 mN for the wind streak and bore studies.

The arbitrary values are easily scaled to produce real dust mixing ratios provided a source rate is known. Stress was computed using the friction velocity and density predicted by the model.

The threshold and the constant lifting rate values were chosen since one purpose of the study was to find out where the dust would be transported, should it be lifted, and to get an idea of the circulation that may have lifted it. Later in the diagnosis of the model results, tracer values were normalized to provide dust mixing ratios according to the dust lifting equation formulated by J. R. Murphy (personal communication):

$$\frac{\partial r}{\partial t} = 2.431\times10^{-5} * \tau^2 * \left(\frac{\tau - \tau_t}{\tau_t}\right) \qquad (3)$$

where r is the dust mass flux in kg m^{-2}, τ is surface stress, and τ_t is the stress threshold. The simulations for the Arsia spiral study (presented below in the chapter about thermal circulations) used this equation directly for dust lifting rate rather than the constant arbitrary value. The threshold used in (3) is also 14 mN. Since sedimentation of dust was not included in the simulations, the actual amount of dust in the atmosphere may not be accurate. However, the simulations give a first guess as to the dust distribution. Once dust is lifted, it is advected by the wind with no fall velocity. For the Arsia spiral experiments only, the lifted dust was added to the model's total dust opacity, making it radiatively active.

3. Results and Discussion

The low-level flow in the Tharsis region is controlled by the topography. The volcanoes act as massive, elevated heat sources during the day, and the trend of daytime flows is towards an upslope circulation. At night, downslope flows dominate. The winds flow radially outward from the Tharsis bulge.

At slightly higher elevations, westerlies prevail and above that, easterlies. The depth of the westerlies varies according to season. Westerlies are deepest during the winter when the region is under the descending branch of the Hadley cell, while easterlies dominate during the summer (Haberle *et al.* 1993).

3.1 Thermal Circulations and the Arsia Spiral

Focusing on the mesoscale, circulations in the Tharsis region are more complex than mere downslope and upslope flows. Evidence of this was seen in the MOC image of a spiral dust cloud over the caldera of Arsia Mons, the southernmost volcano of the Tharsis Montes (Fig. 11). The spiral was imaged at southern spring equinox (L_s 180°), on June 19, 2001, at 2 PM local time. This structure was observed for several days, although it is unclear whether this was the same spiral or a phenomenon that recurs daily. The exact time of day that the spiral became optically visible is also uncertain since MOC only images once per martian day, or sol.

In an attempt to simulate this phenomenon, MRAMS was run with nested grids three and four situated over Arsia. Grid 3 encompassed the whole volcano, while grid 4 zoomed in on the caldera (see Fig. 12). The simulations were initially run at L_s 142°

(since initial and boundary conditions for this seasonal longitude were already in the database) but the results showed no spiral (Fig. 13b). The winds during this season attempt to spiral but do not seem able to organize into a more structured form. When run at L_s 180° – the same season as the observed spiral – a spiral was seen to form in the northern section of the caldera (Fig. 13a). The spiraling structure in the dust tracer field starts to appear around 3 PM local time, and is present for a few hours. The development of this feature at Ls 180° and the notable lack of helical structure at Ls 142 implied a seasonality to the phenomenon. MOC images showing no spiral over Arsia during L_s 142° support this finding (MSSS 2001). At present, it is unclear why the spiral appears only at this particular season. Changes in the circulation due to seasonal differences in solar heating can be speculated as a possible cause for this seasonality.

The vertical distribution of dust tracer above the caldera is shown in Fig. 14, which is a vertical cross-section through the center of the spiral at approximately 3 PM. It is at this time when a dust maximum in the vertical starts getting defined. The time in the MOC image (Fig. 11) was about an hour before. The relative tracer maximum on either side of the center comprises the spiral. The dust tracer mass reaches to over 20 km above the caldera surface, with relative maximum values found at around 18 km above ground level. Although the time in the image is not the exact time as in Fig. 14, this value can still be roughly compared to the observational data derived from the MOC image. The length of the shadow seen to the right of the cloud (in Fig. 11) gives an indication of the cloud's height. This height was computed from the incidence angle and shadow length taken from the image data (see Fig. 15). It is not clear how much higher

the center of the spiral is relative to the rest of the cloud, making the calculation of the cloud height more complicated. It can be estimated, however, by measuring the shadow length from the edge of the brightest part of the spiral to the edge of the darkest part of the shadow. Since the portion of the cloud that is optically thickest will cast the darkest shadow, the resulting height can be compared to simulation results. We computed the length as being 15-18 km, resulting in a height of about 18-21 km above the caldera. This height compares favorably with where the model predicted the densest tracer concentration.

The spiral is an indication of the presence of a larger thermal circulation forced by the daytime heating of the volcano. Figure 16 shows the full extent of the dust distribution, which results from the daytime thermal circulation over Arsia. Winds spiral up the volcano, and upon reaching the volcano summit, converge and flow upward along a helical trajectory. The observed dust cloud highlights this structure. Dust is picked up along the foot and slopes of the volcano, is carried upslope and converges with the flow to form the visible spiral. Aloft, the flow diverges, with return flow winds exceeding 60 m/s. By the end of the afternoon, this circulation has transported dust up to a thousand kilometers away, in a suspended layer about 20 km above the surface. In comparison, the winds closest to the surface only reach about 40 m/s. The large difference in wind speeds is due to the lower density of the atmosphere at higher altitudes. Conservation of mass dictates the flow velocities in the region of lower densities should greatly exceed flow velocities at higher densities.

This structure of convergence below and divergence aloft is reminiscent of warm core lows observed on Earth. In the case of Mars, the flow is driven by the relative low pressure generated by the warm volcano. As the sun warms the volcano slopes, the near surface air becomes warmer than its surroundings, creating a pressure gradient.

As air rises past the summit and up to several kilometers above the volcano, it is adiabatically cooled, forming a cold spot at the peak of the circulation (Fig. 17). This generates high pressure aloft, enhancing the divergence in the return flow. The cold spot sometimes reaches temperatures as low as 115 K at heights that reach almost twice the height of the volcano. Over Olympus Mons, the circulation reaches to nearly 40 km above the geoid. Low temperatures at such great heights are conducive for both CO_2 and water cloud formation. Unfortunately, as of the time of this study, condensation and precipitation were not permitted in MRAMS. Thus, the model was run without the capability to form CO_2 or water ice clouds. MOC and Viking orbiter images, however, have shown that such clouds have been commonly seen to exist over the Tharsis volcanoes during the mid-afternoon [Image MOC2-134 (MSSS 2001)].

This circulation is important for other processes in addition to cloud formation. The large, daily venting of air could be a major source of dust in the atmosphere. Providing there is dust to lift, the circulation can lift it to heights double that of the volcano, and horizontally transport it up to thousands of kilometers away. This has implications on how the global dust load is maintained. The Martian atmosphere has been observed to maintain a typical background dust opacity value of about 0.3 (in the absence of dust storms). Currently, the dust cycle on Mars is attributed to Hadley-type circulations, dust

devils, local dust storms, baroclinic and planetary waves. This daily slope circulation may be another "constant" source of dust injection. The transport and distribution of dust by the circulation is much more rapid than the Hadley cell. Instead of vertically decreasing and diffused concentrations of dust expected from the Hadley cell, the transport of dust by the topography-induced circulation will form elevated layers of enhanced dust maxima, potentially creating, through radiative processes, mid level inversions. Should this be true, this circulation could affect the larger-scale momentum and thermal fields. A general description and summary of these simulation results were published by Rakfin *et al.* (2002).

At night, the surface flow reverses, and katabatic winds take over. As the sun goes down, the volcanoes cool faster than the surrounding air, generating a relative high pressure, and forcing downslope katabatic winds. In the model, atmospheric bores have been seen to form along the leading edge of the katabatic flows (i.e., along katabatic fronts). The nighttime flows and atmospheric bores are discussed in more detail in the following section.

3.2 Bore Wave System

A most interesting event is predicted every Martian night in the simulations. An atmospheric bore-like system was found to develop and propagate radially away from the volcanoes. This finding matches observations of low lying wave clouds along the flanks of Tharsis volcanoes seen during the early morning hours (Fig. 8). From Viking orbiter images (e.g., Hunt *et al.* 1981; Kahn and Gierasch 1982; Pickersgill 1984), it was seen

that the wave clouds were most evident during late spring to early summer and only during the early part of the morning. They found that the clouds dissipated by around 10 in the morning. The wavelengths they derived from these Viking images ranged from 10-20 km, and the propagation speeds were taken to be 6.8-27.6 m/s.

The observed system was theorized to have been caused by nighttime katabatic winds. The air near the surface of the volcano radiatively cools faster than the surrounding atmosphere, making the near-surface air more dense. This creates a density gradient, forcing the colder, heavier air to rush down into the warmer, less dense air below. The resulting density current generates a bore that propagates along the low-level nocturnal inversion.

In order to resolve the horizontal and vertical structure of the bore wave system, nests three and four of these simulations were positioned slightly northeast of Olympus Mons (see Fig. 18). The simulations were run for four seasonal longitudes: L_s 90°, 142°, 180°, and 360°, to determine the seasonal variations, if any, of the phenomenon.

Results show that katabatic fronts are formed by strong downslope flows that come from all four of the Tharsis volcanoes in the domain every night at each of the seasonal longitudes (Fig. 19). The bores form at the leading edge of these fronts. The fronts from Pavonis, the southwestern side of Ascreus, and the northeastern side of Arsia quickly lose their coherence as they meet and converge. Few katabatic fronts travel extremely long distances before they dissipate. Encountering mostly plains to the west, the disturbance associated with the density current from Arsia is an exception. It travels almost 1000 km before the perturbation dissipates.

Figures 20(a)-(d) show the vertical profiles of potential temperature (θ) and density (ρ) of the bore for each of the four simulated seasons. This figure can be compared to the streamlines of a bore observed on earth (see Fig. 21). Since potential temperature surfaces are material surfaces for adiabatic processes, the theta contours are comparable to the streamlines in Fig. 21. In this case, because there are strong, diabatic processes involved as well, the θ contours are more of an approximation. Despite this being the case, the structure predicted by the model is similar to the undular bore structure observed over the head of the density current.

Most noticeable are the undulations seen at L_s 180° (Fig. 20(d)), and the lack thereof at L_s 90° (Fig. 20(b)). Results at the other seasons seem to be intermediate between these two. The number of undulations observed imply the strength of the wave (as explained in the previous section). More undulations imply a weaker bore, with a lower ratio between the bore height, h_1, and the original height of the inversion, h_0. Bores with values of $h_1/h_0 < 3$ usually develop undulations behind the gravity current head, while a ratio larger than 3 characterizes turbulent bores that have no undulations. When a bore is turbulent, the gravity current generating the bore is moving at a velocity greater than that at which a gravity wave can propagate. This relationship between the speed at which a disturbance is moving and the maximum speed a gravity wave can propagate along an interface is given by the Froude number.

The Froude number, Fr, is given by the formulation,

$$Fr = \frac{U}{\sqrt{g' h_0}} \tag{4}$$

where U is the speed of the disturbance (m s^{-1}) relative to the background wind, and the denominator is the phase speed of a shallow gravity wave traveling along an interface between two fluids of differing densities. This maximum speed is dependent on the height of the fluid interface, h_0 (m), through which the density current is moving, and a measure of the gravitational contribution due to the density gradient, g', which is given by

$$g' = g\left(\frac{\rho_2 - \rho_1}{\rho_1}\right) \tag{5}$$

where g is the gravitational acceleration in m s^{-2} (the simulations used 3.72 m s^{-2} for Mars), and ρ_2 and ρ_1 (in kg m^{-3}) are the densities of the upper and lower fluids, respectively. This quantity, g', is sometimes referred to as reduced gravity. If $Fr \leq 1$, gravity waves forced by the disturbance (in this case, the bore) can propagate along the given interface. If $Fr > 1$, the flow is said to be supercritical. In this case, the disturbance is moving faster than gravity waves can propagate. A shockwave front is produced since gravity waves are unable to carry away energy from the source.

In the model, the atmosphere is seen as a continuously stratified fluid, and it is difficult to get an exact value for the Froude number (which was formulated for a two layer fluid). To get an approximate value of h_0, the interface between two fluids was assumed to be the height of the inversion ahead of the bore. As the gravity current propagates, the inversion height increases to the height of the gravity current. The higher density was taken to be the average density within the density current, and the lower density value was taken as the average density of the atmosphere at the surface before the pas-

sage of the bore. The resulting density difference was on the order of 10^{-3} kg m^{-3}. The predicted speeds of the bore waves for all the simulated seasons ranged from 25-35 m s^{-1}, and the approximate Froude number for all simulated seasons exceeded 1. This explains why no waves are seen to propagate ahead of the gravity current. Instead, these waves seem to be generated at the current head, and are then left behind to dissipate. The lowest Froude number was found at L_s 180, which coincides with the finding that the bore has the most undulations during this season. The strongest bore (with the least undulations) and the highest Froude number were at L_s 90.

At the density current head, air is forced up rather steeply, as evidenced by the potential temperature surfaces. As the less dense air is forced to rise above the cold current, it sometimes breaks through the inversion (Fig. 22). The rising air generates a large rotor-like disturbance, along the boundary between between the easterlies aloft and westerlies below. Figure 23 shows this disturbance for all simulated seasons. This disturbance is large enough to perturb the layer of easterlies and produce a mountain wave-like effect behind the rotor-like circulation. In this case, the "mountain" is the disturbance and since it is moving, the situation is can be analyzed with the frame of reference moving with the flow. These waves were evident during L_s 90°, 142°, and 180° (Fig. 23(b)-(d), respectively). They appear to be internal waves that do not propagate in the vertical, and instead damp with height. To confirm this, it needs to be shown that the phase lines do not tilt, i.e., the vertical wavelength is infinite.

Starting with the assumption that the vertical wavelength is indeed infinite, the vertical wavenumber, m, is practically zero. The scorer parameter, defined as $l^2 = m^2 +$

k^2, should then approximate k^2, the square of the horizontal wavenumber. For the initial assumption to be true, it must be shown that l^2 diagnosed from the model results is approximately equal to the wavenumber derived from the observed wavelengths in Fig. 23(b)-(d).

The formulation used for the calculation of the Scorer parameter is

$$l^2 = \frac{N^2}{U^2} - \frac{1}{U}\frac{\partial^2 U}{\partial z^2} \tag{6}$$

The first term is the ratio of the Brunt Vaisala frequency (N^2) in units of s^{-1}, and the wind speed (U) in units of m/s. The second term represents the curvature of the wind and when U is large, this term becomes negligible. The Scorer parameter also becomes very small when U is large. In this case, the U that is used is the background wind (magnitude of the easterlies) plus the speed of the gravity current (because the disturbance is moving upstream). The resulting l^2 in the region of the wave is on the order of 10^{-7} m^{-2} (at L_s 90°). The wavelengths of the waves upstream of the disturbance (and downstream of the easterlies) were found to range from about 15-45 km, giving a maximum k^2 on the order of 10^{-7} m^{-2}. This number is the same order of magnitude as the calculated l^2, which confirms that the wave does not have significant propagation in the vertical. In comparison, a typical value for the Scorer parameter used in some theoretical and numerical studies for Mars was on the order of 10^{-2} m^{-2} (Pickersgill and Hunt 1980).

The energy that cannot be carried away by gravity waves leaks out through the rotor-like disturbance and produces these waves. The easterlies aloft trap this energy, preventing it from propagating. The waves become more pronounced when the easterlies are strong and deep, as seen in Fig. 23. The easterlies are deepest at L_s 90° and 142°

(Fig. 23(b) and (c)), and the waves are also most defined during these times. At L_s 360° (Fig. 23(a)), hardly any waves are seen and the atmosphere above the bore is mostly turbulent. This may be because the energy is more effectively absorbed in the critical layers that form between the easterlies and a second set of westerlies above. At this season, the easterlies aloft are shallow and the boundary between them and the next layer of westerlies above is at a much lower height. The developing wave is torn apart by the shear of the reversing winds. Easterlies are also relatively shallow at L_s 180° (Fig. 23(d)), and wave activity is also diminished during this season.

The internal waves predicted at L_s 90° and 142° are most likely the cause of the wave clouds observed by Viking (see Fig. 8). They have a propagation speed equal to that of the density current (~25-35 m/s) and are seen to form below the summit of the volcano (in this case, Olympus Mons), approximately 15 km above ground. Though these results are from Olympus Mons, they are comparable with observational data from the wave clouds seen near, and between, Pavonis and Arsia Mons. The observed typical propagation speed for the bore waves near these volcanoes was 6.8-27.6 m s^{-1} (Pickersgill 1984). Moreover, although resolution is poor in the 60 km grid, results from grid two do show an indication of wave activity in the saddle between Arsia and Pavonis Mons. The bore cloud was observed between the two volcanoes at approximately 6:30 AM local time. At this same time at L_s 90°, the model results show a line of convergence between the two volcanoes where katabatic flow from Arsia and Pavonis meet (not shown). The w-field shows a wave like pattern about 20 km above the region north of Arsia and southwest of Pavonis (Fig. 24).

Since the bore phenomenon is strongly associated with topography, the same disturbance, albeit slightly weaker perhaps, can be expected over the other volcanoes in the region as well. Thus, according to the simulations, bore waves do indeed form due to katabatic winds on Mars. Additionally, wave activity aloft generated by the bore's passage produces the observed clouds along the flanks of the volcanoes. This is in contrast with a previous theory that the wave clouds were generated by gravity waves propagating downstream of a hydraulic jump occurring at the base of the volcano slopes (Kahn and Gierasch 1982).

3.3 Wind Streaks

Aside from topography-forced low-pressure systems and bore-wave like phenomena, Tharsis is also a place where wind streaks are found in abundance. The most common streaks on Tharsis are those that have been classified as Type I(b) and Type I(d). There are also a few mixed streaks (Type I(m)) scattered over the region. As discussed in the first chapter, Type I(b) streaks are believed to be depositional and the proposed conditions for formation include high stability, high dust opacity, and relatively weak, unidirectional winds. For Type I(d) streaks, two hypotheses have been put forward regarding their formation. Both hypotheses require strong winds, but theory one needs low stability (Veverka *et al.* 1981), while theory two needs high stability (Fenton and Richardson 2001).

Simulations were carried out to test these hypotheses and determine under which conditions predicted wind directions match observed streak orientations. The simulation

design was similar to that of the bore wave study, with four seasonal runs (L_s 90°, 142°, 180°, and 360°) and with grids 3 and 4 centered on a large crater a few degrees slightly northeast of Olympus Mons (at approximately 122°W and 24°N). This region was chosen because of the presence of observed bright streaks associated with small craters surrounding a large one, which has no obvious streak (see Fig. 25). The objective was to determine what influence the flows from Olympus Mons and from the large crater would have on streak formation. Results from grids 2 and 4 will be used mostly in the analysis.

Grid 2 shows the diurnal circulation over the whole region. The predicted mesoscale wind directions are compared with catalogued wind streaks based on observational data. Figures 26(a)-(d) show streak orientations from observational data, with each map documenting data gathered over a period of 90° of L_s (taken from Lee *et al.* 1982).

If current theory for bright streak formation were correct, nighttime would be most conducive for forming Type I(b) streaks, since high stabilities are associated with the development of the nocturnal inversion by radiative cooling. Predicted wind speeds and directions averaged over the nighttime and daytime are presented in Fig. 27 and Fig. 28, respectively. There is little difference in wind directions between the seasons. The regions noted A and B in the observational data maps (Fig. 26), seem to have the best correlation with the simulation results. Winds at A are caused by the nightly katabatic flow from Arsia. The downslope winds on the western side of Arsia are strongest and reach the farthest. The katabatic winds on the northern and eastern side collide with similar flows from Pavonis, limiting their extent. The flow in region B is a combination of redirected converging downslope winds from Pavonis, Ascreus and Alba Patera (partly

seen in the north edge of the domain). In both regions, the winds continue in the same general direction until the sun comes up and downslope flows switch to upslope. All seasons indicate the same patterns during the night, and only differ slightly in wind magnitudes.

To determine whether the winds during this time are indeed conducive for deposition rather than erosion, surface stresses should be less than thresholds for dust lifting. Previous work (e.g., Greeley *et al.* 1980) gave thresholds in friction velocities at certain pressures and temperatures. Using Bagnold's equation for surface stress,

$$\tau = \rho u_*^2 \tag{7}$$

where τ is surface stress (kg m^{-1} s^{-2}), ρ is air density (kg m^{-3}), and u_* is friction velocity (m s^{-1}), and data from Greeley's (1980) wind tunnel analysis, it was determined that the average minimum stress required for lifting a 100 μm dust particle was approximately 30-35 mN. From the wind tunnel tests, 100 μm dust particles are the easiest to saltate. The surface stresses generated by the nighttime winds in both regions A and B reach about 25 mN in all seasons. Although close to the threshold, it is still reasonable to expect deposition rather than erosion to occur. If current theory for bright streaks were accurate in assuming that positive stability aids in developing pockets of relatively weak winds behind obstacles, with the unidirectional winds found in regions A and B, meteorological conditions would be conducive for depositional streak formation. Naturally, there would have to be enough dust in the atmosphere to settle out in these pockets before deposition could take place.

Not all the streaks observed in regions A and B are depositional. There are also erosional streaks. The closeness of the predicted wind stresses to the theoretical values indicates that it is possible for erosion to occur in these regions as well. It is not clear from current hypotheses whether positive or negative stability is required for erosional streaks to form. Streak orientations in regions A and B seem to better match nighttime wind directions, implying nighttime positive stability to be a condition for streak formation. The bright streaks observed over the volcanoes are also mostly oriented downslope, further strengthening the supposition that conditions for bright streak formation are met during the nighttime.

There also are streaks whose orientation do not match predicted wind directions. Some differences might be because of topographic influences not resolved by the 60 km grid resolution. Others, such as downslope oriented dark streaks forming a collar around the summits of some volcanoes (see Fig.6), are harder to explain. These kinds of streaks were hypothesized to have been eroded away by katabatic winds. Given that the pressure at the top of the volcanoes rarely get as high as high as 3 mb, it would take unusually high friction velocities to move any dust particles. Unfortunately, the simulations do not predict high enough values for u_*, and surface stresses hardly reach 20 mN. Moreover, the results from the Arsia spiral studies show that stresses are a maximum during the day, when the flow is upslope. Though this helps with the formation of the dust cloud over Arsia that was discussed previously, it does not agree with apparent streak orientations observed on the caldera. It is also possible that these dark streaks could have formed at an age when the pressure of the Martian atmosphere was significantly higher than the

present. This would imply that these streaks are ancient, or possibly due to rare, "catastrophic" events.

There is another discrepancy between the current formation theories and model predictions. Grid 4, which is in region B, showed some intriguing results as the katabatic front passed through its domain (Fig. 29(a)). High wind speeds and surface stresses accompanied this front (Fig. 29(b)). Stresses sometimes exceeded 50 mN while wind speeds reached more than 30 m/s. With stresses of this magnitude, the front should generate enough force to initiate saltation of particles with sizes ranging from 60 μm to 200 μm. Interestingly enough, no dark streaks are observed in this region (see Fig. 25) and the bright streaks that are observed, are oriented perpendicular to the direction of front propagation. After the front passes through, a prevailing southeasterly flow takes over. These are the winds seen in Fig. 27, where similar katabatic flows from both Pavonis and Ascreus Mons merge and stream through the shallow valley east of Olympus Mons, where the domain of grid 4 is located. This flow matches the bright streak orientations. As mentioned earlier, the wind stresses corresponding to this flow are relatively low. With high stability high during the night, the proposed conditions for bright streak formation would be met, assuming a dusty atmosphere. According to the second theory for dark streak formation, however, the conditions as the front passes through should be favorable for dark streaks as well. Thus, if this theory were correct, dark streaks should be observed in this same region. Even 30 years ago, when the Viking orbiter imaged the same region (see Fig. 30), there was no indication of dark streaks parallel to the direction of front propagation. Instead, bright streaks with the same orientation as that in the MOC

image are found. Although the region seems to have more dust in the MOC image, as evidenced by the slight differences in bright streak margins, the wind direction indicated by the streak orientations remains unchanged. An examination of tracer behavior due to frontal passage could provide a possible explanation to this discrepancy between front propagation direction and streak orientations.

Figures 31(a)-(c) show dust tracer concentrations before, during, and after the front comes through. It can be seen that as the front comes through, it provides a source for the tracer. After the front has passed through, the region has significantly more atmospheric dust than it had originally, and as the flow turns parallel to the streaks a few hours later, this dust may then settle out in the sheltered region downwind of the obstacles. A similar process is seen on Arsia. Its katabatic flows extend far to the west, as there is not much topography to interfere with the flow. The east-southeasterly wind direction initiated by the downslope winds becomes the prevailing flow that matches streak orientations in region A.

To summarize, simulations results seem to match the conditions that the current hypothesis states are conducive for Type I(b) streak formation. Bright streaks are observed in regions where the model predicts unilateral flow parallel to streak orientations, together with high static stability. This unilateral flow is seen on a nightly basis after a katabatic front passes through. For region A, the front is from Arsia and for region B, from Olympus Mons. These results seem to reinforce the existing theory of Type I(b) formation. It is speculated that the front generates enough surface stress to lift dust. Af-

ter the passage of the front, when the winds become unidirectional, the dust could potentially settle behind the craters, forming the bright streaks.

Dark streaks are also found in region A. These may be caused by high stresses associated with frontal winds from Arsia. If dark streaks form as a result of frontal passage, however, it should follow that dark streaks should also be found in region B. This is not the case. One proposed hypothesis for this is that the stresses associated with the fronts from Olympus Mons are strong enough to lift dust indiscriminately and not just behind craters and obstacles. In Arsia's case, the dark streaks are observed quite a few degrees west of the volcano. The fronts may have dissipated slightly by this time, decreasing friction velocities. Then, only when coupled with increased wind shear due to rough topography (i.e., a crater) can the stresses be high enough to initiate lifting, thus forming dark streaks. This process and the stress magnitudes cannot be confirmed unless MRAMS is run with a nest is placed in that region. The simulations seem to suggest that formation of both Type I(b) and I(d) occur when the atmosphere is statically stable. This also suggests that turbulence borne of strong wind shear may be a bigger factor in erosional streak formation than buoyancy generated turbulence.

The model has not been able so far to match streaks observed on the summits of the volcanoes. Observations show dark streaks at high altitudes, and simulations do not predict friction velocities strong enough to move particles at such low pressures.

4. Conclusion and Recommendations

The extreme topography of Tharsis dominates the local air circulation of the region. Circulations are governed by the diurnal heating of the volcanoes. During the day, the heated volcanic slopes drive upslope winds that develop a rotational component and generate a warm core-like vortex above each volcano. There is convergence close to the caldera surface and divergence aloft, at heights sometimes reaching 40 km. The spiral observed by MOC (Fig. 11) highlights the spiraling upflow above the caldera.

The outflow from this phenomenon extends for thousands of kilometers. This has implications for atmospheric dust loading and transport. Should dust be lifted from near the base of the volcanoes and be carried up by the circulation, it is possible for it to be transported thousands of kilometers away in a suspended dust layer (see Fig. 16). This could play a significant role in the dust maintenance in the atmosphere. There is also potential for water and CO_2 cloud formation, as a cold spot forms from the adiabatically cooled air at the peak of the upslope flow. This finding compares well with MOC images of typical mid-afternoon cap clouds over the volcanoes. The vertical and horizontal extent of this circulation could have a significant effect on larger-scale thermal and momentum fields, such as heated dust layers creating mid-level inversions extending far beyond the Tharsis region.

During the night, density currents from katabatic flows generate bore waves. Horizontally propagating waves are also produced by a large rotor-like disturbance formed at the head of the gravity current. These waves are analogous to mountain waves on Earth. They damp and do not propagate with height, but they travel with the speed of

the density current since that is what generates them. These waves appear to be what form the undulatory clouds observed by Viking orbiter near the foot of volcanoes (see Fig. 8). The wave clouds do not appear to be created by gravity waves produced by a hydraulic jump at the base of the slopes.

The examination of possible correlations between daytime and nighttime flow regimes, together with atmospheric stability, on wind streak formation was inconclusive. Although, conditions thought to be required for light streak formation largely seemed to be met and matched with existing light streaks for certain regions of Tharsis, the formation processes for both light and dark streaks are not always straightforward. For example, the presence of high stability and high wind shear in a region does not imply the existence of dark streaks. This was shown by the occurrence of strong, nightly katabatic fronts in a region where only bright streaks were observed (see Fig.25). Because of the high surface stress values that are associated with the fronts, they may be an effective mechanism for lifting dust up into the atmosphere and can therefore lead to erosional streaks. As discussed earlier, the passage of the front can also result in depositional streaks. It appears the formation mechanism for bright streaks dominated since there were no dark streaks observed in Fig. 25. These fronts are one example of several processes that have, so far, not been taken into account in explaining the formation of streaks. The fronts and other similar atmospheric events could have significant implications on the conditions required for streak formation and on small-scale atmospheric dust loading.

In summary, this work has shown that there are more complicated processes involved in streak formation than those related directly to atmospheric stability and wind

speeds and directions. Many processes come to play in the formation of streaks; streak existence cannot be based solely on these few factors. The current formation hypotheses capture a portion of the full range of atmospheric dynamics that come into play. A cursory comparison between the predicted wind directions and observed streak orientations do, however, seem to agree that both dark and bright streaks were formed during times of high static stability.

Aside from wind streak results, the research on the Arsia spiral simulations has uncovered a possible major daily source of atmospheric dust loading that has not been studied previously. The cold spots seen developing over the tops of volcanoes are another result of the daytime upslope flows, and could provide a possible explanation for the cap clouds observed over the volcanoes (e.g., Image MOC2-134 (MSSS 2001)). Moreover, the results from the bore wave simulations have given further insight on the dynamics of the observed bores and have offered a possible explanation for the seasonality of the phenomenon. This ability of MRAMS to accurately simulate observations of the Arsia spiral and the bore waves has shown that this model will be an extremely useful and valuable tool in examining more of the local and regional-scale atmospheric phenomena observed to take place on Mars.

Further study is needed on the subject of wind streaks. As seen in the simulation results, streak formation is complex and the most localized forcings have to be taken into consideration. More experiments with grid nests over different parts of Tharsis are needed, especially over regions that experience more seasonal variations. These experiments should also be conducted in high altitude regions where apparent erosional streaks

are observed. This will aid in the determination of whether surface stresses at that altitude can reach the threshold for lifting.

The local region examined in this study was a small domain just northeast of Olympus Mons. As explained above, topography-forced fronts may play a role in the formation of winds streaks. Similar topography-controlled flows may occur in other regions on Tharsis. Further experiments are needed to examine other regions to determine whether the resulting smaller scale flows and stresses in those areas match streak orientations (and thus, current theories of streak formation).

A topography dataset that can resolve at least 1 km-wide craters (and other obstacles) would also be desirable. Most craters that have streaks associated with them are of this width. With this kind of resolution, it will be possible to predict either the development of the pocket of relatively weak winds in the lee of obstacles, or the acceleration of winds downwind of obstacles. This will help isolate the meteorological conditions required for both depositional and erosional streak formation. Adding a good dust sedimentation algorithm would also be useful, as it can provide a first estimate of where dust would preferentially settle out, once lifted.

For the daytime thermal circulation, simulations using more realistic dust lifting thresholds would be desirable in order to ascertain a realistic amount of dust that could be transported by the daily venting over the volcanoes. As mentioned above, a deposition scheme would also make the dust concentrations more accurate. A cloud microphysics model would be a good addition as well. This will allow the simulation of cap clouds over the Tharsis volcanoes. Moreover, it would also be good to examine further the sea-

sonality of the spiral dust cloud over Arsia. This seasonality may be associated with changes in the circulations due to differences in solar heating.

6. References

Albee, A., 2002: The Mars Global Surveyor mission: description, status, and significant result. *Highlights of Astronomy*, **12**, 631-635.

Bagnold, R. A., 1941: *The physics of brown sand and desert dunes*. Methuen & Co. Ltd., London, 265 pp.

Bridges, N. T., 1994: Elevation-corrected thermal inertia and derived particle size on Mars and implications for the Tharsis Montes. *Geophys. Res. Lett.*, **21**, 785-788.

Christensen, P. R., 1988: Global albedo variations on Mars: Implications for active aeolian transport, deposition, and erosion. *J. Geophys. Res.*, **93**, 7611-7624.

Clarke, R. H., 1972: The Morning Glory: An atmospheric hydraulic jump. *J. Appl. Meteor.*, **11**, 304-311.

Conrath, B., R. Curran, R. Hanel, V. Kunde, W. Maguire, J. Pearl, J. Pirraglia, J. Welker, and T. Burke, 1973. Atmospheric and surface properties of Mars obtained by infrared spectroscopy on Mariner 9. *J. Geophys. Res.*, **78**, 4267-4278.

Crook, N. A., and M. J. Miller, 1985: A numerical and analytical study of atmospheric undular bores. *Quart. J. R. Meteor. Soc.*, **111**, 225-242.

Evans, N., 1980: Arsia-Pavonis Bore Wave: Three Mars Years of Observations. *Bull. Amer. Astr. Soc.*, **12**, 74.

Fenton, L. K., and M. I. Richardson, 2001: Martian surface winds: Insensitivity to orbital changes and implications for aolian processes. *J. Geophys. Res.*, **106**, 32885-32902.

Greeley, R., A. Skypeck, and J. B. Pollack, 1993: Martian aeolian features and deposits: Comparisons with general circulation model results. *J. Geophys. Res.*, **98**, 3183-3196.

Greeley, R., M. D. Kraft, R. O. Kuzmin, and N. T. Bridges, 2000: Mars Pathfinder landing site: Evidence for a change in wind regime from lander and orbiter data. *J. Geophys. Res.*, **105**, 1829-1840.

Greeley, R., R. Leach, B. White, J. Iversen, and J. Pollack, 1980: Threshold windspeeds for sand on Mars: Wind tunnel simulations. *Geophys. Res. Lett.*, **7**, 121-124.

Greeley, R., M. Kraft, R. Sullivan, G. Wilson, N. Bridges, K. Herkenhoff, R. O. Kuzmin, M. Malin, and W. Ward, 1999: Aeolian features and processes at the Mars Pathfinder landing site. *J. Geophys. Res.*, **104**, 8573-8584.

Haberle, R. M., J. B. Pollack, J. R. Barnes, R. W. Zurek, C. B. Leovy, J. R. Murphy, H. Lee, and J. Schaeffer, 1993: Mars atmospheric dynamics as simulated by the NASA Ames general circulation model: 1. The zonal-mean circulation. *J. Geophys. Res.*, **98**, 3093-3123.

Haberle, R. M., M. M. Joshi, J. R. Murphy, J. R. Barnes, J. T. Schofield, G. W. Wilson, M. Lopez-Valverde, J. L. Hollingsworth, A. F. C. Bridger, and J. Schaeffer, 1999: General circulation model simulations of the Mars Pathfinder atmospheric structure investigation/meteorology data. *J. Geophys. Res.*, **104**, 8957-8974.

Holyer, J. Y., and H. E. Huppert, 1980: Gravity currents entering a two-layer fluid. *J. Fluid. Mech.*, **100**, 739-767.

Hunt, G. E., A. O. Pickergill, P. B. James, and N. Evans, 1981: Daily and seasonal Viking observations of martian bore wave systems. *Nature*, **293**, 630-633.

Hunt, G. E., A. O. Pickersgill, P. B. James, and G. Johnson, 1980: Some diurnal properties of clouds over martian volcanoes. *Nature*, **286**, 362-364.

Kahn, R., and P. Gierasch, 1982: Long cloud observations on Mars and implications for boundary layer characteristics over slopes. *J. Geophys. Res.*, **87**, 867-880.

Koch, S. E., P. B. Dorian, R. Ferrare, S. H. Melfi, W. C. Skillman, and D. Whiteman, 1991: Structure of an internal bore and dissipating gravity current as revealed by raman lidar. *Mon. Wea. Rev.*, **119**, 857-887.

Lee, S. W., P. C. Thomas, and J. Veverka, 1982: Wind streaks in Tharsis and Elysium: Implications for sediment transport by slope winds. *J. Geophys. Res.*, **87**, 10025-10041.

Locatelli, J. D., M. T. Stoelinga, P. V. Hobbs, and J. Johnson, 1998: Structure and evolution of an undular bore on the high plains and its effects on migrating birds. *Bull. Amer. Meteor. Soc.*, **79**, 1043-1060.

Malin, M., 1998: Mars Orbiter Camera: The first year. *Bull. Amer. Astro. Soc.*, **30**, 1020.

Malin, M, and B. Cantor, 2002: personal communications.

Malin Space Science Systems, 2001: Mars Global Surveyor – Mars Orbiter Camera. [Available on-line at http://www.msss.com]

Martin, T. Z., and H. H. Kieffer, 1979: Thermal infrared properties of the Martian atmosphere. II. The 15-μm band measurements. *J. Geophys. Res.*, **84**, 2843-2852.

Michaels, T. I., 2002: Large eddy simulation of atmospheric convection on Mars. M.S. thesis, Dept. of Meteor., SJSU, 95 pp.

Michaels, T. I., and S. C. R. Rafkin, 2002: Large eddy simulation of the convective boundary layer of Mars. *Quart. J. Roy. Meteor. Soc.*, submitted.

Magalhaes, J., and P. Gierasch, 1982: A model of martian slope winds: Implications for eolian transport. *J. Geophys. Res.*, **87**, 9975-9984.

Magalhaes, J.A., and R. E. Young, 1995: Downslope windstorms in the lee of ridges on Mars. *Icarus*, **113**, 277-294.

Mars Orbiter Laser Altimeter (MOLA) Science Investigation, 2001: Mapping and Extended Mission Results. [Available on-line at http://ltpwww.gsfc.nasa.gov/tharsis/mapping_results.html]

Murphy, J., 2001: personal communications.

Pelkey, S. M., B. M. Jakosky, and M. T. Mellon, 2001: Thermal inertia of crater-related wind streaks on Mars. *J. Geophys. Res.*, **106**, 23909-23920.

Peterfreund, A. R., 1981: Visual and infrared observations of wind streaks on Mars. *Icarus*, **45**, 447-467.

Pickersgill, A. O., 1984: Martian bore waves of the Tharsis region: A comparison with Australian atmospheric waves of elevation. *J. Atmos. Sci.*, **41**, 1461-1473.

Planetary Data System, 2001: Planetary Data System Imaging Node. [Available on-line at http://www-pdsimage.jpl.nasa.gov/PDS/]

Rafkin, S. C. R., R. M. Haberle, and T. I. Michaels, 2001: The Mars regional atmospheric Modeling system: Model description and selected simulations. *Icarus*, **151**, 228-256.

Rafkin, S. C. R., M. R. V. Sta. Maria, and T. I. Michaels, 2002: Simulation of the atmospheric thermal circulation of a martian volcano using a mesoscale numerical model. *Nature*, **419**, 697-698.

Rottman, J. W., and J. E. Simpson, 1989: The formation of internal bores in the atmosphere: A laboratory model. *Quart. J. Roy. Meteor. Soc.*, **115**, 941-963.

Sagan, C., D. Pierl, P. Fox, R. E. Arvidson, and E. A. Guinness, 1977: Particle motion on Mars inferred from the Viking lander cameras. *J. Geophys. Res.*, **82**, 4430-4438.

Sagan, C., J. Veverka, P. Fox, R. Dubisch, J. Lederberg, E. Levinthal, L. Quam, R. Tucker, J. B. Pollack, and B. A. Smith, 1972: Variable features on Mars: Preliminary Mariner 9 television results. *Icarus*, **17**, 346-372.

Sagan, C., J. Veverka, P. Fox, R. Dubisch, R. French, P. Gierasch, L. Quam, J. Lederberg, E. Levinthal, R. Tucker, B. Eross, and J. B. Pollack, 1973: Variable features on Mars: 2. Mariner 9 global results. *J. Geophys. Res.*, **78**, 4163-4196.

Sandoval, J, E. Jensen, K.Supulver, K. Edgett, S. Davis, W. Gross, R. Zimdar, L. Posiolova, M. Caplinger, J. Warren, and M. Malin, 2000: Observing Mars with MOC. Presented, American Astronomical Society Meeting 197, #50.08.

Siili, T., 1996: Modeling of albedo and thermal inertia induced mesoscale circulations in the midlatitude summertime Martian atmosphere. *J. Geophys. Res.*, **101**, 14957-14968.

Siili, T., D. S. Bass, and H. Savijärvi, 2000: On mesoscale circulations amd water transport around the northern polar cap.

Simpson, J. E., 1997: *Gravity currents in the environment and the laboratory.* 2nd Ed., Cambridge University Press, 244 pp.

Snyder, C. W., and V. I. Moroz, 1992: *Mars*. Chapter 3: Spacecraft exploration of Mars. The University of Arizona Press, Tucson, 71-119.

Thomas, P., and J. Veverka, 1979: Seasonal and secular variation of wind streaks on Mars: An analysis of Mariner 9 and Viking data. *J. Geophys. Res.*, **84**, 8131-8146.

Thomas, P., J. Veverka, D. Gineris, and L. Wong, 1984: "Dust" streaks on Mars. *Icarus*, **60**, 161-179.

Thomas, P., J. Veverka, S. Lee, and A. Bloom, 1981: Classification of wind streaks on Mars. *Icarus*, **45**, 124-153.

Toigo, A. D., and M. I. Richardson, 1999: Polar cap edge circulations in a 3D martian mesoscale model.

Veverka, J., 1975: Variable features on Mars V: Evidence for crater streaks produced by wind erosion. *Icarus*, **25**, 595-601.

Veverka, J., P. Gierasch, and P. Thomas, 1981: Wind streaks on Mars: Meteorological control of occurrence and mode of formation. *Icarus*, **45**, 154-166.

Wakimoto, R. M., and D. E. Kingsmill, 1995: Structure of an atmospheric undular bore

generated from colliding boundaries during CaPE. *Mon. Wea. Rev.*, **123**, 1374-1393.

Williams, S. H., 1997: The Winds of Mars: Aeolian Activity and Landforms. [Available online at http://www.lpi.usra.edu/publications/slidesets/winds.html]

Ye, Z. J., M. Segal, and R. A. Pielke, 1990: A comparative study of daytime thermally induced upslope flow on Mars and Earth. *J. Atmos. Sci.*, **47**, 612-628.

Young, R. S., 1978: Viking - The exploration of Mars. Presented, *Proceedings of the Second ISSOL Meeting and Fifth ICOL Meeting*, Kyoto, Japan, 6 pp.

Zurek, R. W., 1992: *Mars*. Chapter 24: Comparative aspects of the climate of Mars: An introduction to the current atmosphere. The University of Arizona Press, Tucson, 799-817.

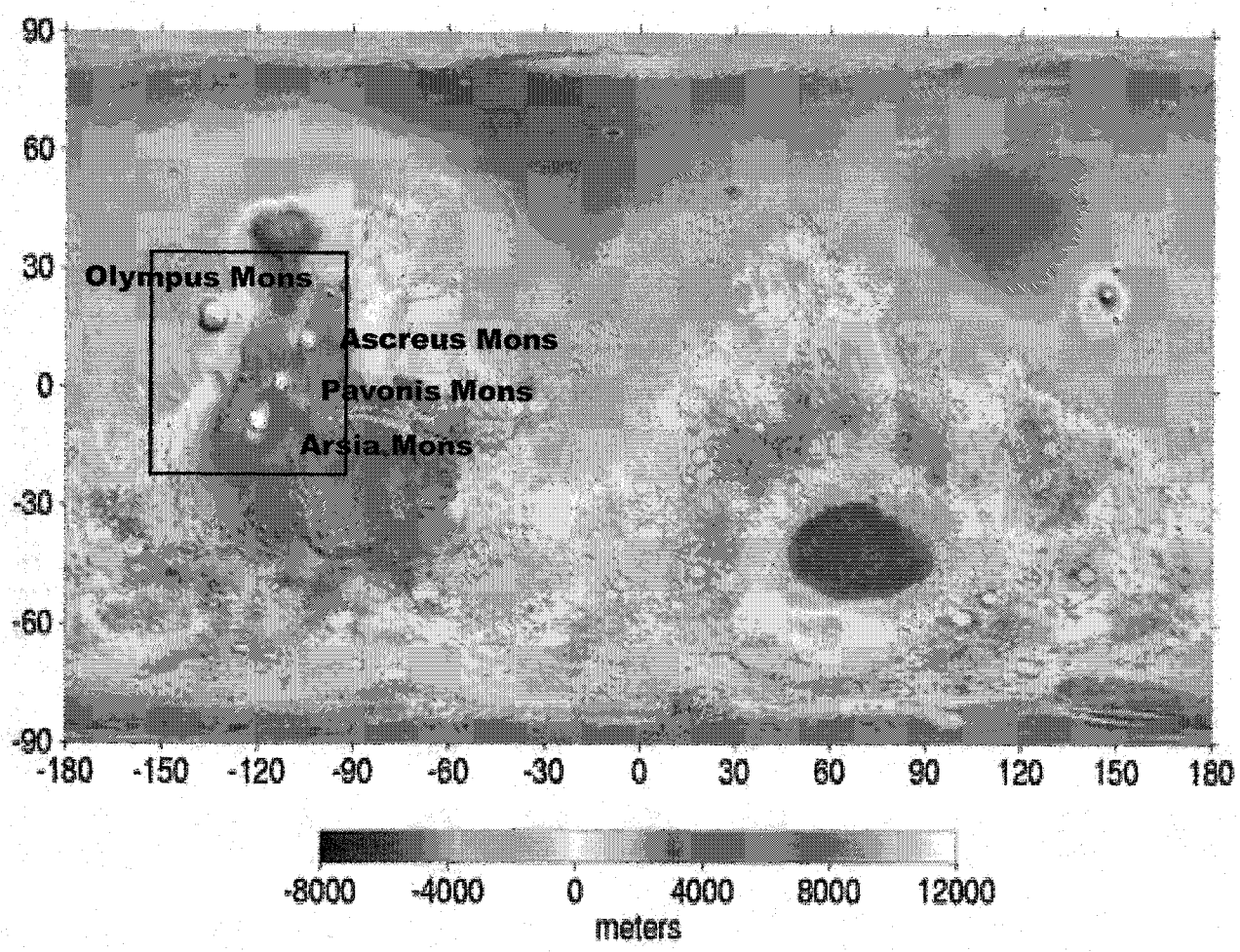
90
60
30
0
-30
-60
-90
Olympus Mons
Ascreus Mons
Pavonis Mons
Arsia Mons
-180
-150
-120
-90
-60
-30
0
30
60
90
120
150
180
-8000
-4000
0
4000
8000
12000
meters

Fig. 1


A
MOC2-111 Malin Space Science Systems/NASA

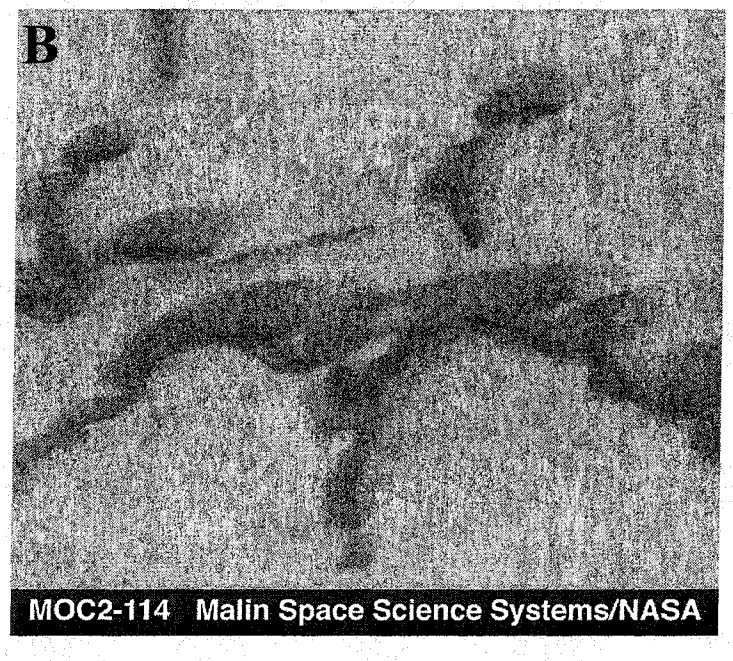
B
MOC2-114 Malin Space Science Systems/NASA

Fig. 2

A

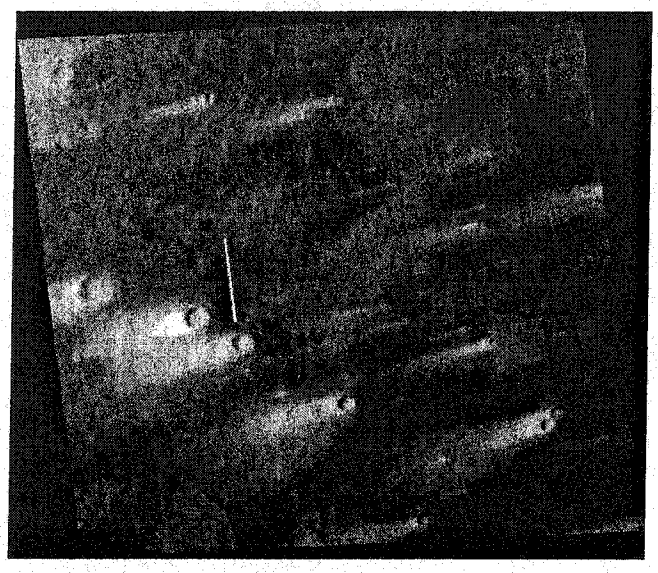

B

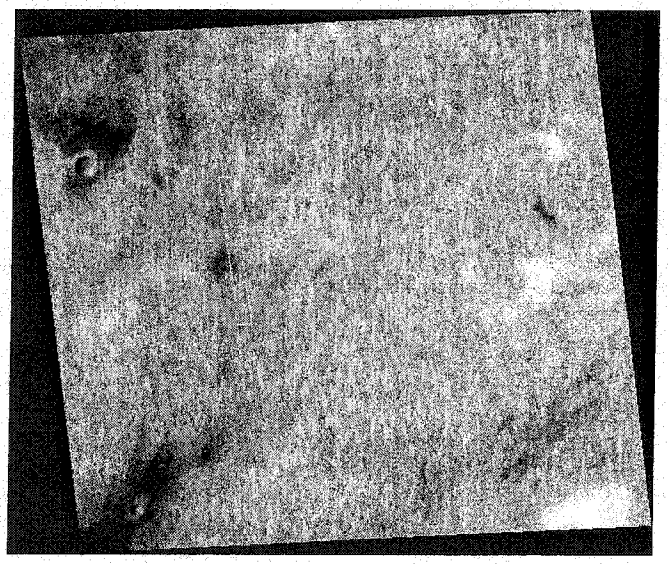

Fig. 3

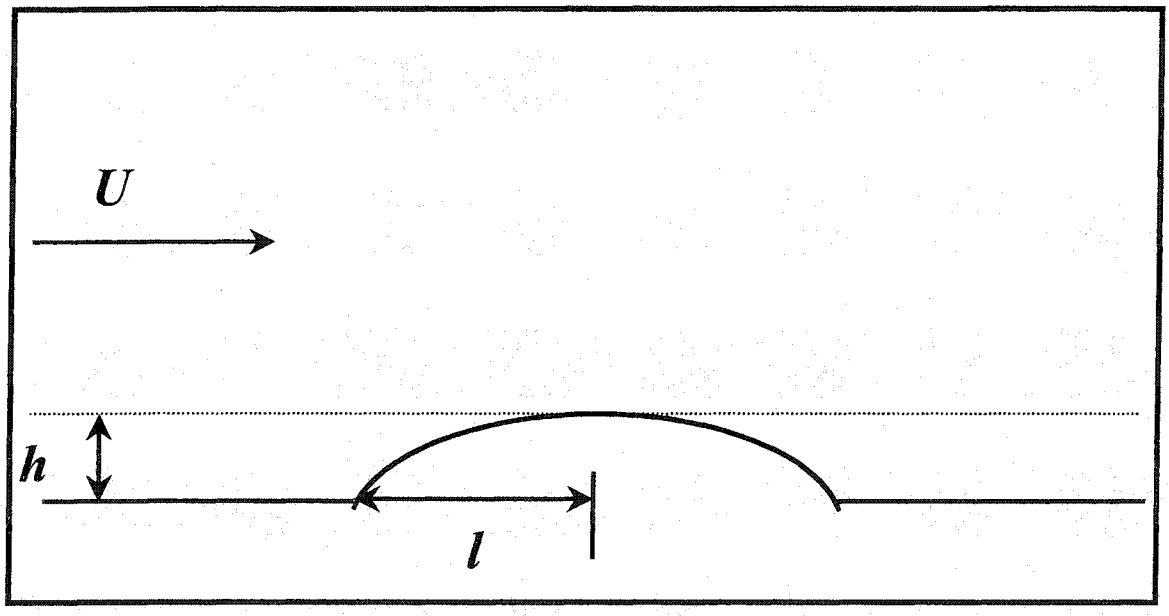

Fig. 4

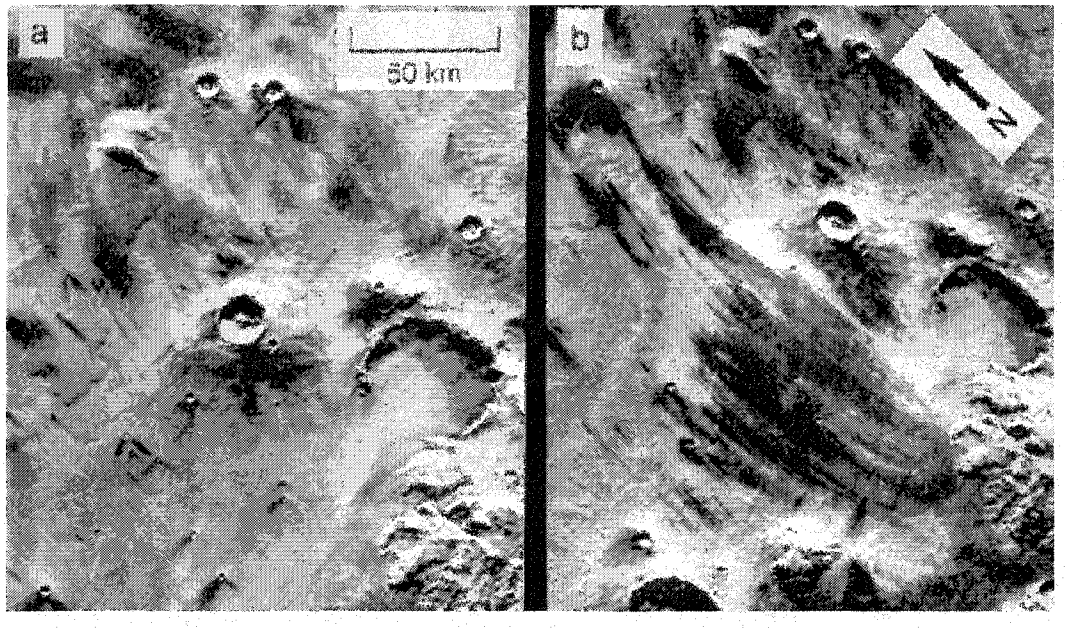

Fig. 5

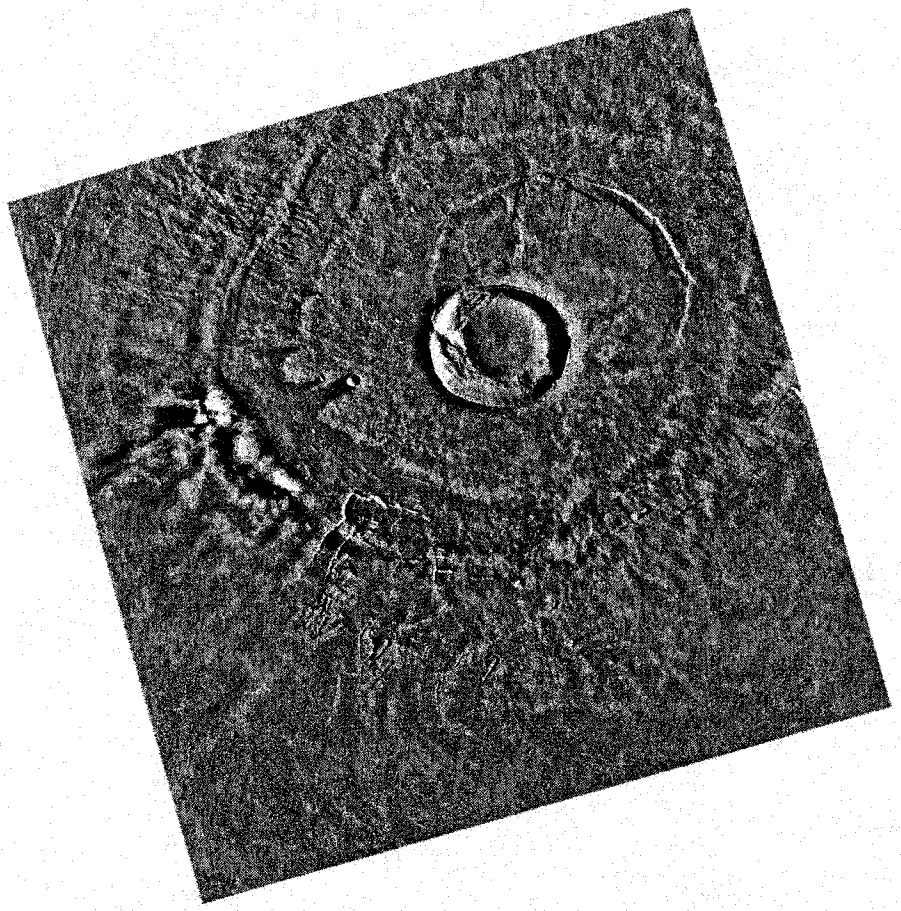

Fig. 6

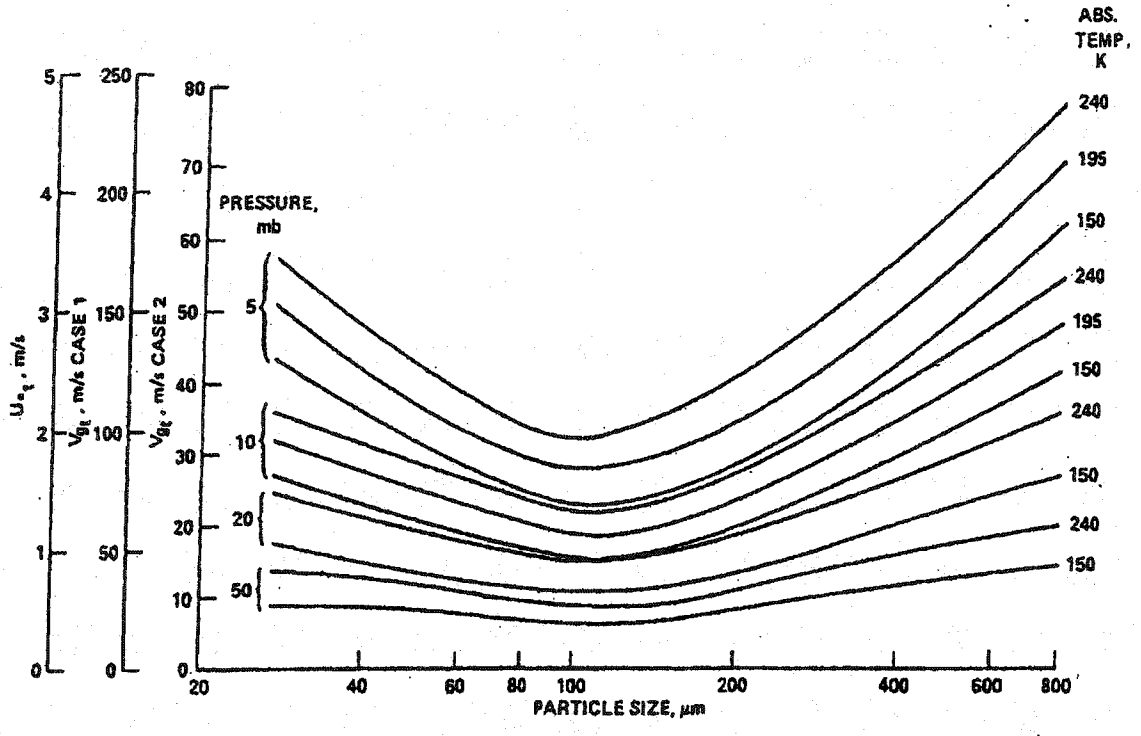
ABS. TEMP, K
240
195
150
240
195
150
240
150
240
150
PRESSURE, mb
5
10
20
50
U_{s_t}, m/s
V_{gt}, m/s CASE 1
V_{gt}, m/s CASE 2
PARTICLE SIZE, μm
20
40
60
80
100
200
400
600
800

Fig. 7

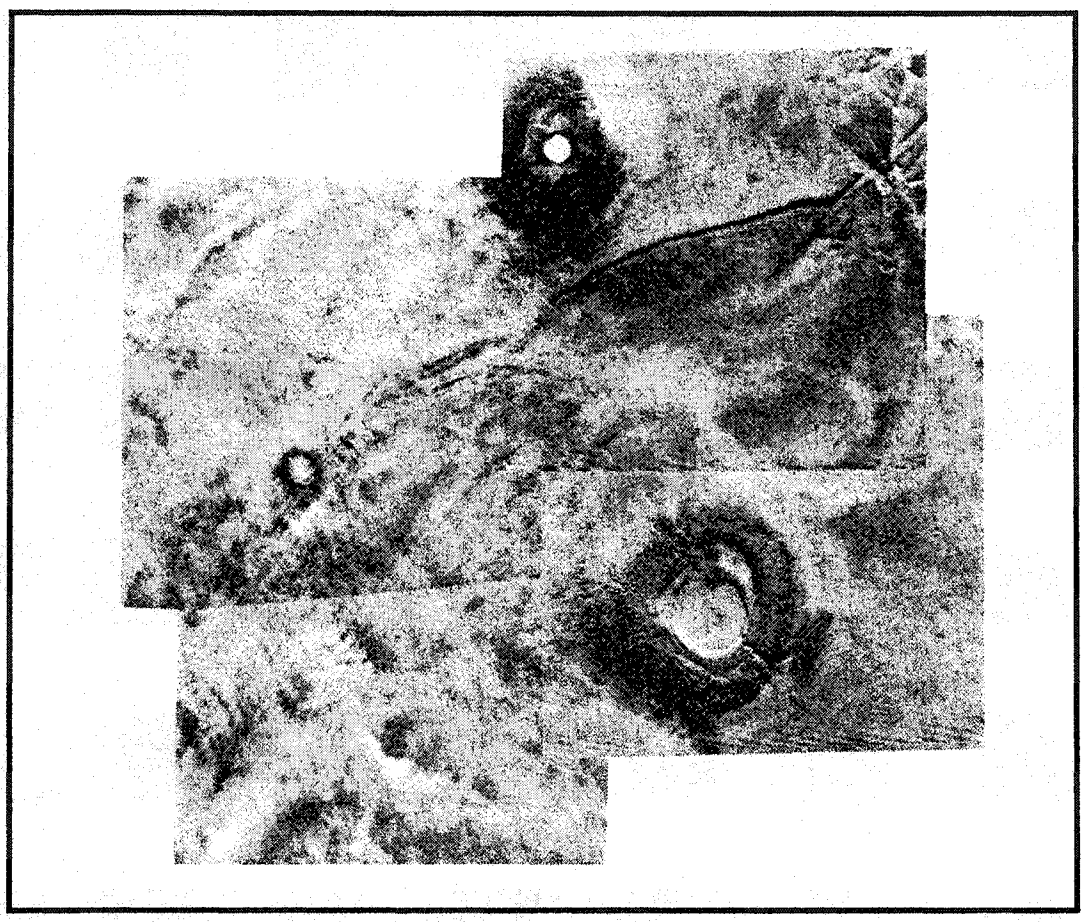

Fig. 8

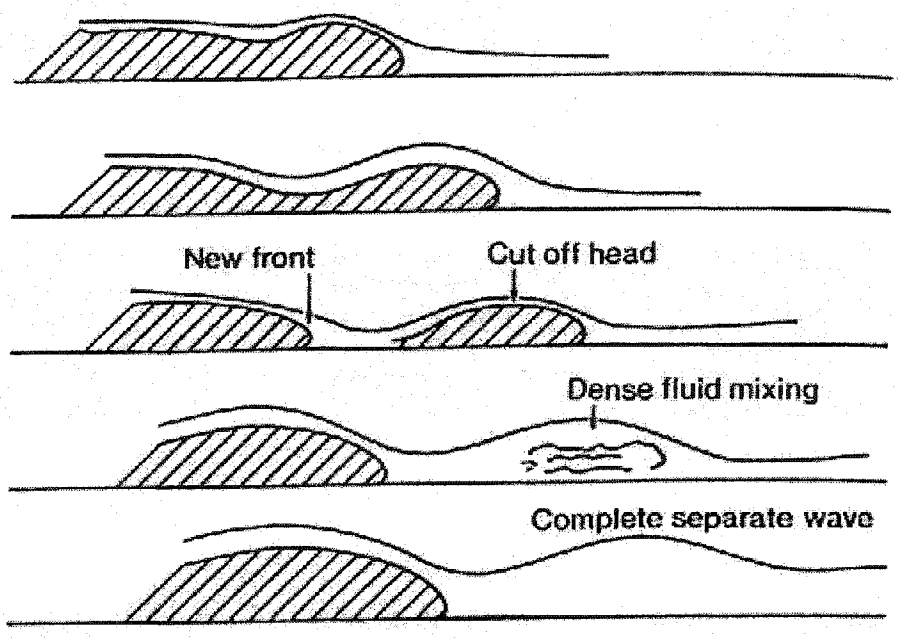
New front
Cut off head
Dense fluid mixing
Complete separate wave

Fig. 9

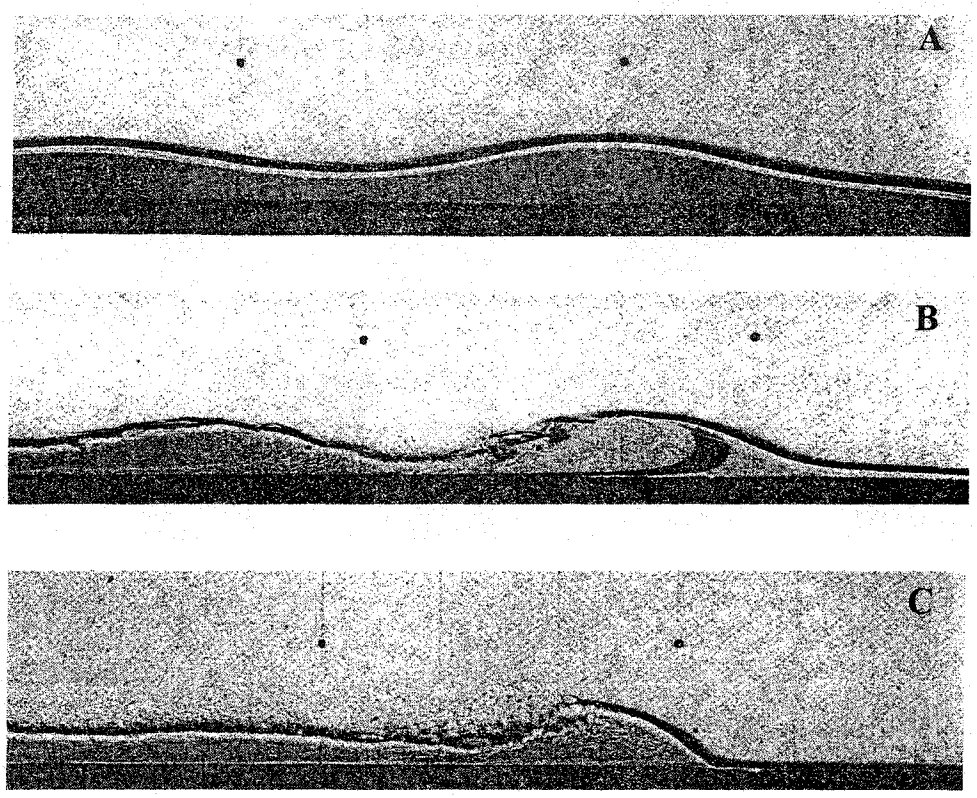

Fig. 10

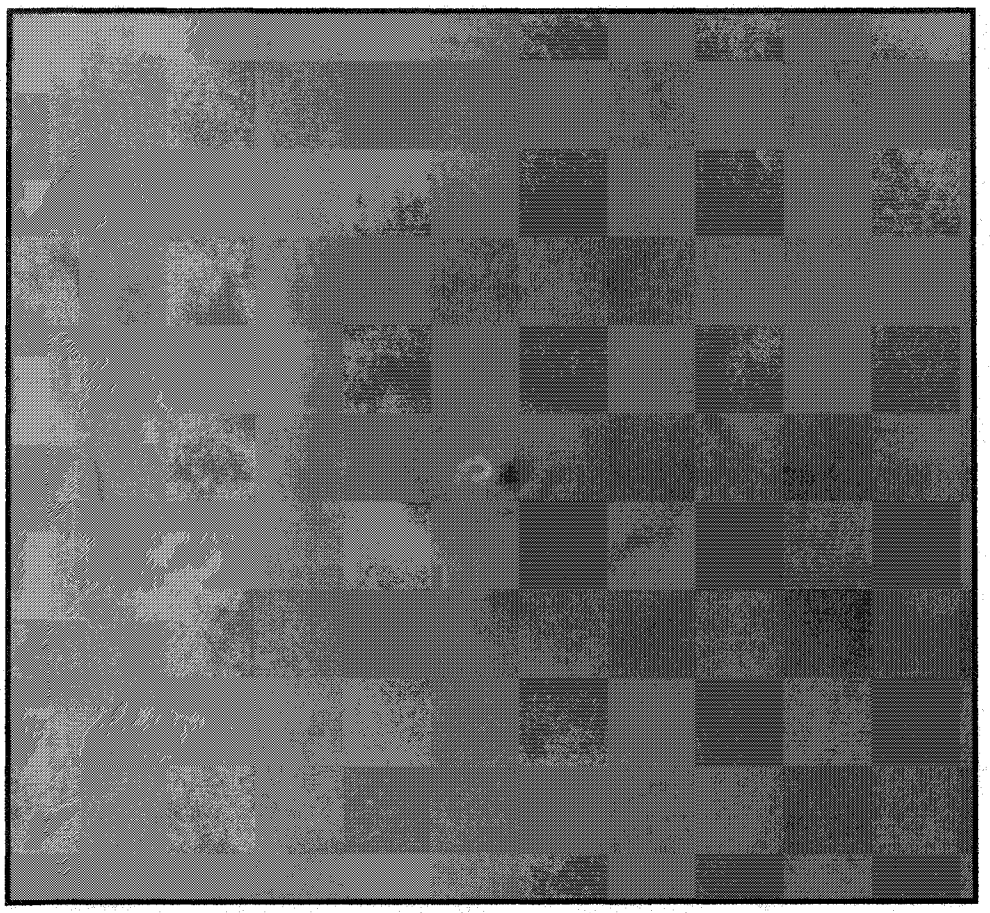

Fig. 11

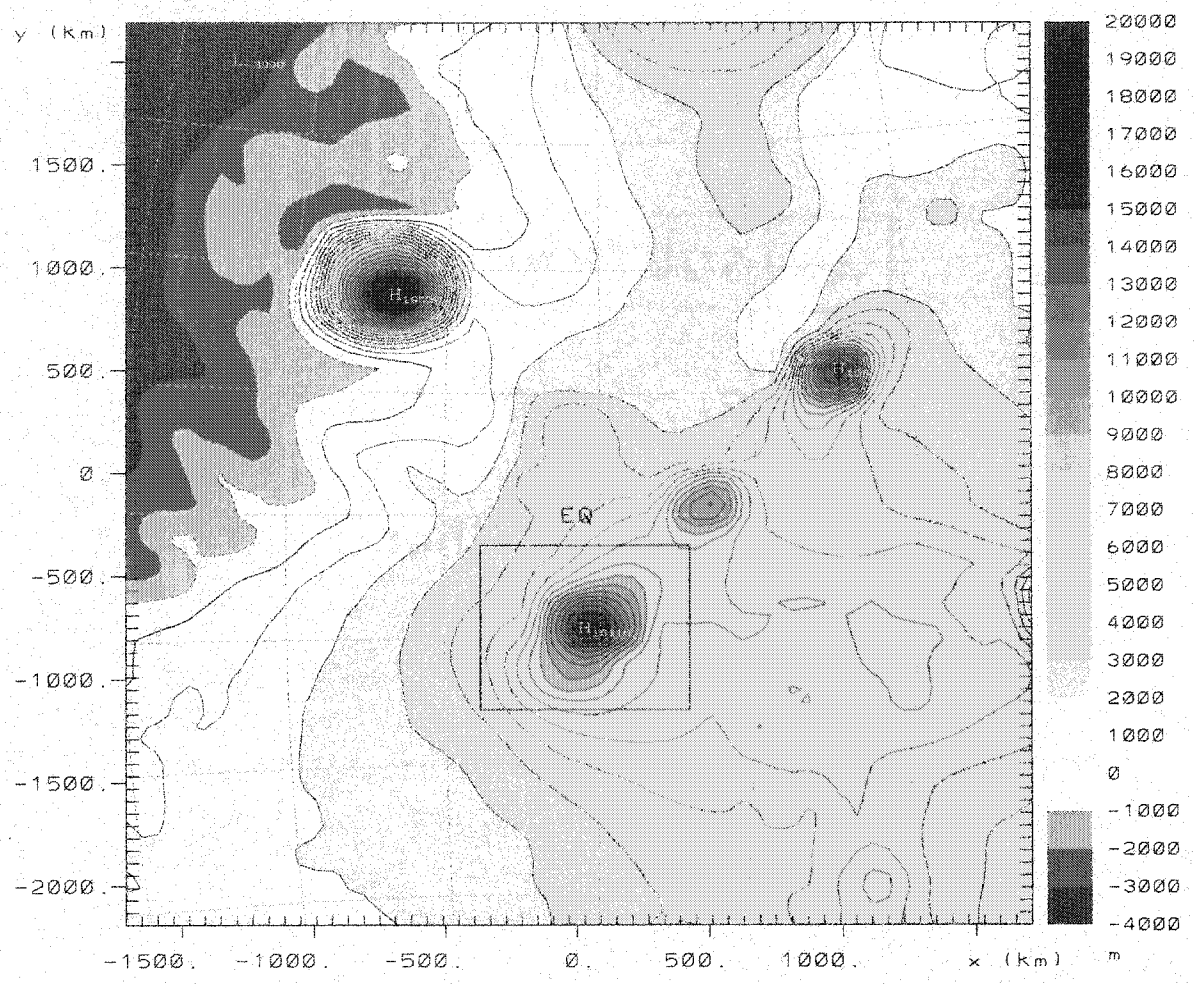
y (km)
1500.
1000.
500.
0
-500.
-1000.
-1500.
-2000.
EQ
-1500.
-1000.
-500.
0.
500.
1000.
x (km)
20000
19000
18000
17000
16000
15000
14000
13000
12000
11000
10000
9000
8000
7000
6000
5000
4000
3000
2000
1000
0
-1000
-2000
-3000
-4000
m

Fig. 12

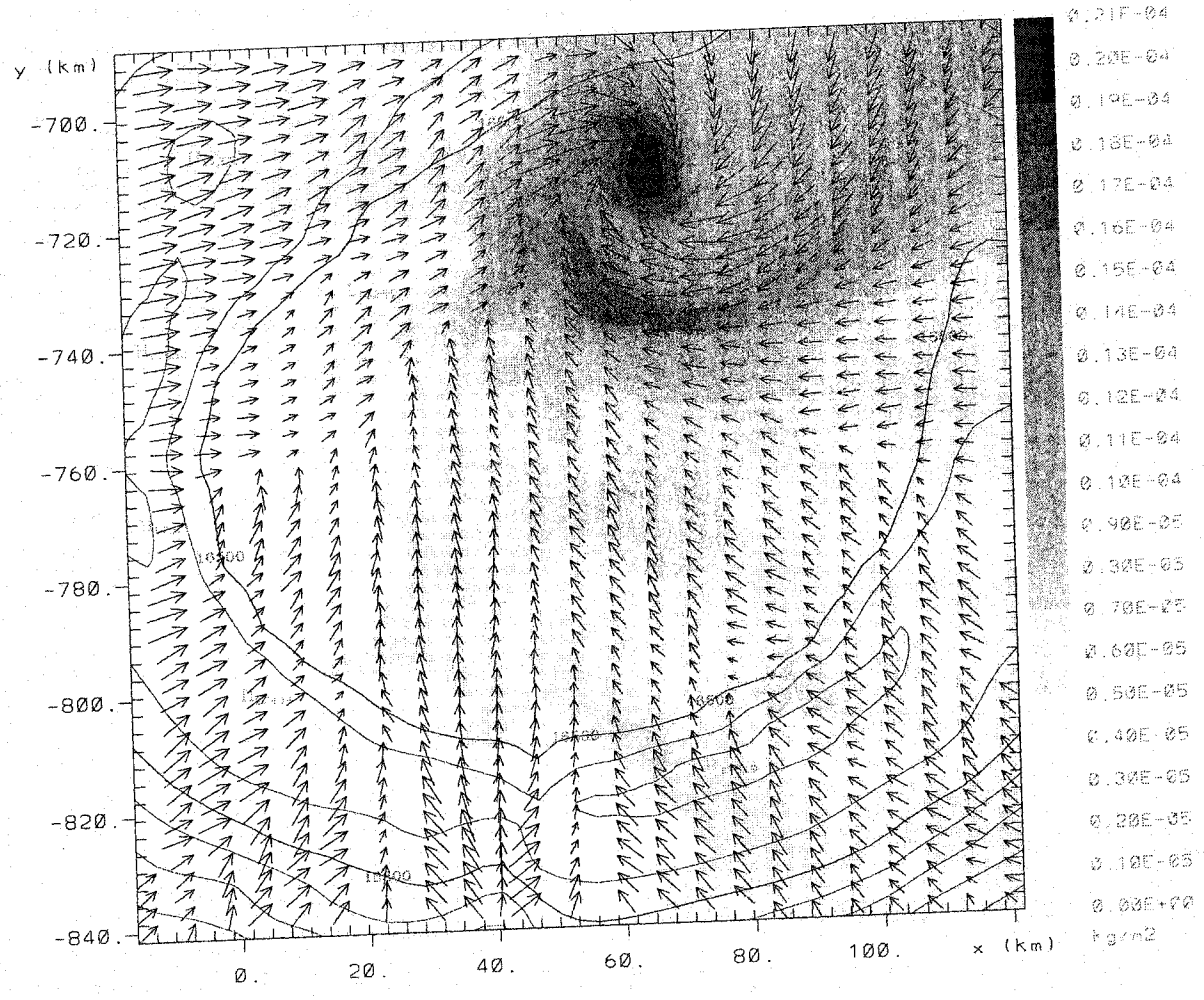
y (km)
-700.
-720.
-740.
-760.
-780.
-800.
-820.
-840.
0.
20.
40.
60.
80.
100.
x (km)
0.21E-04
0.20E-04
0.19E-04
0.18E-04
0.17E-04
0.16E-04
0.15E-04
0.14E-04
0.13E-04
0.12E-04
0.11E-04
0.10E-04
0.90E-05
0.80E-05
0.70E-05
0.60E-05
0.50E-05
0.40E-05
0.30E-05
0.20E-05
0.10E-05
0.00E+00
kg/m2

Fig. 13a

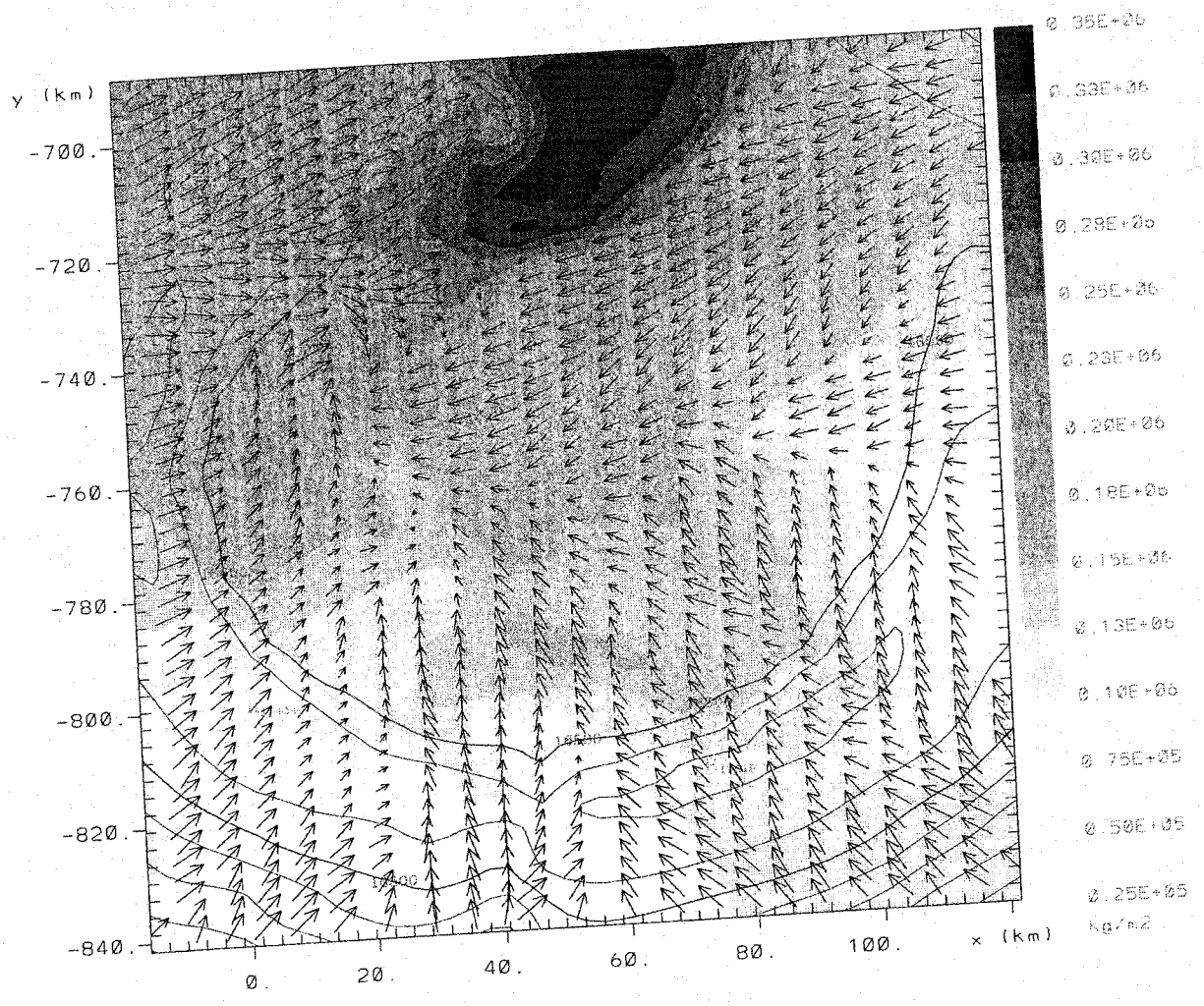
y (km)
-700.
-720.
-740.
-760.
-780.
-800.
-820.
-840.
0.
20.
40.
60.
80.
100.
x (km)
0.35E+06
0.33E+06
0.30E+06
0.28E+06
0.25E+06
0.23E+06
0.20E+06
0.18E+06
0.15E+06
0.13E+06
0.10E+06
0.75E+05
0.50E+05
0.25E+05
kg/m2

Fig. 13b

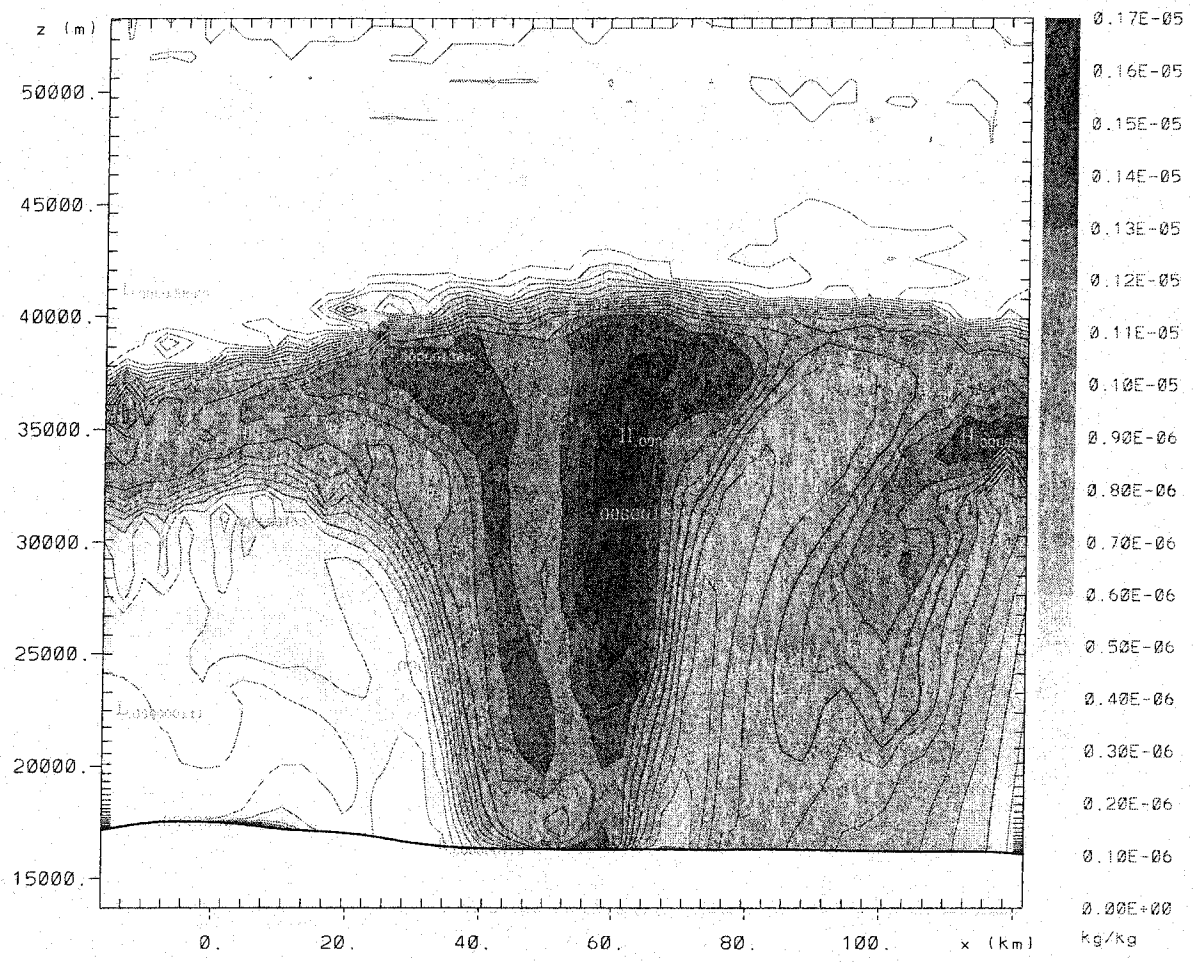
z (m)
50000.
45000.
40000.
35000.
30000.
25000.
20000.
15000.
0.
20.
40.
60.
80.
100.
x (km)
0.17E-05
0.16E-05
0.15E-05
0.14E-05
0.13E-05
0.12E-05
0.11E-05
0.10E-05
0.90E-06
0.80E-06
0.70E-06
0.60E-06
0.50E-06
0.40E-06
0.30E-06
0.20E-06
0.10E-06
0.00E+00
kg/kg

Fig. 14

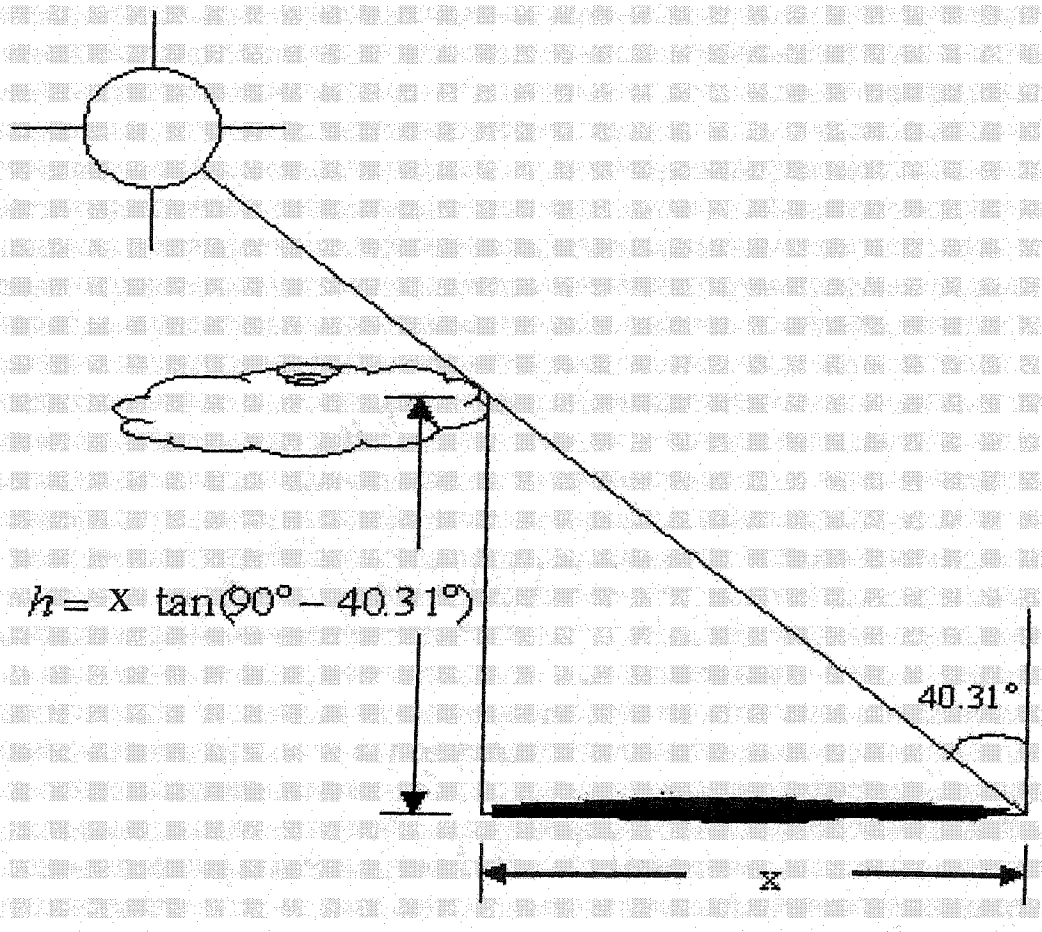

Fig. 15

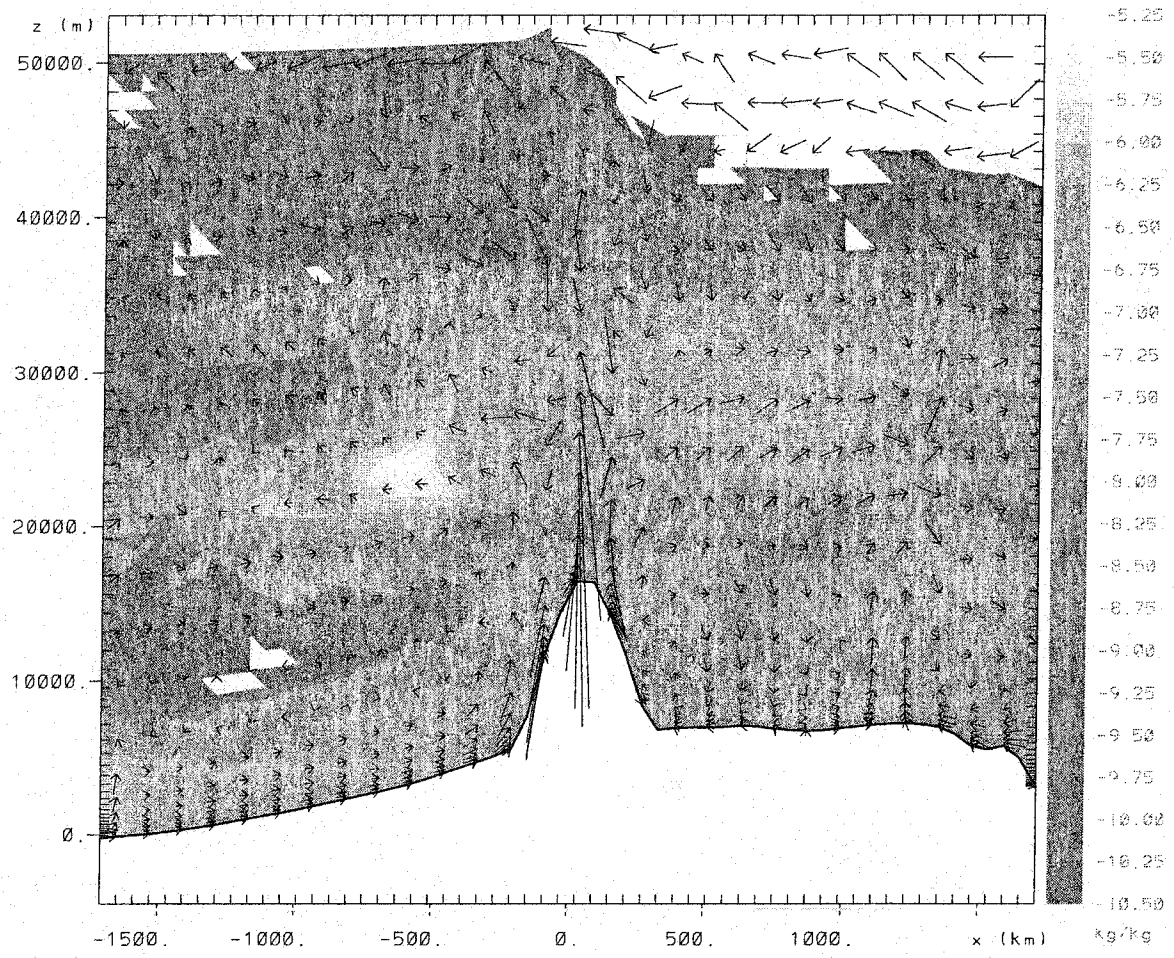
z (m)
50000.
40000.
30000.
20000.
10000.
0.
-1500.
-1000.
-500.
0.
500.
1000.
x (km)
-5.25
-5.50
-5.75
-6.00
-6.25
-6.50
-6.75
-7.00
-7.25
-7.50
-7.75
-8.00
-8.25
-8.50
-8.75
-9.00
-9.25
-9.50
-9.75
-10.00
-10.25
-10.50
kg/kg

Fig. 16

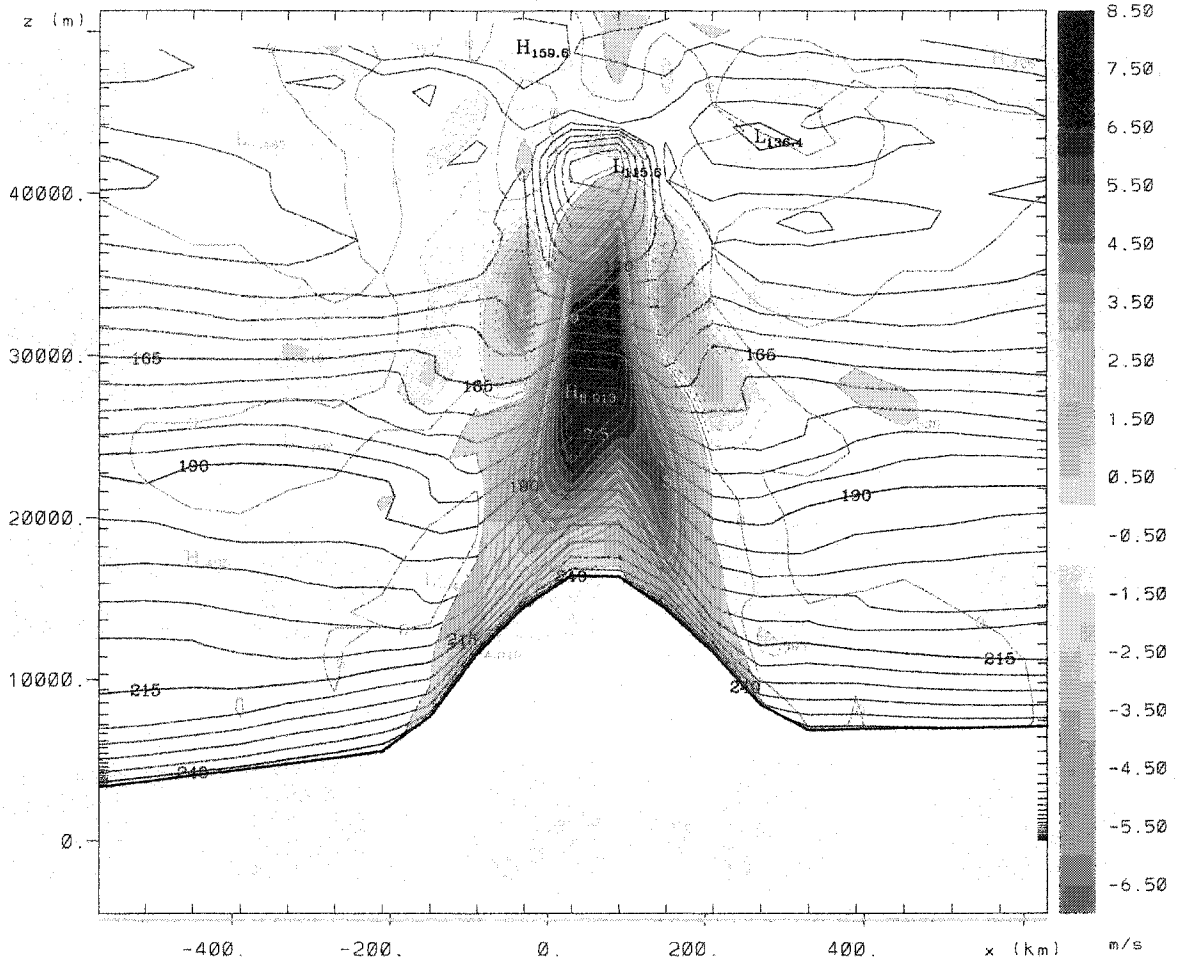
z (m)
40000.
30000.
20000.
10000.
0.
-400.
-200.
0.
200.
400.
x (km)
m/s
8.50
7.50
6.50
5.50
4.50
3.50
2.50
1.50
0.50
-0.50
-1.50
-2.50
-3.50
-4.50
-5.50
-6.50
H159.6
L136.4
L115.6
165
166
185
190
215
240

Fig. 17

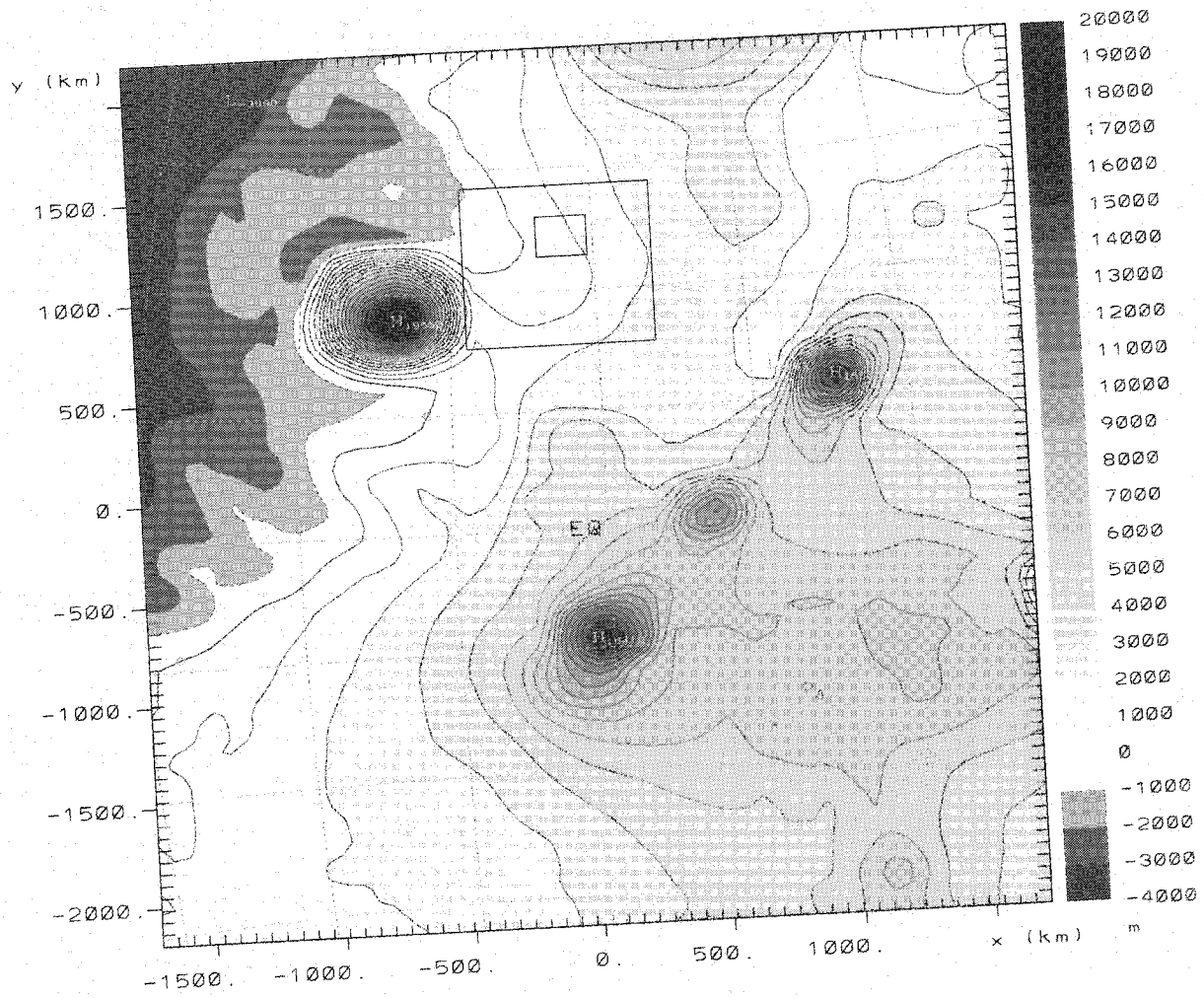
y (Km)
1500.
1000.
500.
0.
-500.
-1000.
-1500.
-2000.
-1500.
-1000.
-500.
0.
500.
1000.
x (km)
20000
19000
18000
17000
16000
15000
14000
13000
12000
11000
10000
9000
8000
7000
6000
5000
4000
3000
2000
1000
0
-1000
-2000
-3000
-4000
m

Fig. 18

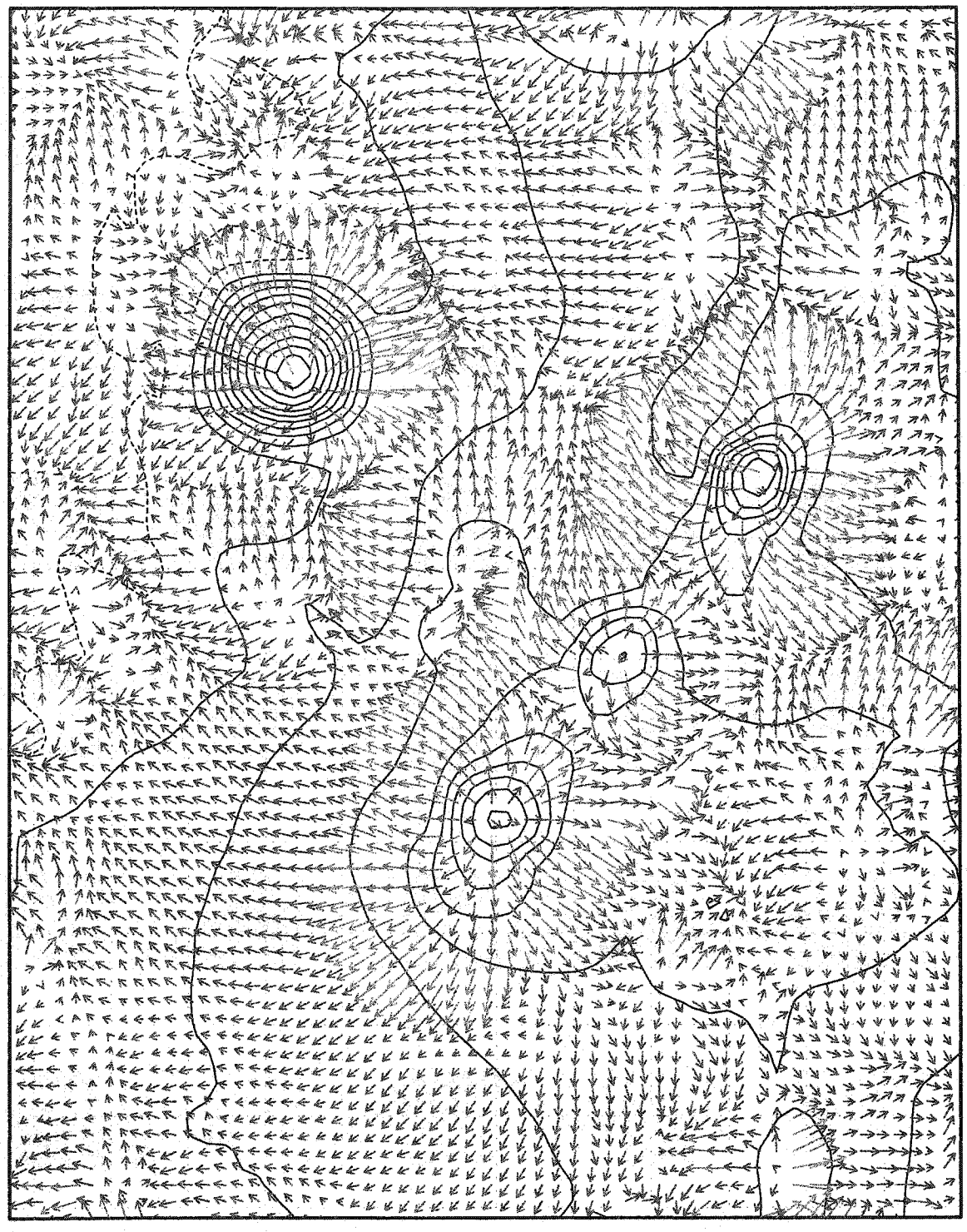

Fig. 19

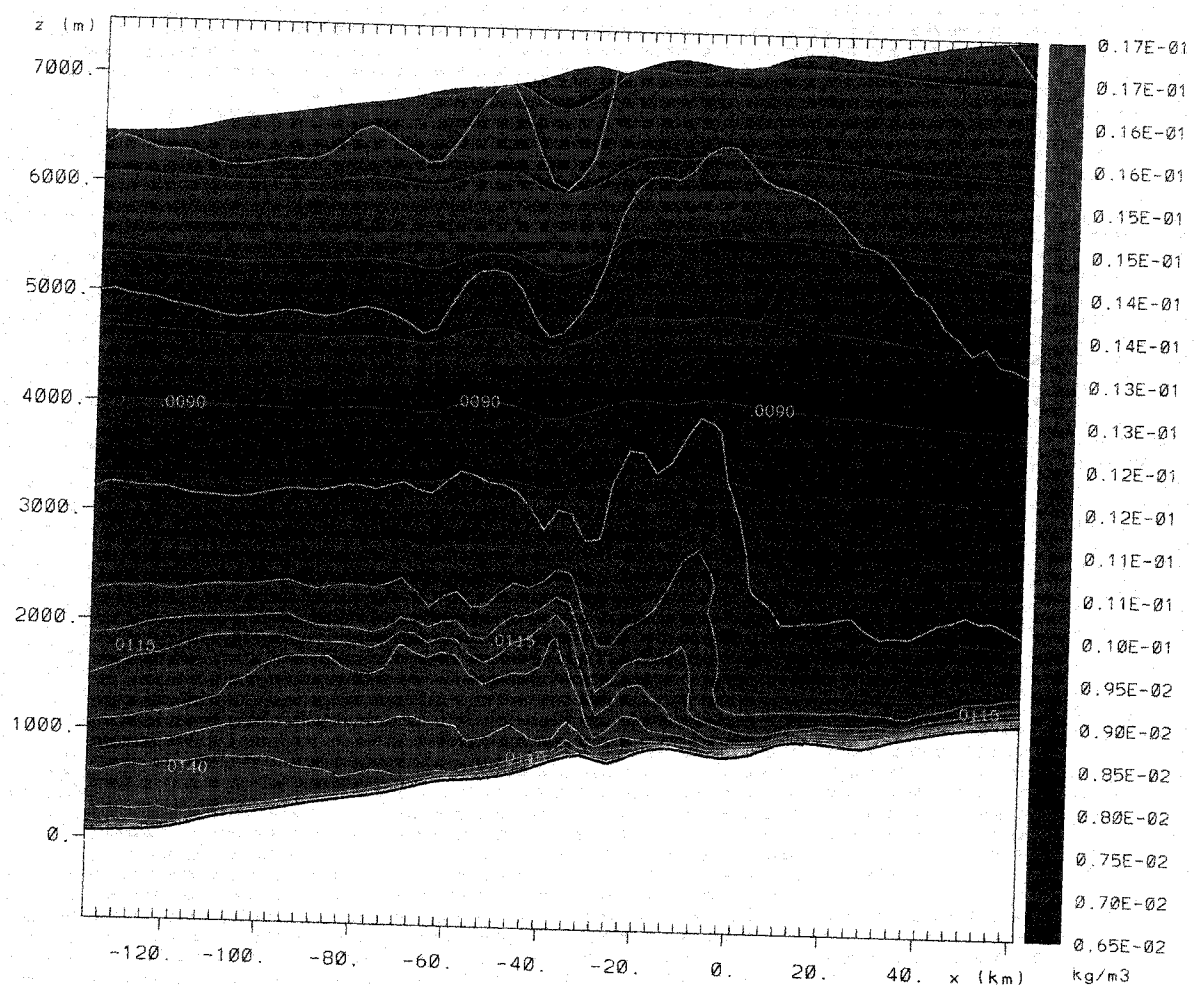
z (m)
7000.
6000.
5000.
4000.
3000.
2000.
1000.
0.
0090
0090
0090
0115
0115
0140
-120.
-100.
-80.
-60.
-40.
-20.
0.
20.
40.
x (km)
0.17E-01
0.17E-01
0.16E-01
0.16E-01
0.15E-01
0.15E-01
0.14E-01
0.14E-01
0.13E-01
0.13E-01
0.12E-01
0.12E-01
0.11E-01
0.11E-01
0.10E-01
0.95E-02
0.90E-02
0.85E-02
0.80E-02
0.75E-02
0.70E-02
0.65E-02
kg/m3

Fig. 20a

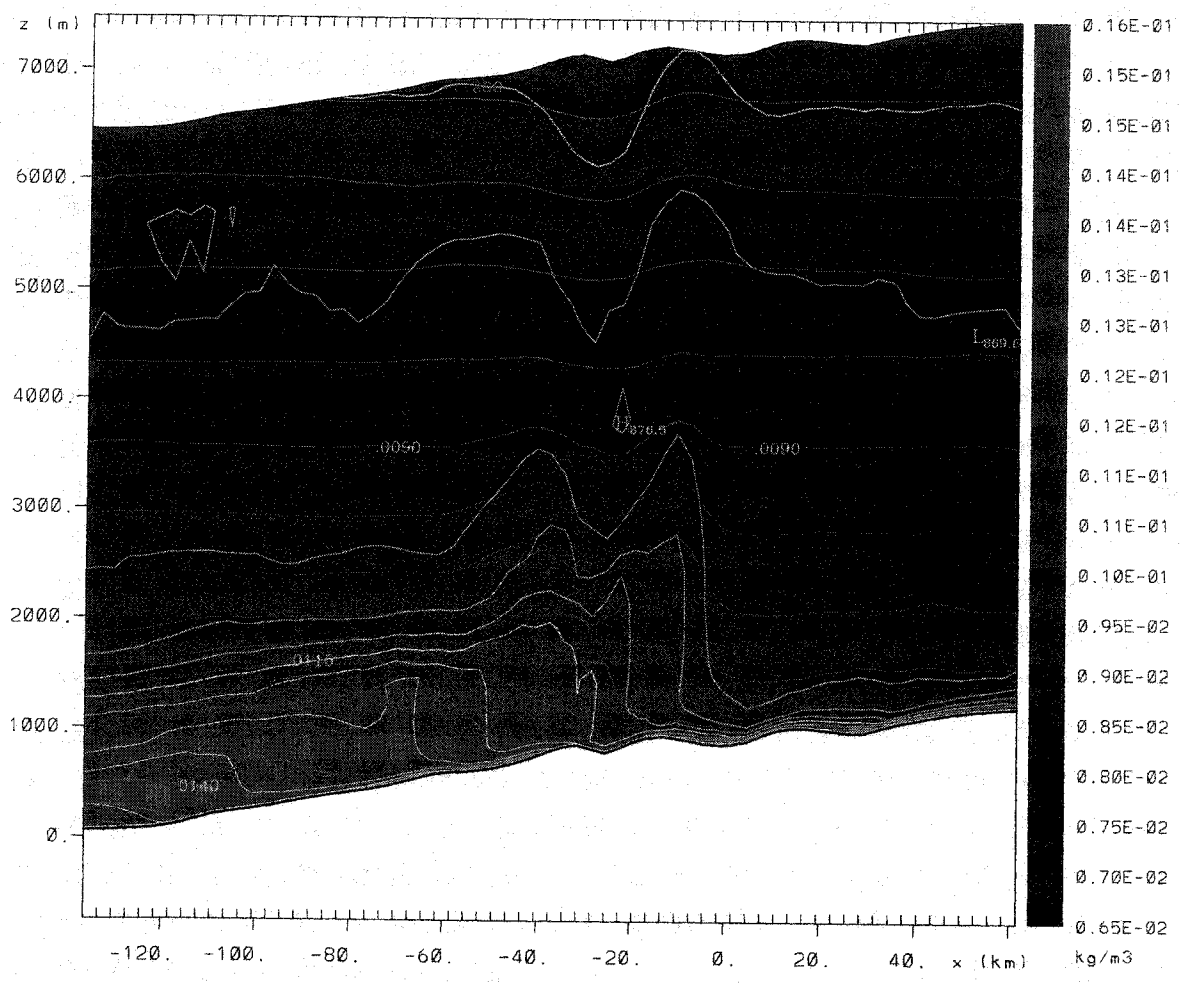
z (m)
7000.
6000.
5000.
4000.
3000.
2000.
1000.
0.
-120.
-100.
-80.
-60.
-40.
-20.
0.
20.
40.
x (km)
0.16E-01
0.15E-01
0.15E-01
0.14E-01
0.14E-01
0.13E-01
0.13E-01
0.12E-01
0.12E-01
0.11E-01
0.11E-01
0.10E-01
0.95E-02
0.90E-02
0.85E-02
0.80E-02
0.75E-02
0.70E-02
0.65E-02
kg/m3

Fig. 20b

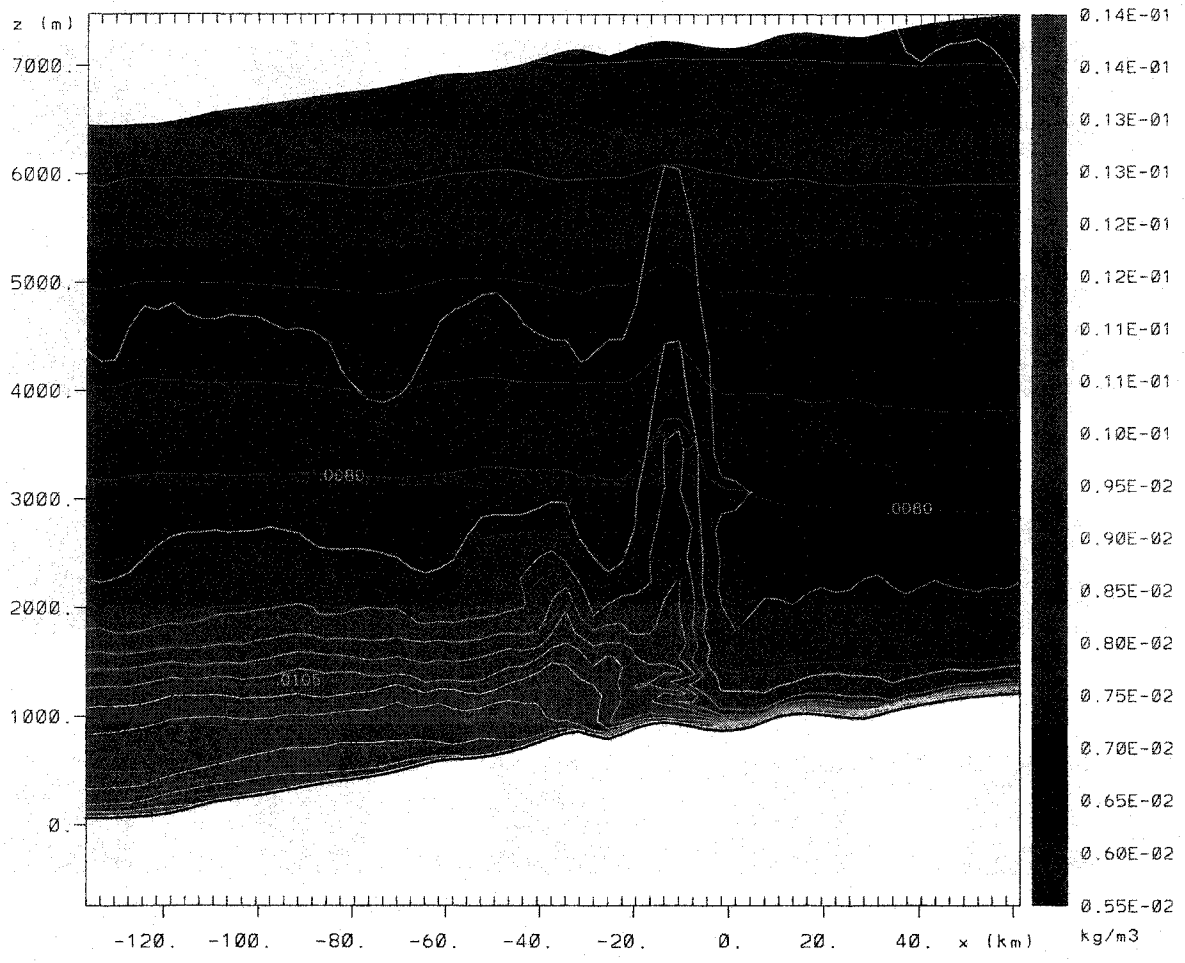
z (m)
7000.
6000.
5000.
4000.
3000.
2000.
1000.
0.
-120.
-100.
-80.
-60.
-40.
-20.
0.
20.
40.
x (km)
0.14E-01
0.14E-01
0.13E-01
0.13E-01
0.12E-01
0.12E-01
0.11E-01
0.11E-01
0.10E-01
0.95E-02
0.90E-02
0.85E-02
0.80E-02
0.75E-02
0.70E-02
0.65E-02
0.60E-02
0.55E-02
kg/m3

Fig. 20c

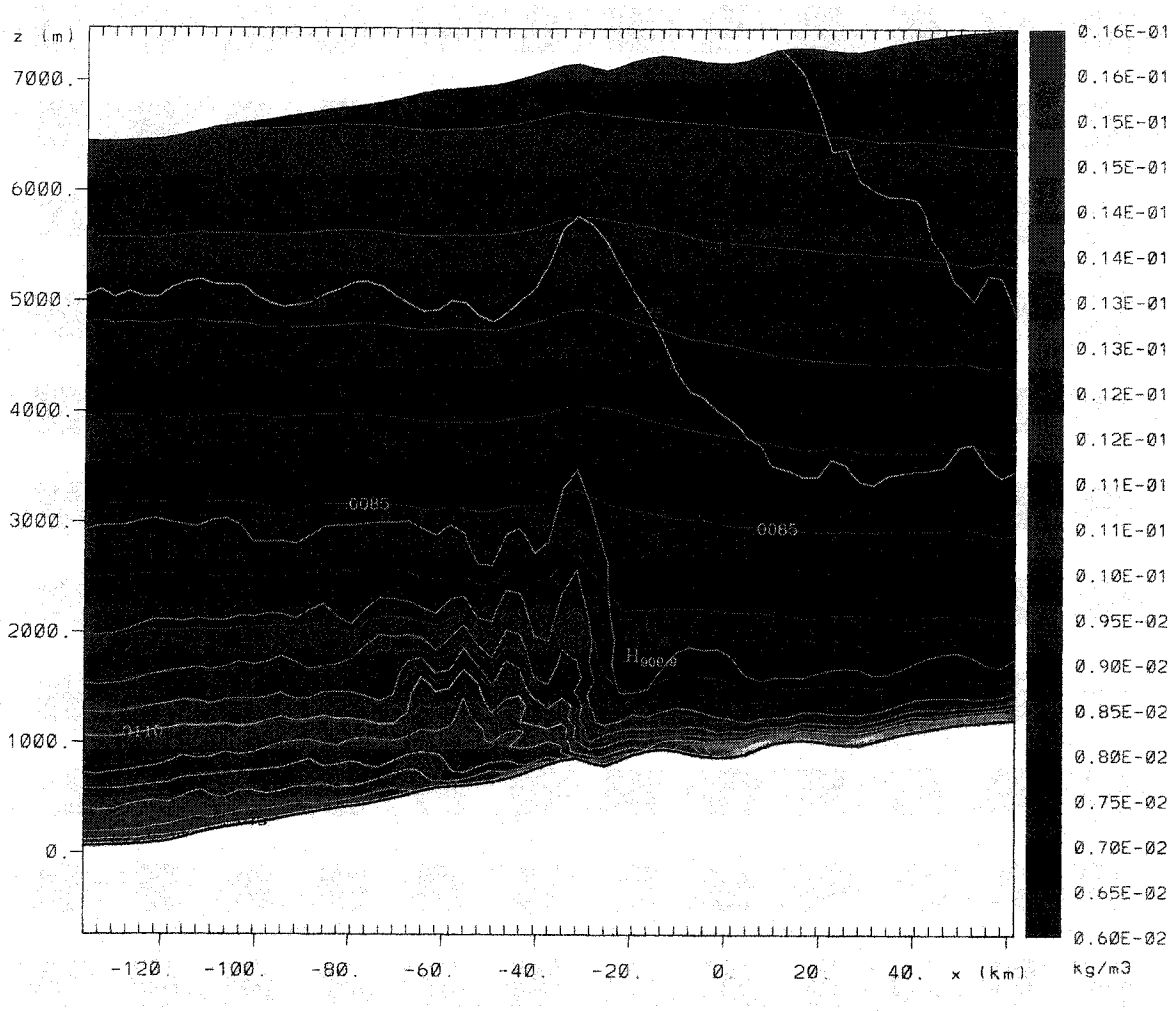
z (m)
7000.
6000.
5000.
4000.
3000.
2000.
1000.
0.
-120.
-100.
-80.
-60.
-40.
-20.
0.
20.
40.
x (km)
0.16E-01
0.16E-01
0.15E-01
0.15E-01
0.14E-01
0.14E-01
0.13E-01
0.13E-01
0.12E-01
0.12E-01
0.11E-01
0.11E-01
0.10E-01
0.95E-02
0.90E-02
0.85E-02
0.80E-02
0.75E-02
0.70E-02
0.65E-02
0.60E-02
kg/m3

Fig. 20d

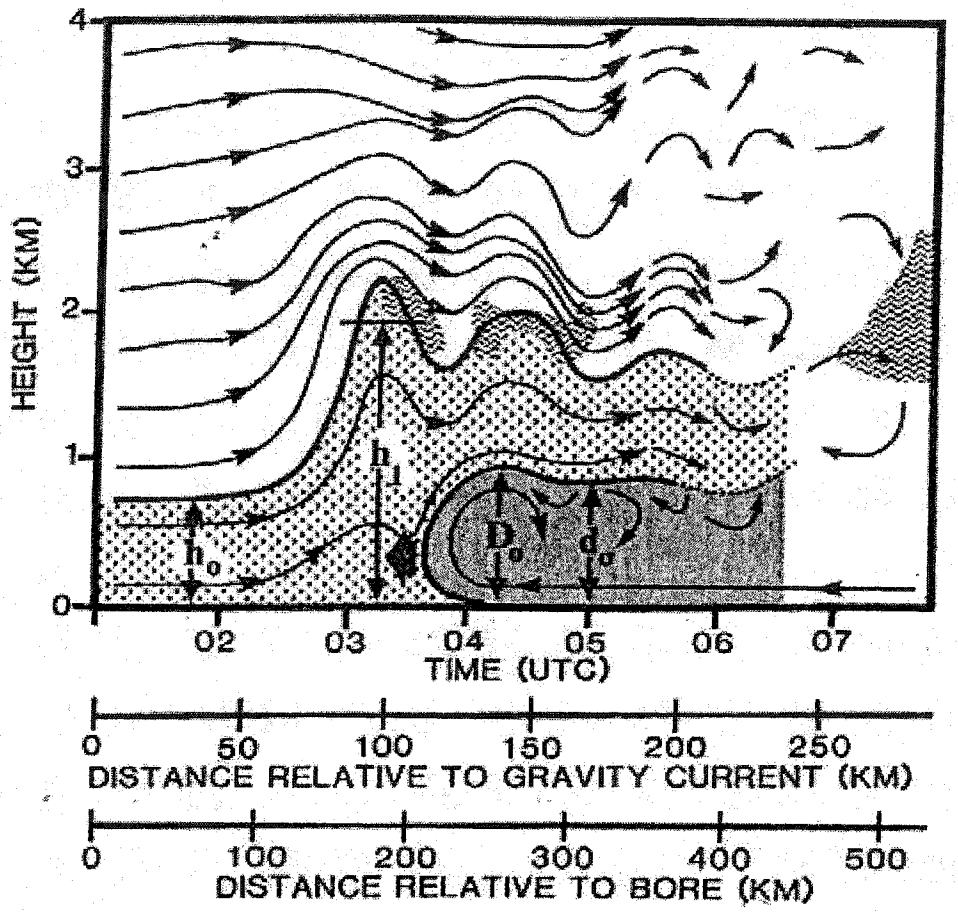
HEIGHT (KM)
4
3
2
1
0
h_1
h_o
D_o
d_o
02
03
04
05
06
07
TIME (UTC)
0
50
100
150
200
250
DISTANCE RELATIVE TO GRAVITY CURRENT (KM)
0
100
200
300
400
500
DISTANCE RELATIVE TO BORE (KM)

Fig. 21

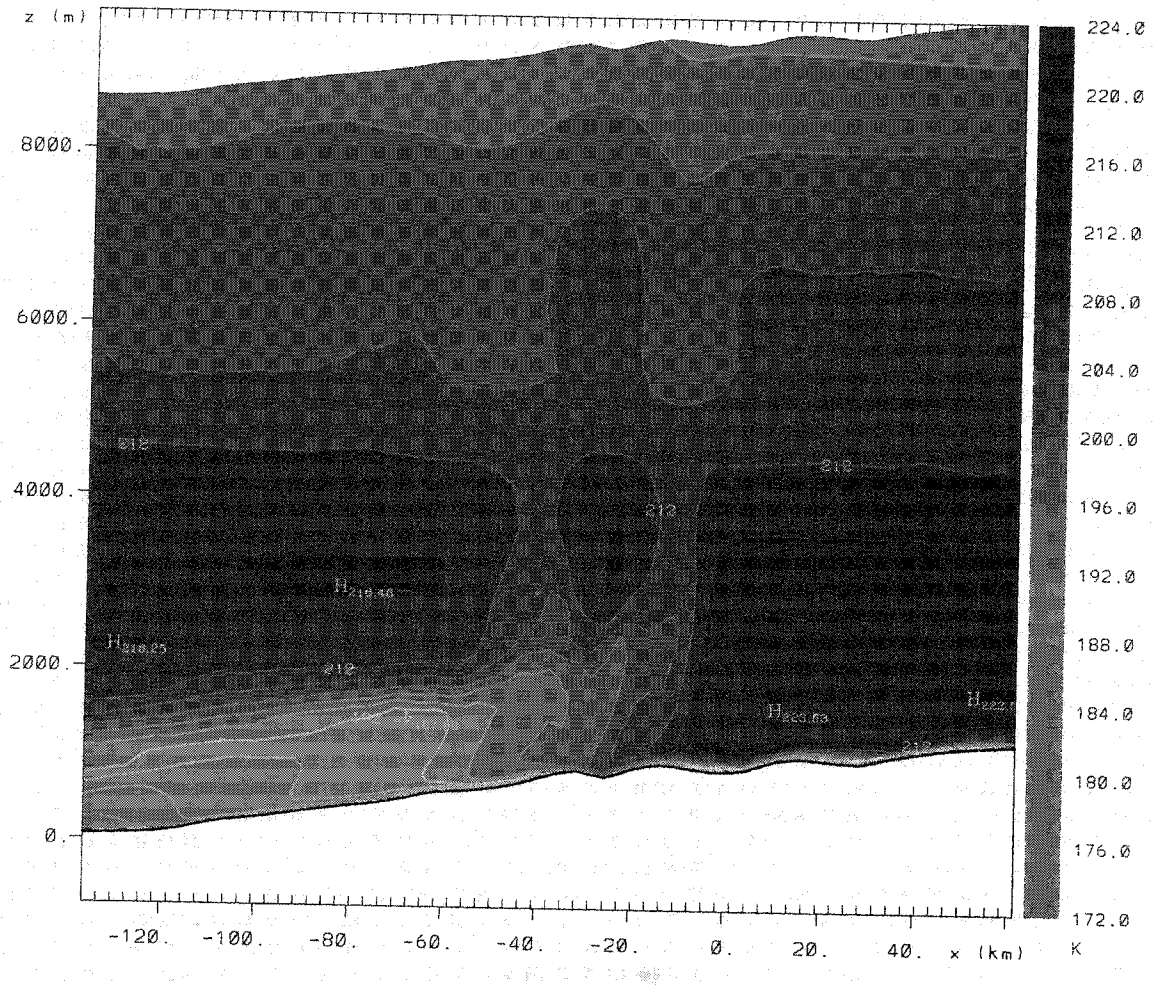
z (m)
8000.
6000.
4000.
2000.
0.
-120.
-100.
-80.
-60.
-40.
-20.
0.
20.
40.
x (km)
224.0
220.0
216.0
212.0
208.0
204.0
200.0
196.0
192.0
188.0
184.0
180.0
176.0
172.0
K

Fig. 22

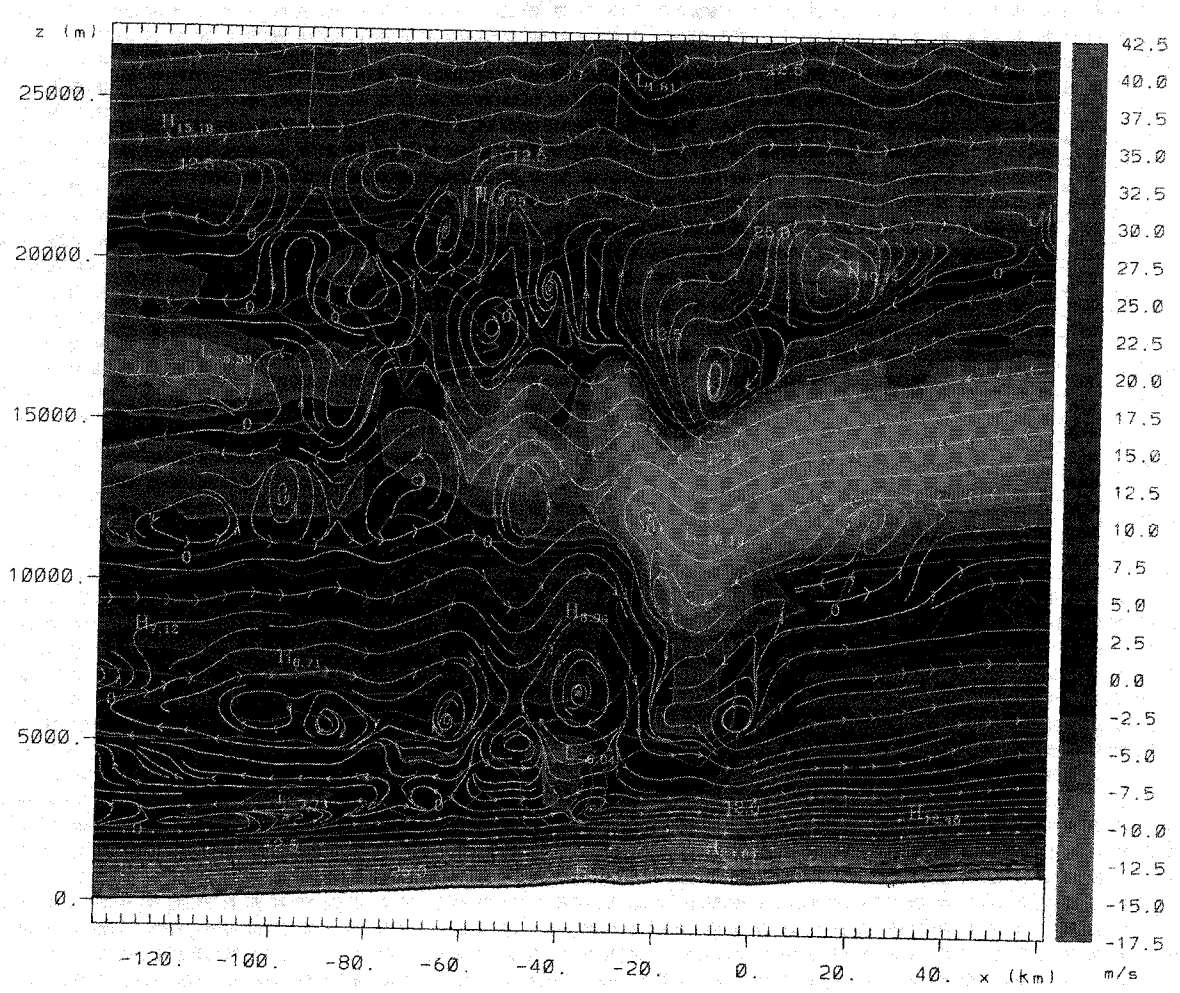
z (m)
25000.
20000.
15000.
10000.
5000.
0.
-120.
-100.
-80.
-60.
-40.
-20.
0.
20.
40.
x (km)
42.5
40.0
37.5
35.0
32.5
30.0
27.5
25.0
22.5
20.0
17.5
15.0
12.5
10.0
7.5
5.0
2.5
0.0
-2.5
-5.0
-7.5
-10.0
-12.5
-15.0
-17.5
m/s

Fig. 23a

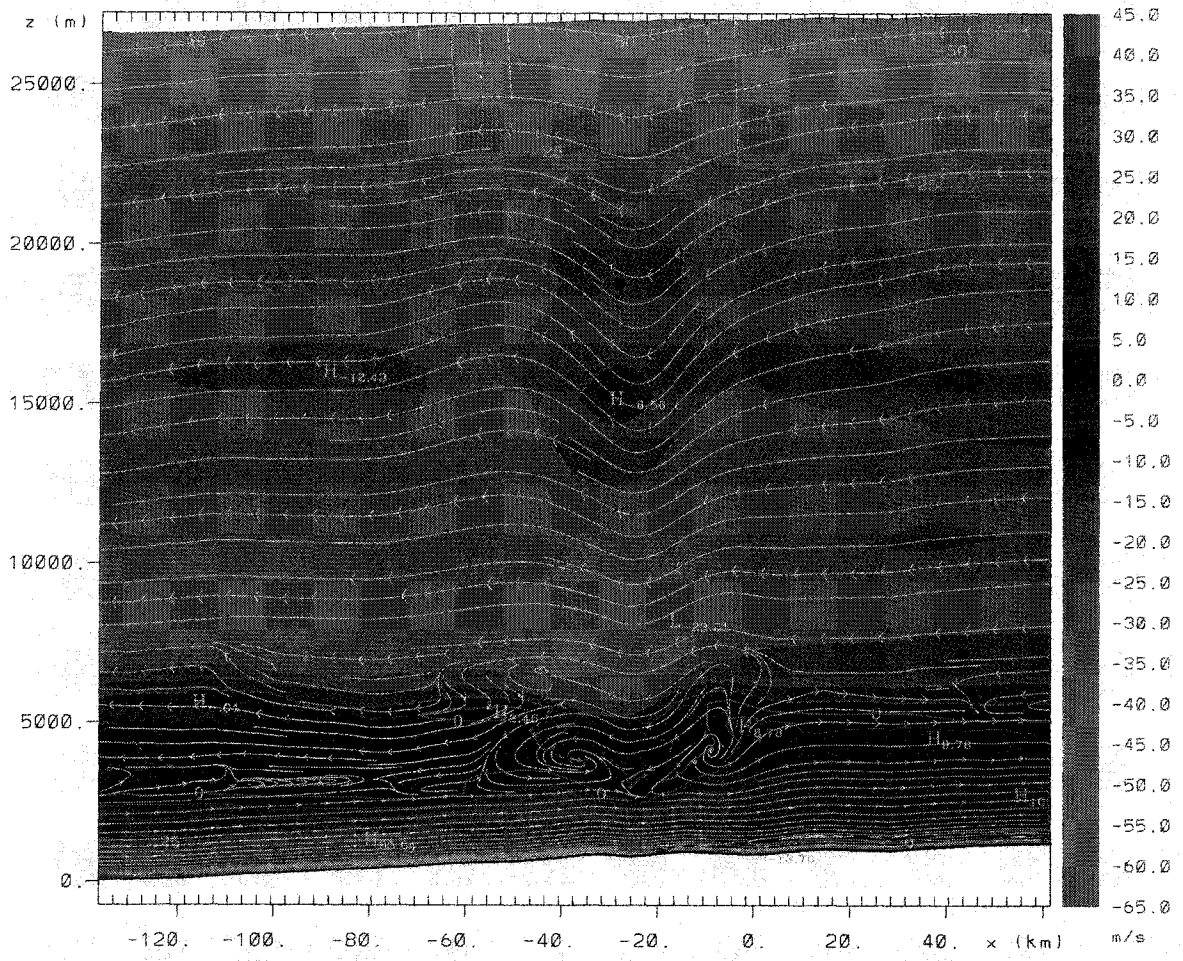
z (m)
25000.
20000.
15000.
10000.
5000.
0.
-120.
-100.
-80.
-60.
-40.
-20.
0.
20.
40.
x (km)
45.0
40.0
35.0
30.0
25.0
20.0
15.0
10.0
5.0
0.0
-5.0
-10.0
-15.0
-20.0
-25.0
-30.0
-35.0
-40.0
-45.0
-50.0
-55.0
-60.0
-65.0
m/s

Fig. 23b

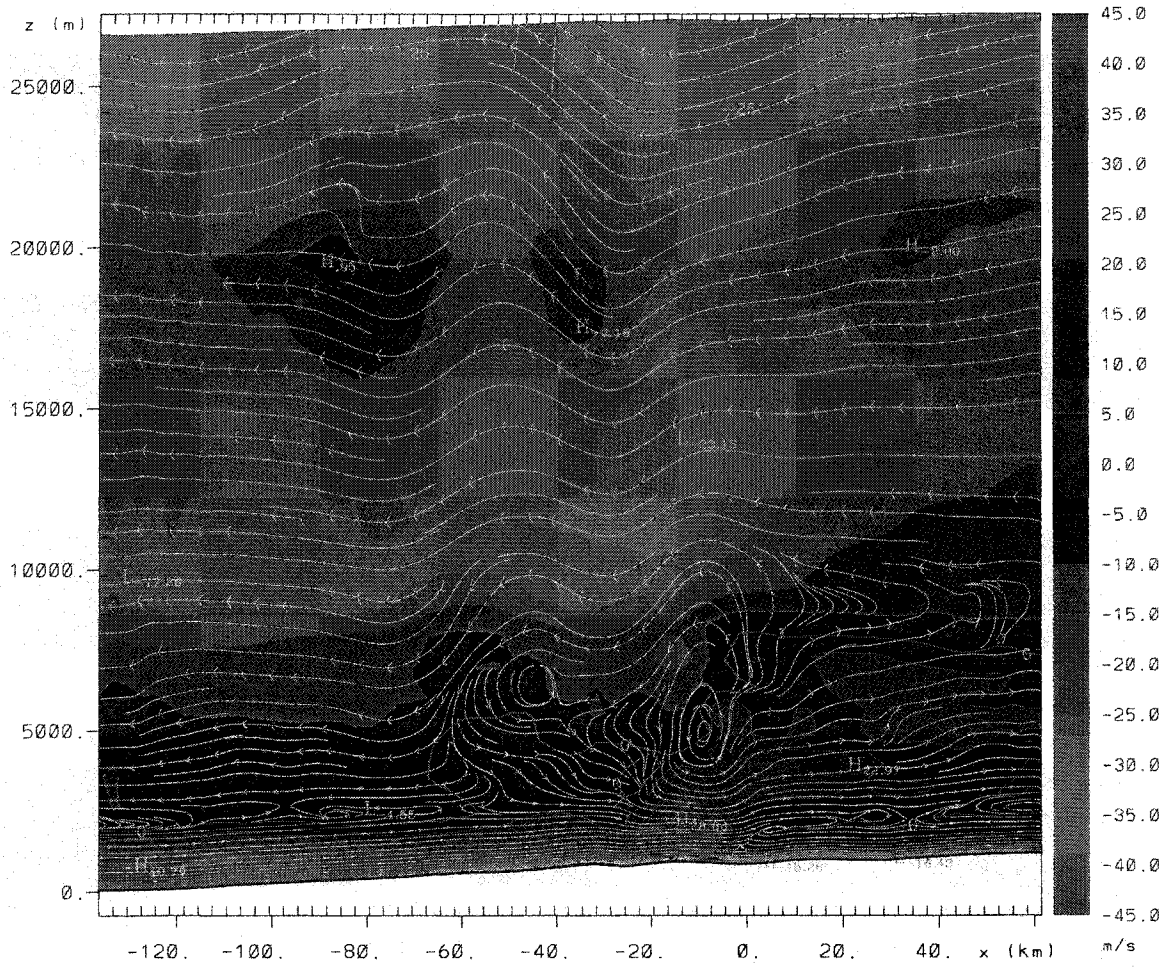
z (m)
25000.
20000.
15000.
10000.
5000.
0.
-120.
-100.
-80.
-60.
-40.
-20.
0.
20.
40.
x (km)
45.0
40.0
35.0
30.0
25.0
20.0
15.0
10.0
5.0
0.0
-5.0
-10.0
-15.0
-20.0
-25.0
-30.0
-35.0
-40.0
-45.0
m/s

Fig. 23c

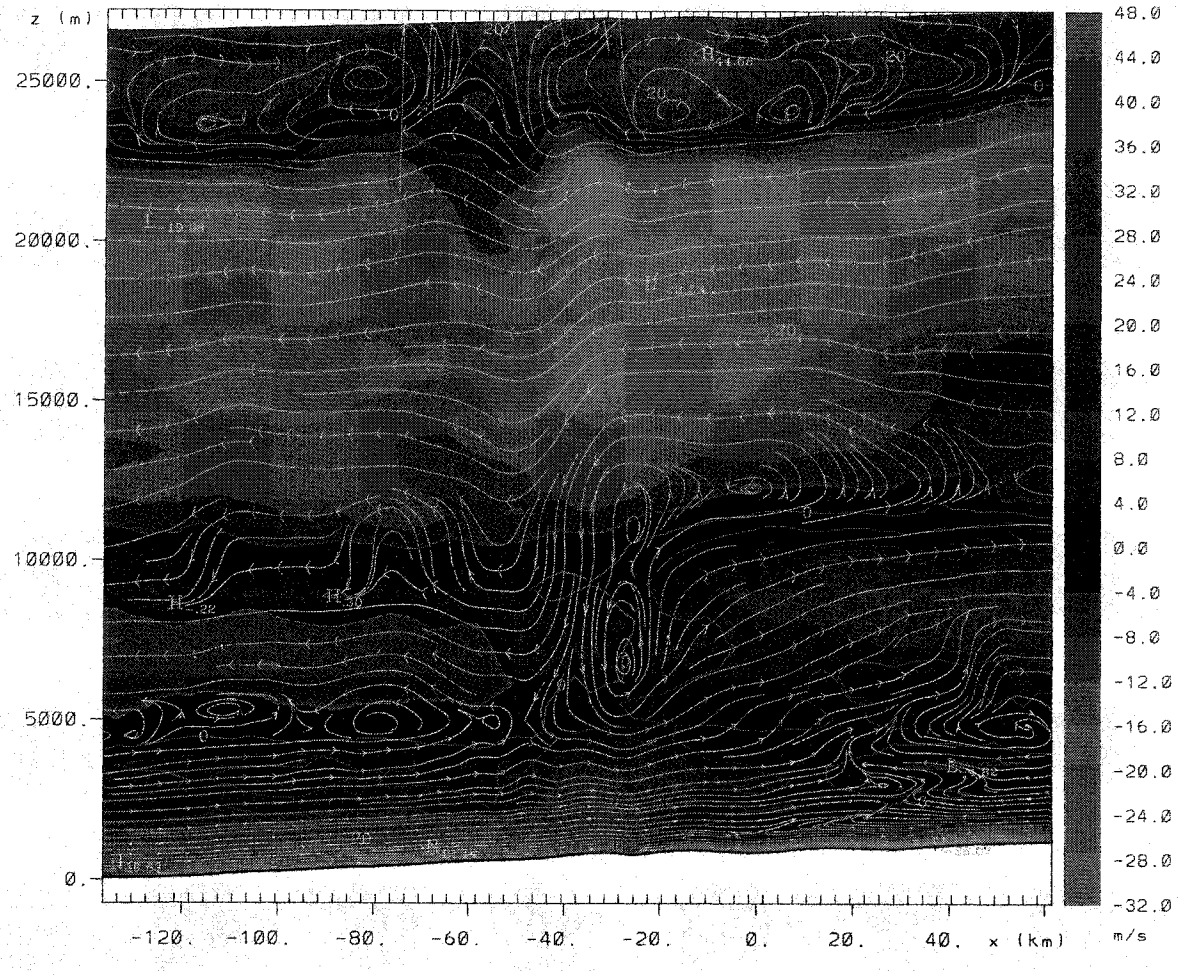
z (m)
25000.
20000.
15000.
10000.
5000.
0.
-120.
-100.
-80.
-60.
-40.
-20.
0.
20.
40.
x (km)
48.0
44.0
40.0
36.0
32.0
28.0
24.0
20.0
16.0
12.0
8.0
4.0
0.0
-4.0
-8.0
-12.0
-16.0
-20.0
-24.0
-28.0
-32.0
m/s

Fig. 23d

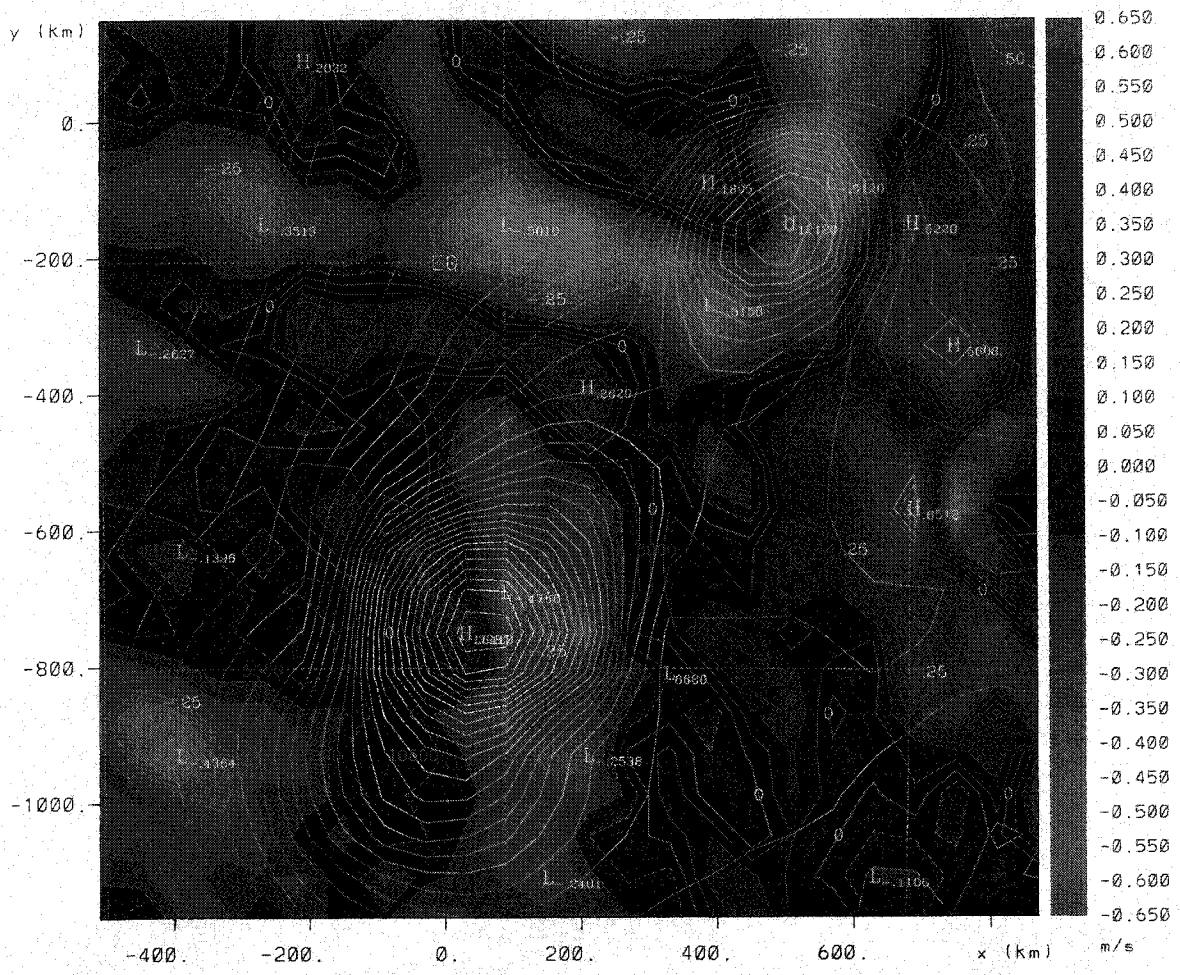
y (km)
0.
-200.
-400.
-600.
-800.
-1000.
-400.
-200.
0.
200.
400.
600.
x (km)
m/s
0.650
0.600
0.550
0.500
0.450
0.400
0.350
0.300
0.250
0.200
0.150
0.100
0.050
0.000
-0.050
-0.100
-0.150
-0.200
-0.250
-0.300
-0.350
-0.400
-0.450
-0.500
-0.550
-0.600
-0.650

Fig. 24

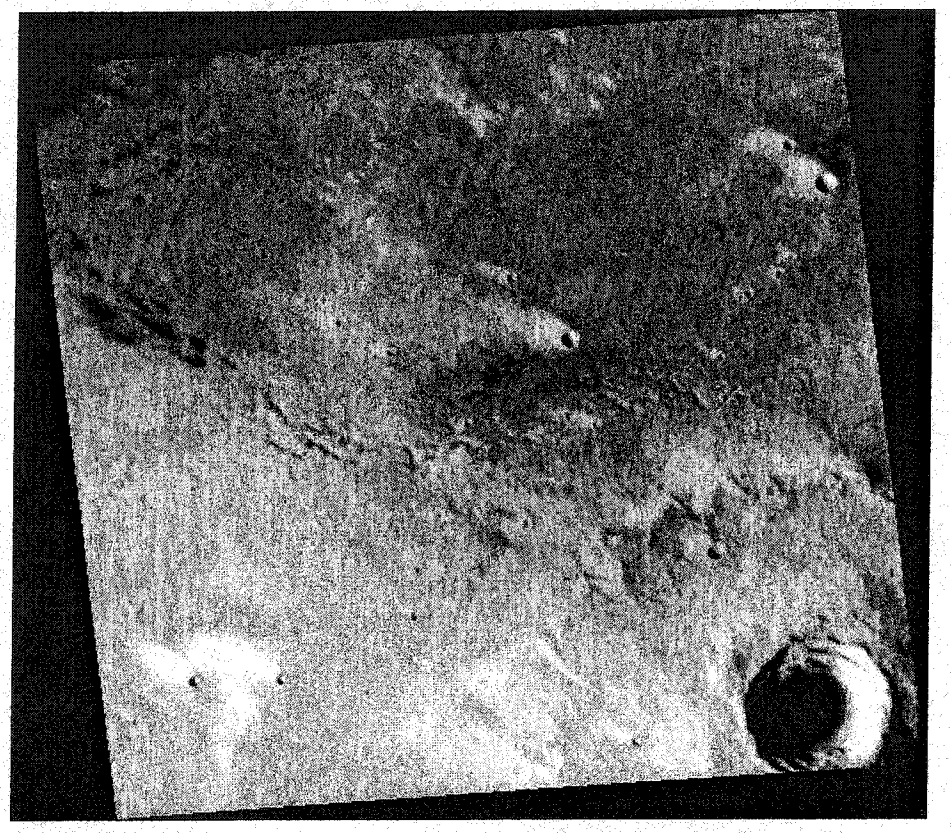

Fig. 25

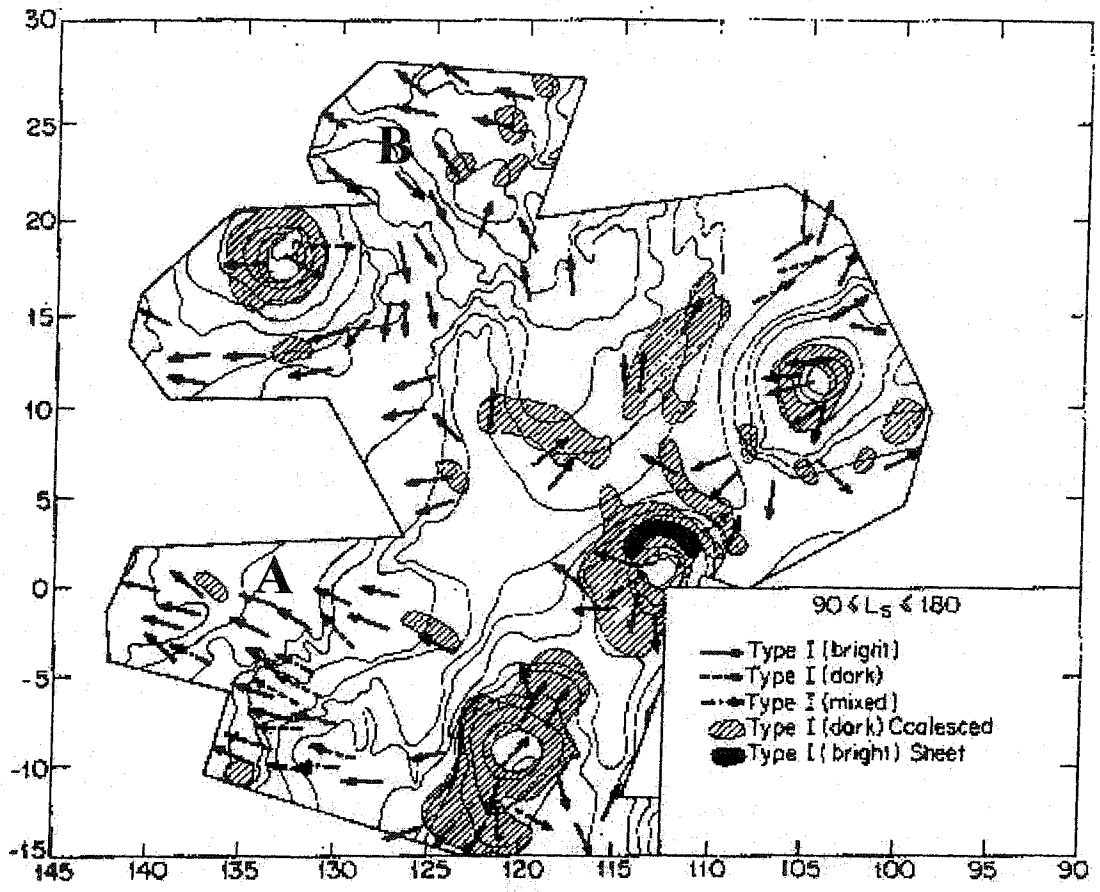
30
25
20
15
10
5
0
-5
-10
-15
145
140
135
130
125
120
115
110
105
100
95
90
B
A
90 ≤ Ls ≤ 180
Type I (bright)
Type I (dark)
Type I (mixed)
Type I (dark) Coalesced
Type I (bright) Sheet

Fig. 26a

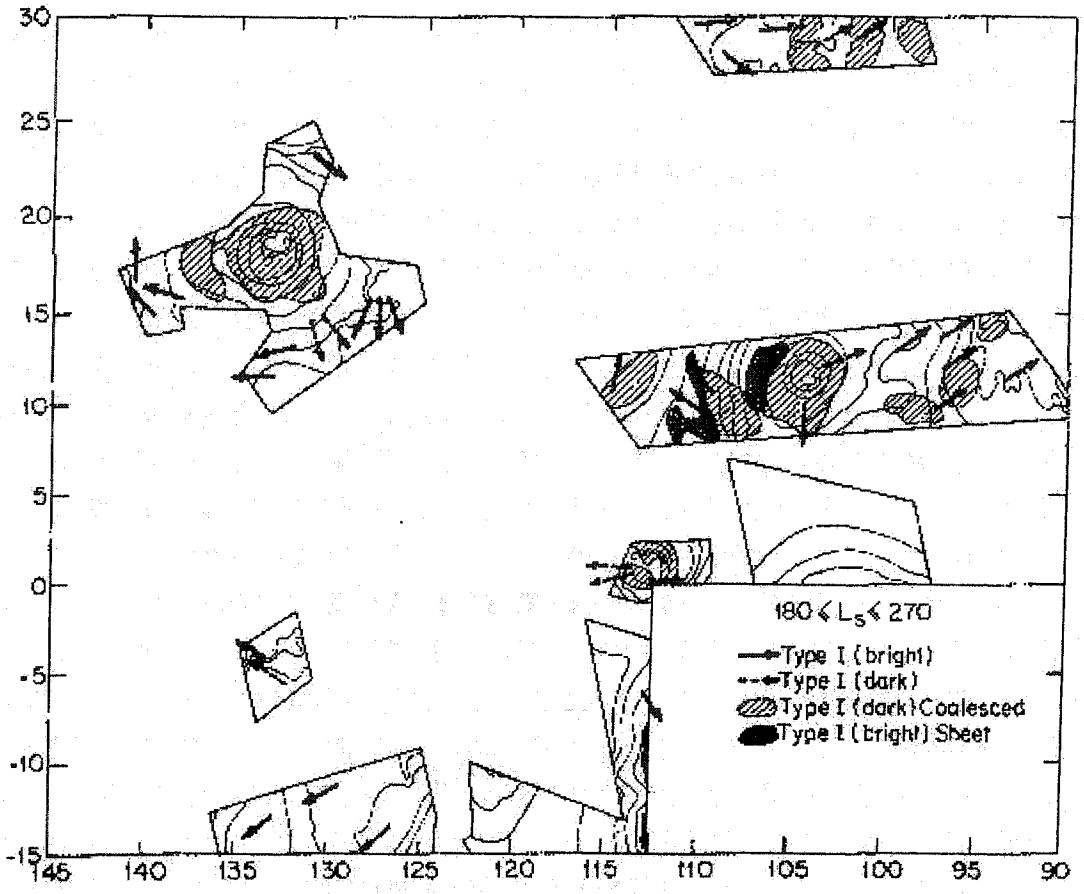
30
25
20
15
10
5
0
-5
-10
-15
145
140
135
130
125
120
115
110
105
100
95
90
180 < Ls < 270
Type I (bright)
Type I (dark)
Type I (dark) Coalesced
Type I (bright) Sheet

Fig. 26b

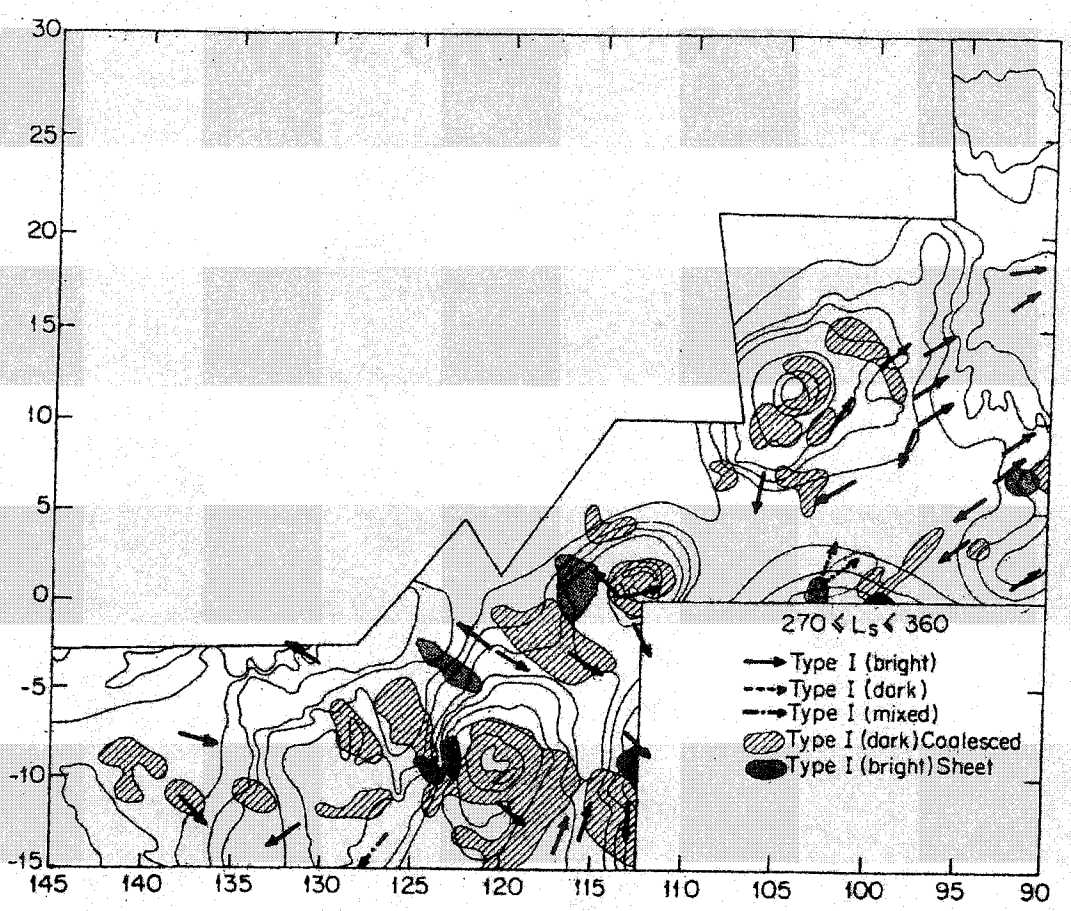
30
25
20
15
10
5
0
-5
-10
-15
145
140
135
130
125
120
115
110
105
100
95
90
270 ≤ Ls ≤ 360
Type I (bright)
Type I (dark)
Type I (mixed)
Type I (dark) Coalesced
Type I (bright) Sheet

Fig. 26c

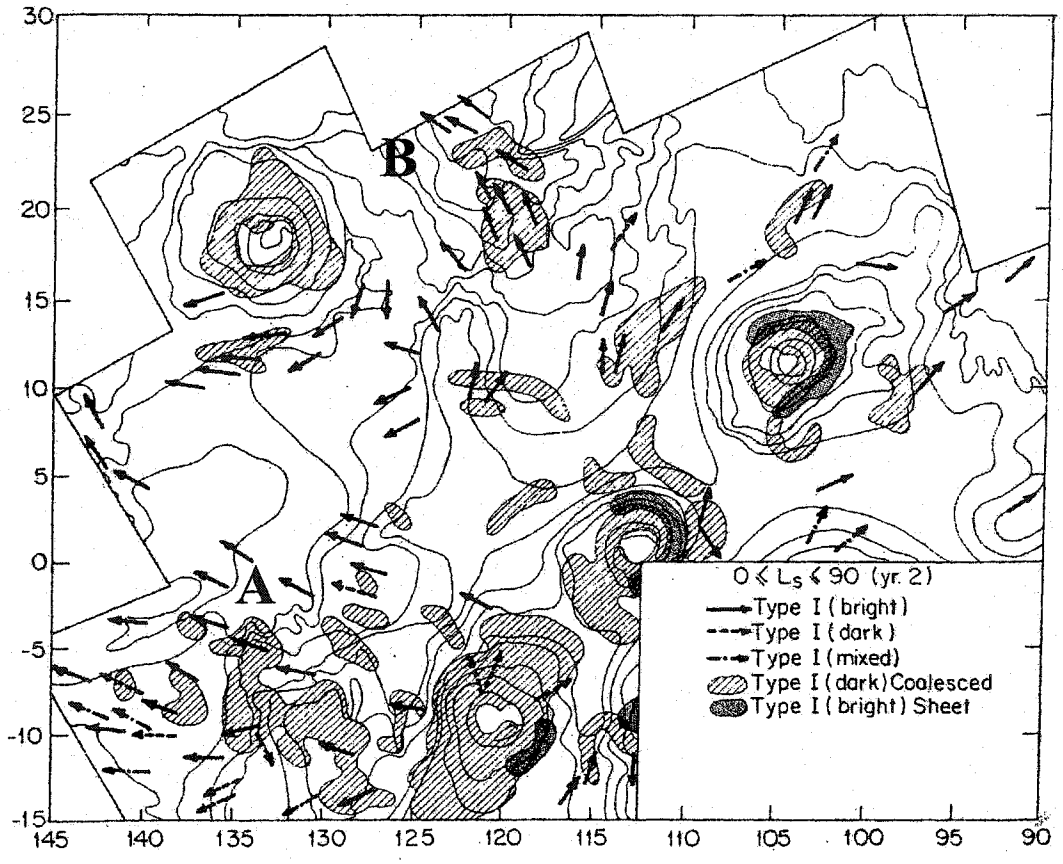
30
25
20
15
10
5
0
-5
-10
-15
145
140
135
130
125
120
115
110
105
100
95
90
B
A
0 ≤ Ls ≤ 90 (yr. 2)
Type I (bright)
Type I (dark)
Type I (mixed)
Type I (dark) Coalesced
Type I (bright) Sheet

Fig. 26d

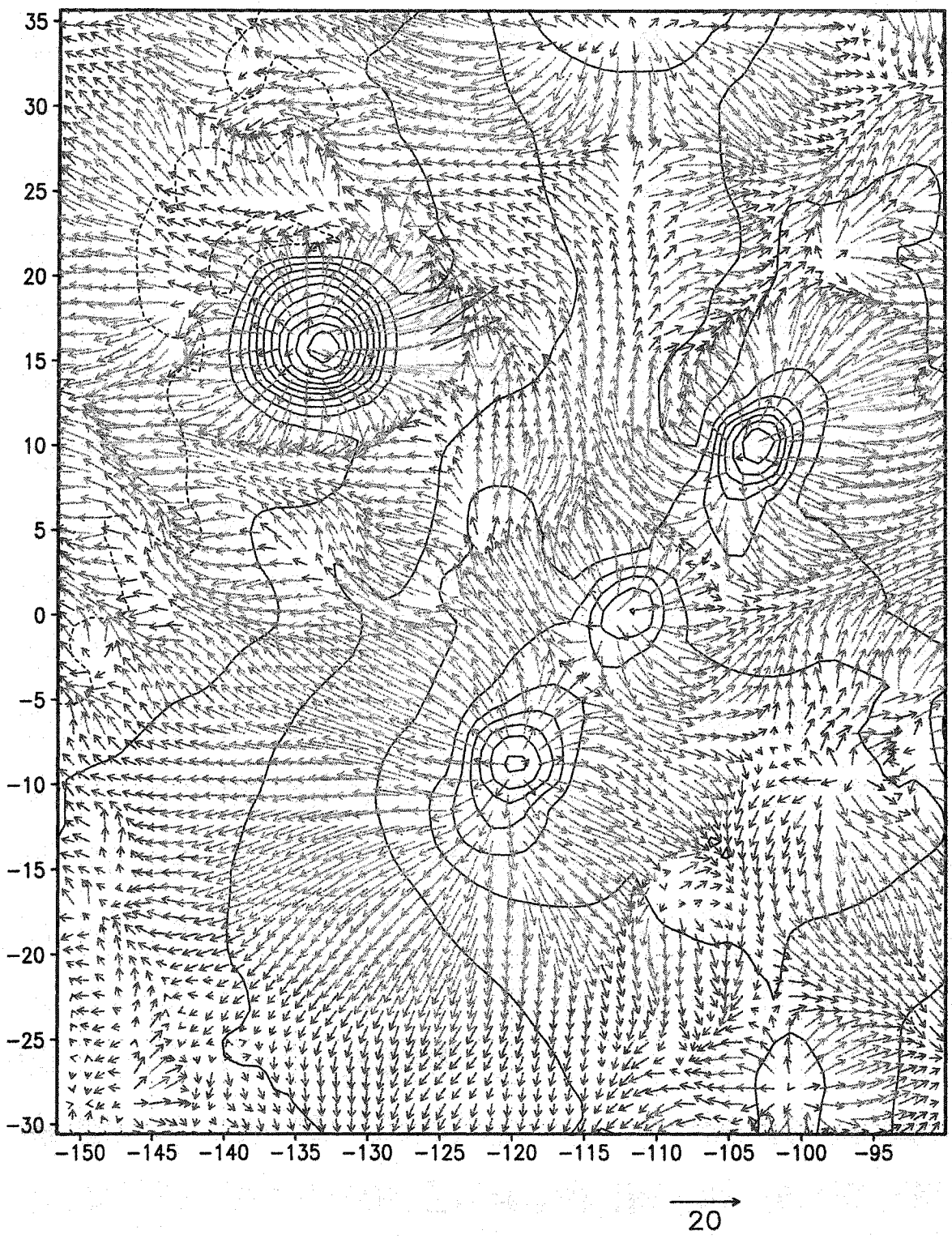
35
30
25
20
15
10
5
0
−5
−10
−15
−20
−25
−30
−150 −145 −140 −135 −130 −125 −120 −115 −110 −105 −100 −95
20

Fig. 27a

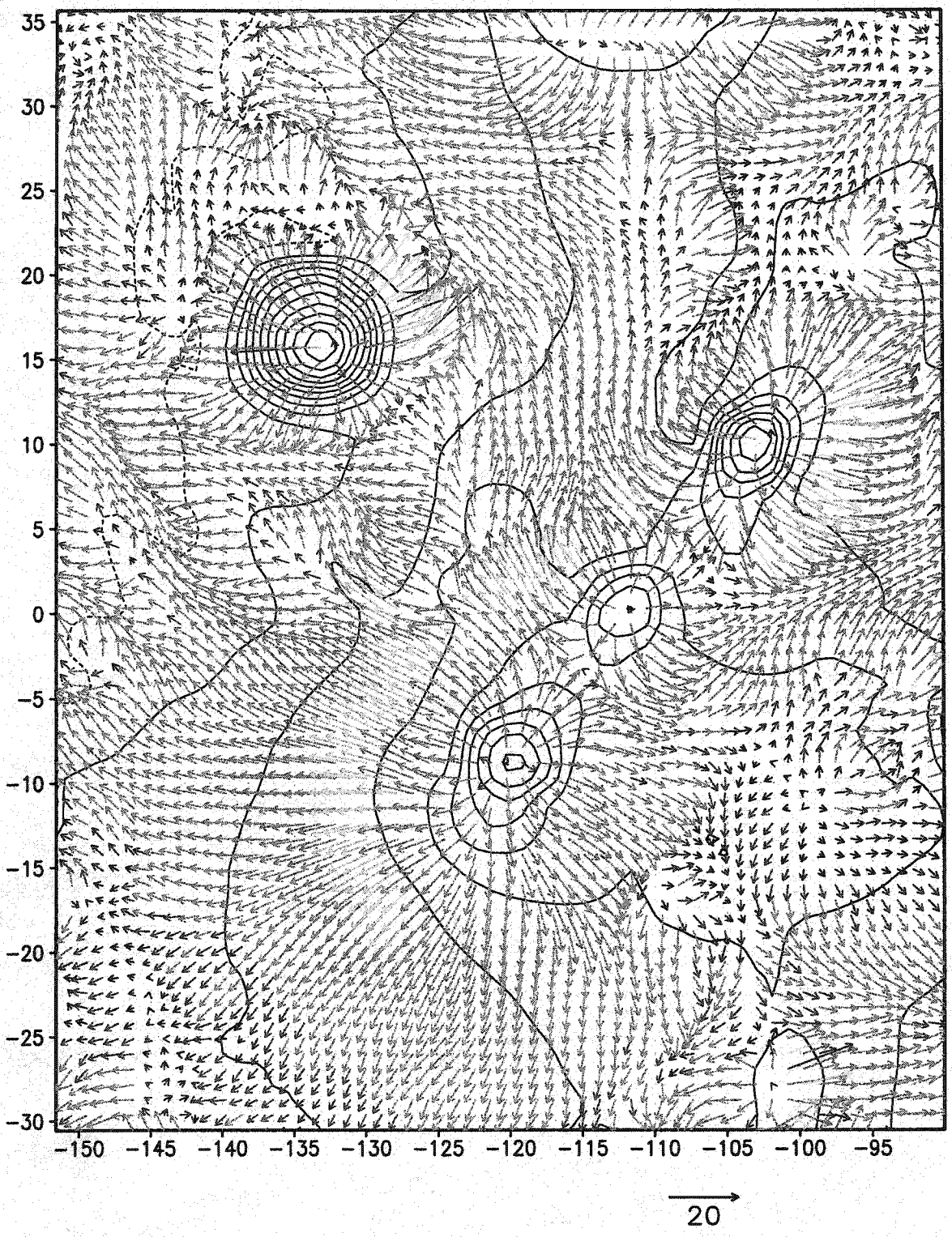
35
30
25
20
15
10
5
0
−5
−10
−15
−20
−25
−30
−150 −145 −140 −135 −130 −125 −120 −115 −110 −105 −100 −95
20

Fig. 27b

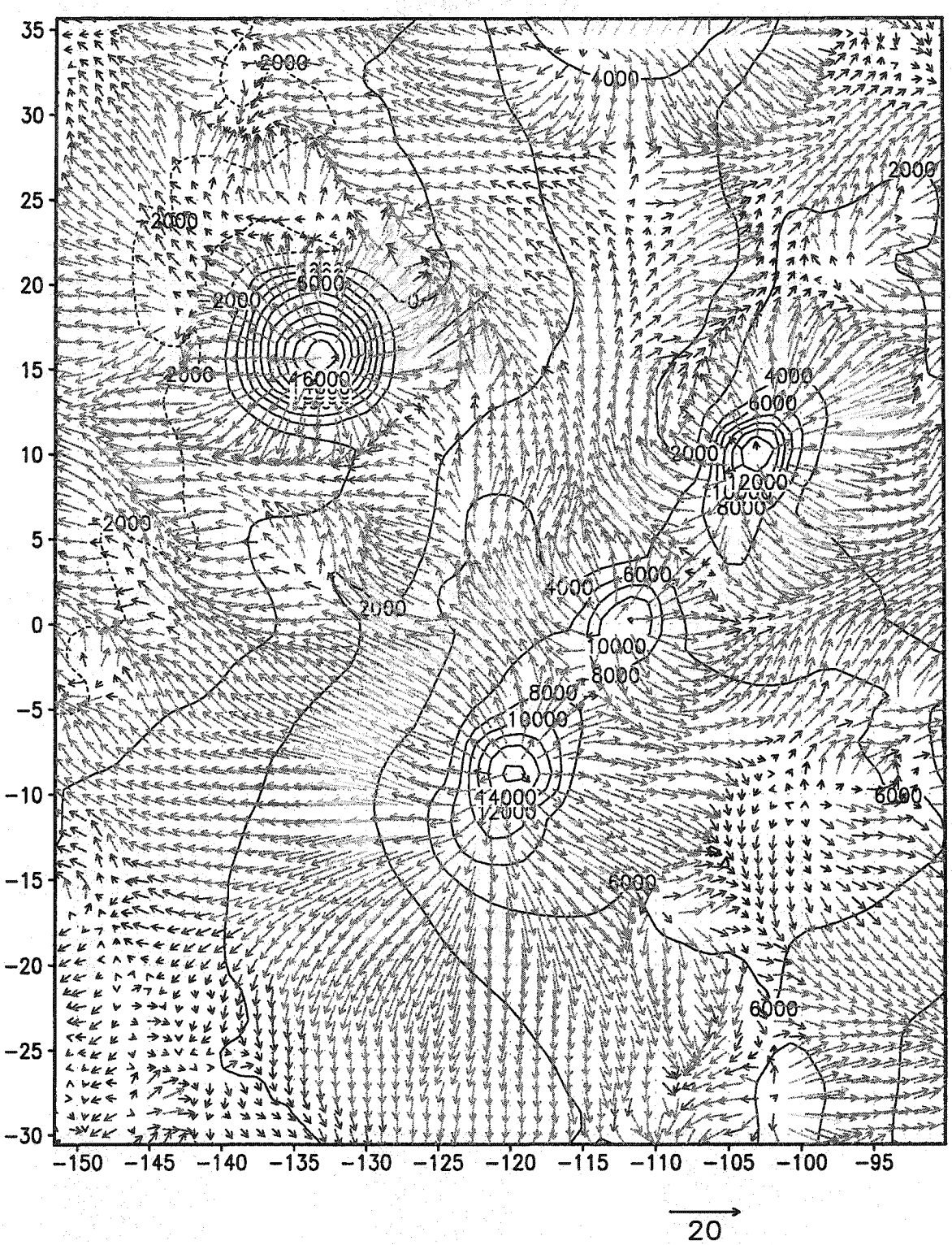
35
30
25
20
15
10
5
0
−5
−10
−15
−20
−25
−30
−150
−145
−140
−135
−130
−125
−120
−115
−110
−105
−100
−95
2000
4000
6000
8000
10000
12000
14000
16000
20

Fig. 27c

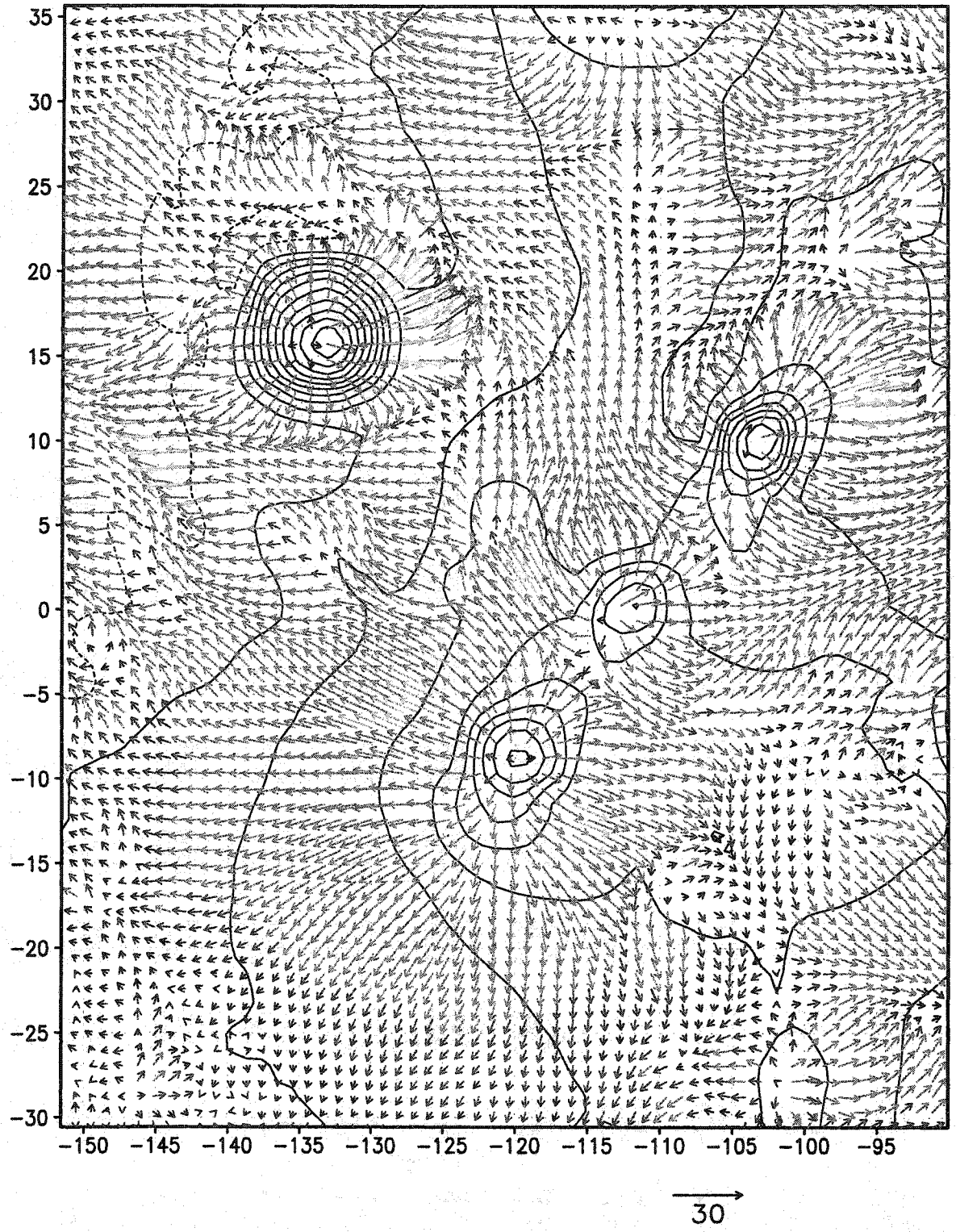
35
30
25
20
15
10
5
0
−5
−10
−15
−20
−25
−30
−150
−145
−140
−135
−130
−125
−120
−115
−110
−105
−100
−95
30

Fig. 27d

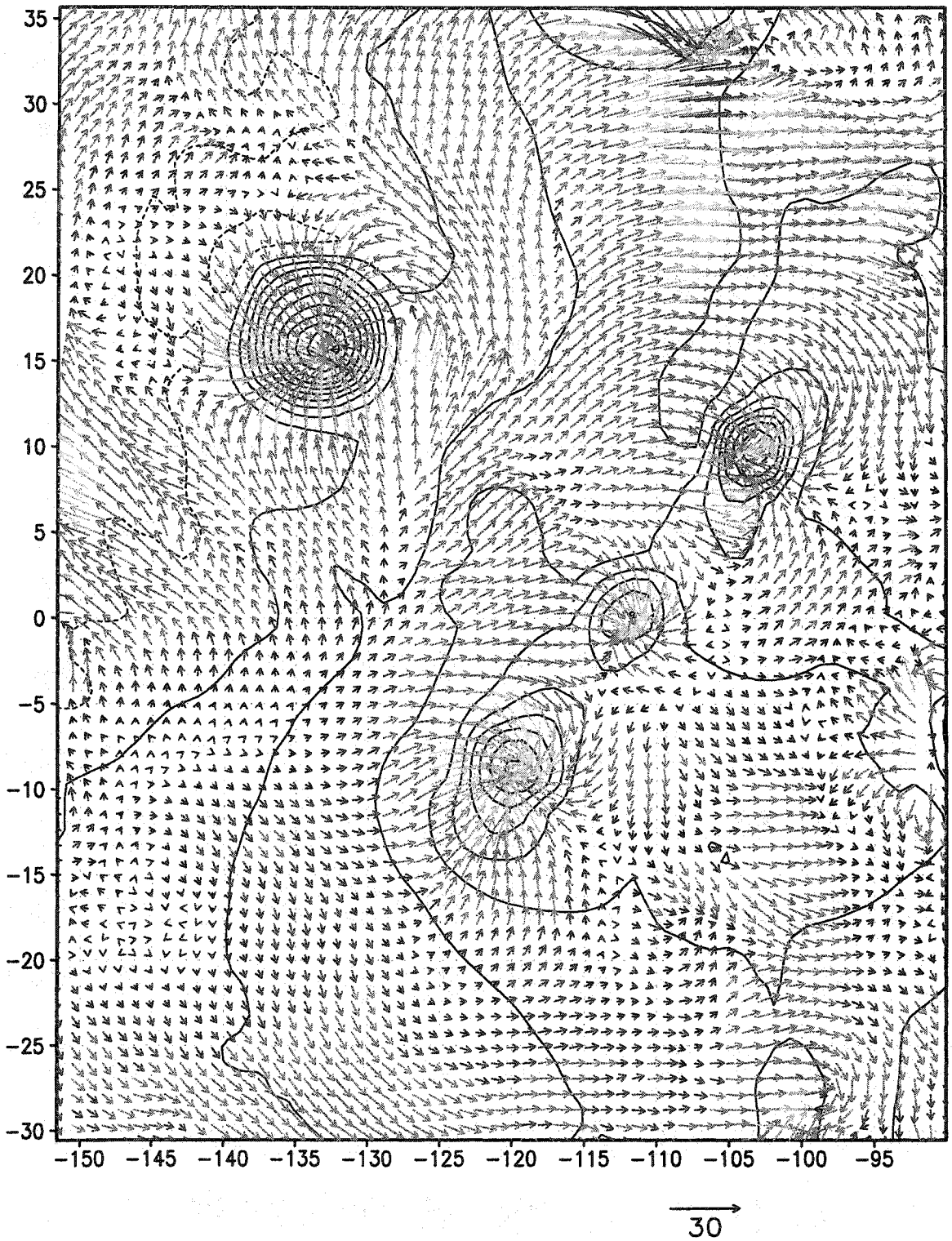
35
30
25
20
15
10
5
0
−5
−10
−15
−20
−25
−30
−150 −145 −140 −135 −130 −125 −120 −115 −110 −105 −100 −95
30

Fig. 28a

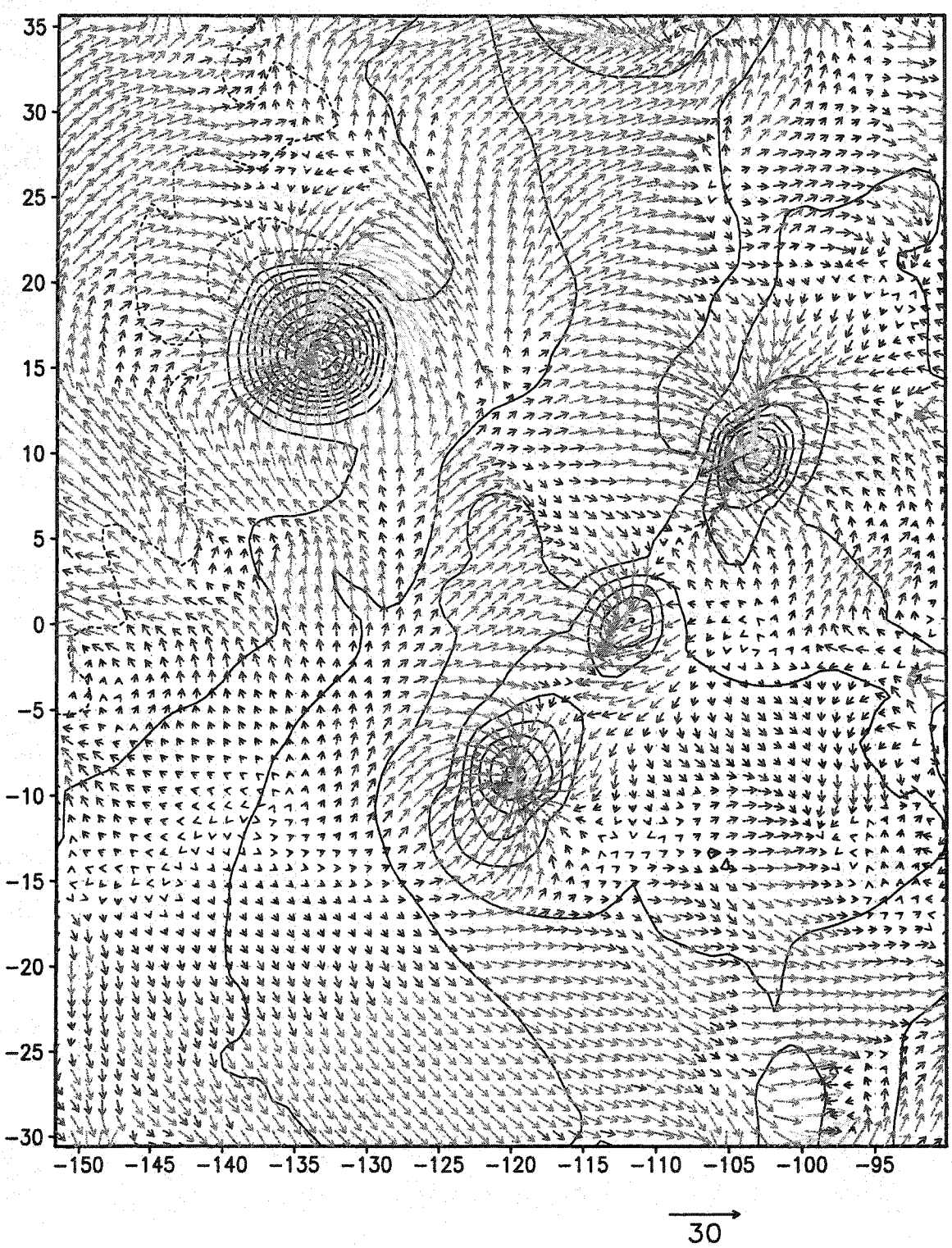
35
30
25
20
15
10
5
0
−5
−10
−15
−20
−25
−30
−150 −145 −140 −135 −130 −125 −120 −115 −110 −105 −100 −95
30

Fig. 28b

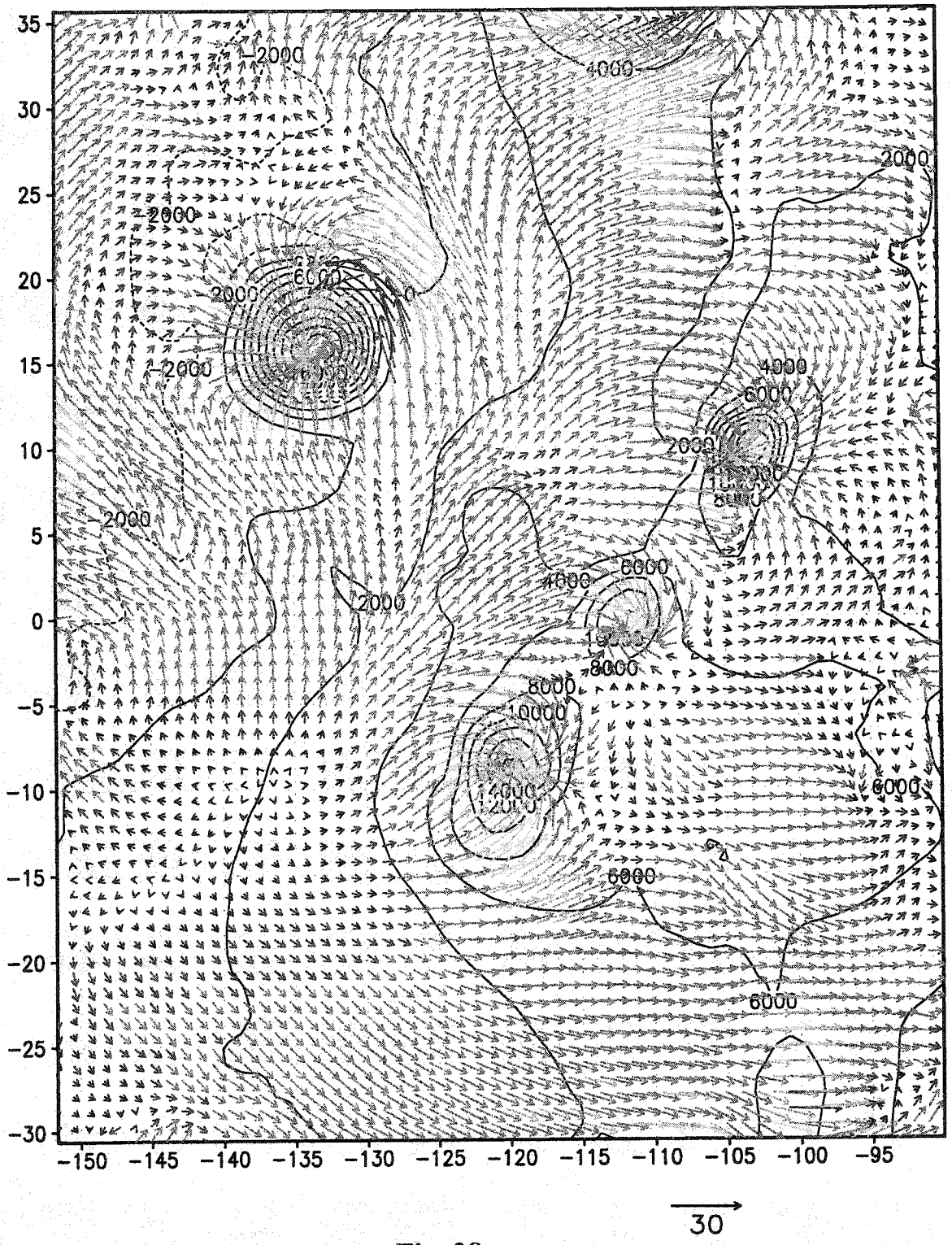
35
30
25
20
15
10
5
0
−5
−10
−15
−20
−25
−30
−150 −145 −140 −135 −130 −125 −120 −115 −110 −105 −100 −95
2000
4000
6000
8000
10000
30

Fig. 28c

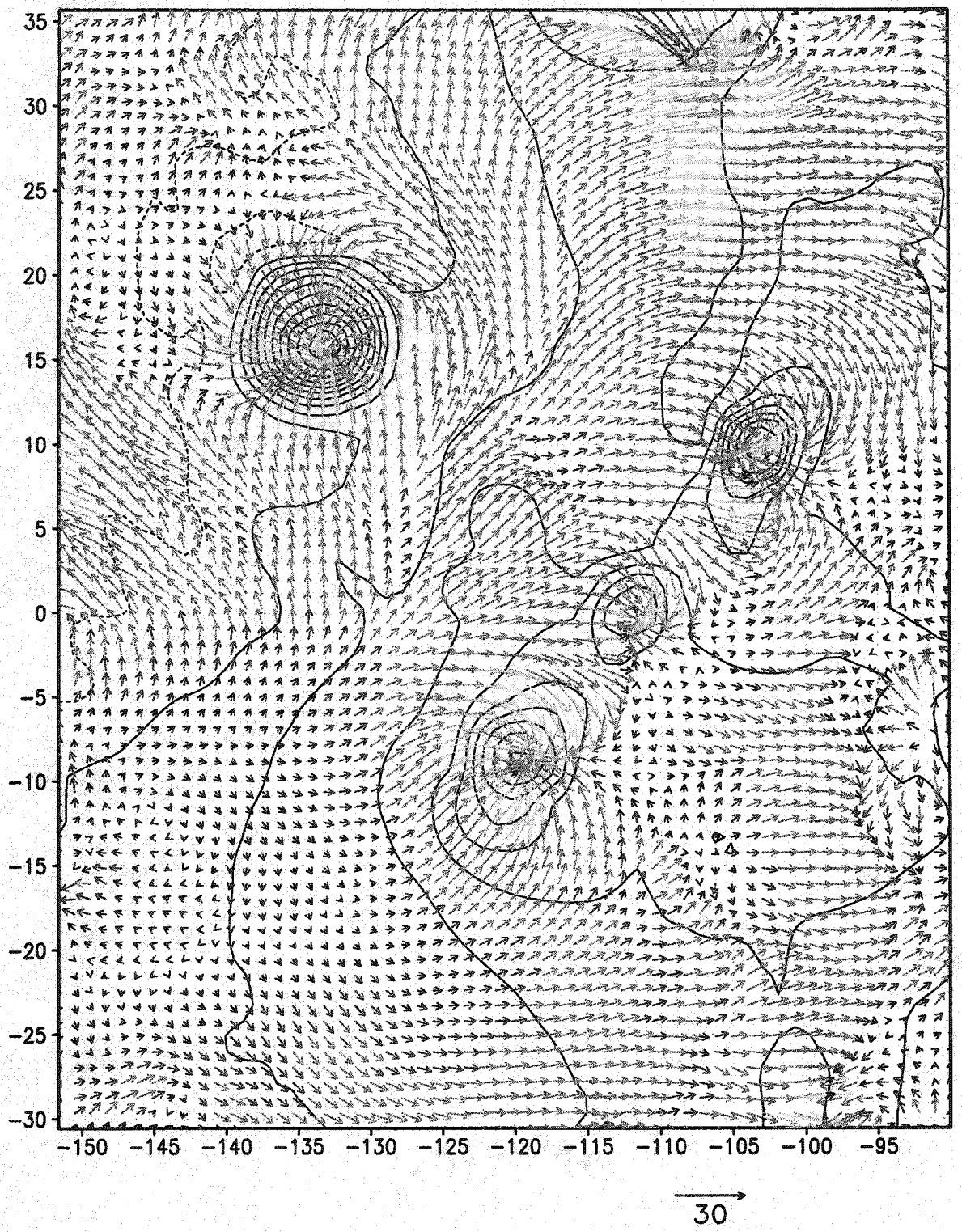
35
30
25
20
15
10
5
0
−5
−10
−15
−20
−25
−30
−150
−145
−140
−135
−130
−125
−120
−115
−110
−105
−100
−95
30

Fig. 28d

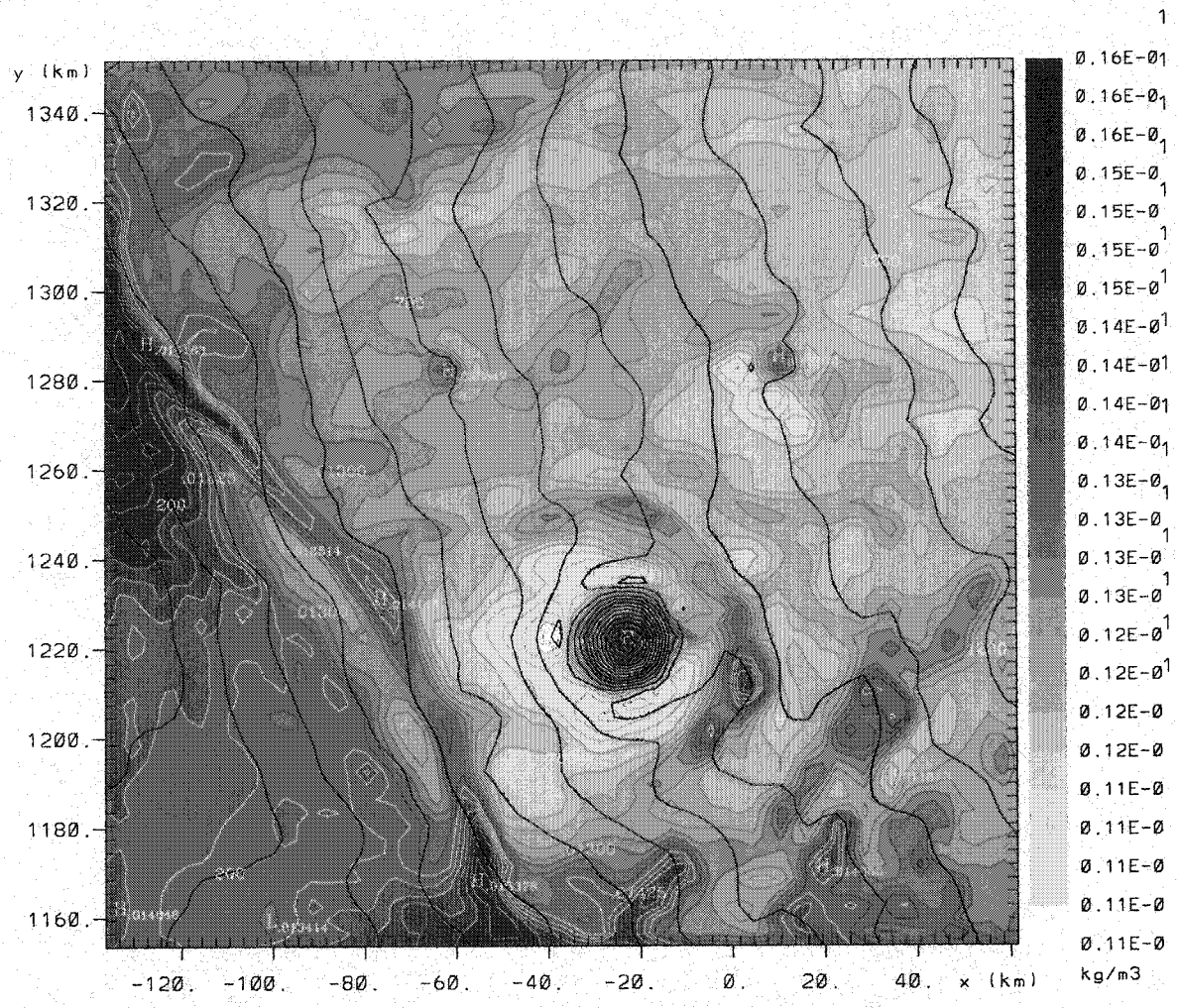
y (km)
1340.
1320.
1300.
1280.
1260.
1240.
1220.
1200.
1180.
1160.
-120.
-100.
-80.
-60.
-40.
-20.
0.
20.
40.
x (km)
1
0.16E-01
0.16E-01
0.16E-01
0.15E-01
0.15E-01
0.15E-01
0.15E-01
0.14E-01
0.14E-01
0.14E-01
0.14E-01
0.13E-01
0.13E-01
0.13E-01
0.13E-01
0.12E-01
0.12E-01
0.12E-01
0.12E-01
0.11E-01
0.11E-01
0.11E-01
0.11E-01
kg/m3

Fig. 29a

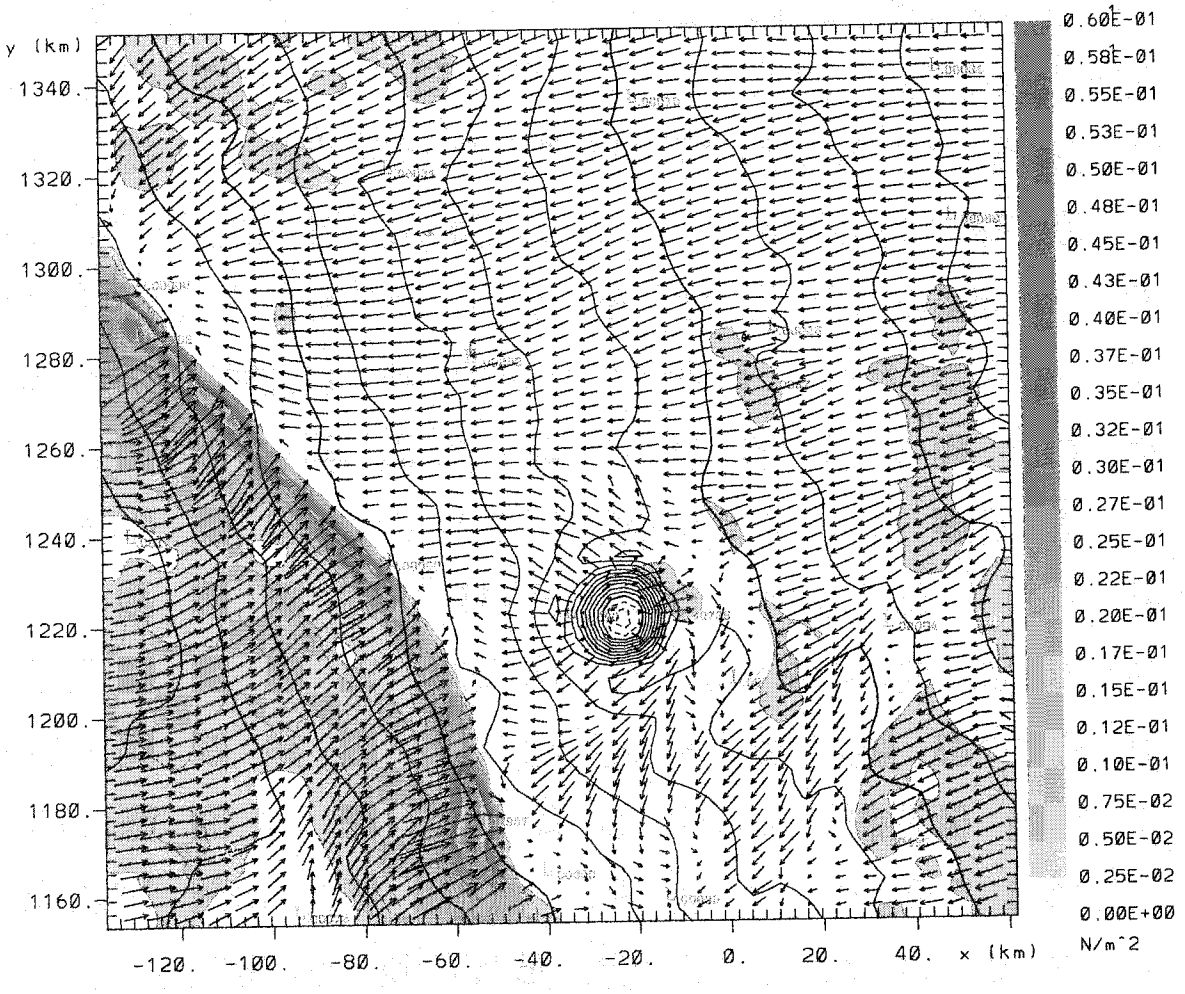
y (km)
1340.
1320.
1300.
1280.
1260.
1240.
1220.
1200.
1180.
1160.
-120.
-100.
-80.
-60.
-40.
-20.
0.
20.
40.
x (km)
0.60E-01
0.58E-01
0.55E-01
0.53E-01
0.50E-01
0.48E-01
0.45E-01
0.43E-01
0.40E-01
0.37E-01
0.35E-01
0.32E-01
0.30E-01
0.27E-01
0.25E-01
0.22E-01
0.20E-01
0.17E-01
0.15E-01
0.12E-01
0.10E-01
0.75E-02
0.50E-02
0.25E-02
0.00E+00
N/m^2

Fig. 29b

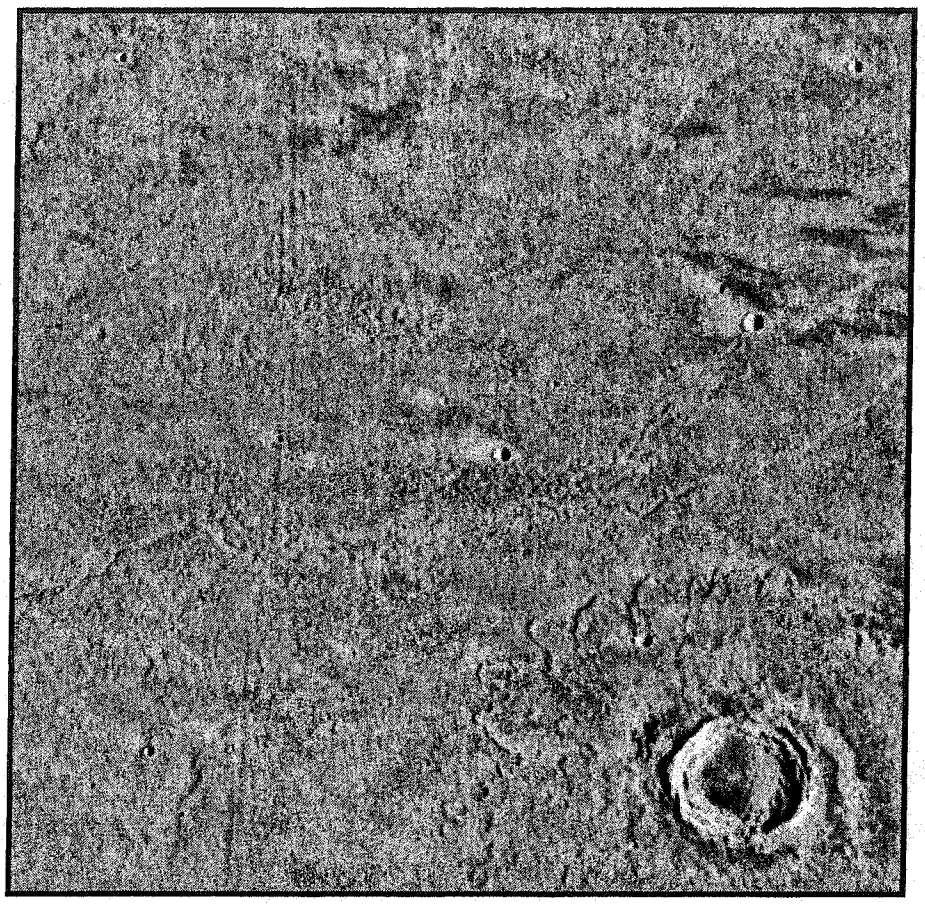

Fig. 30

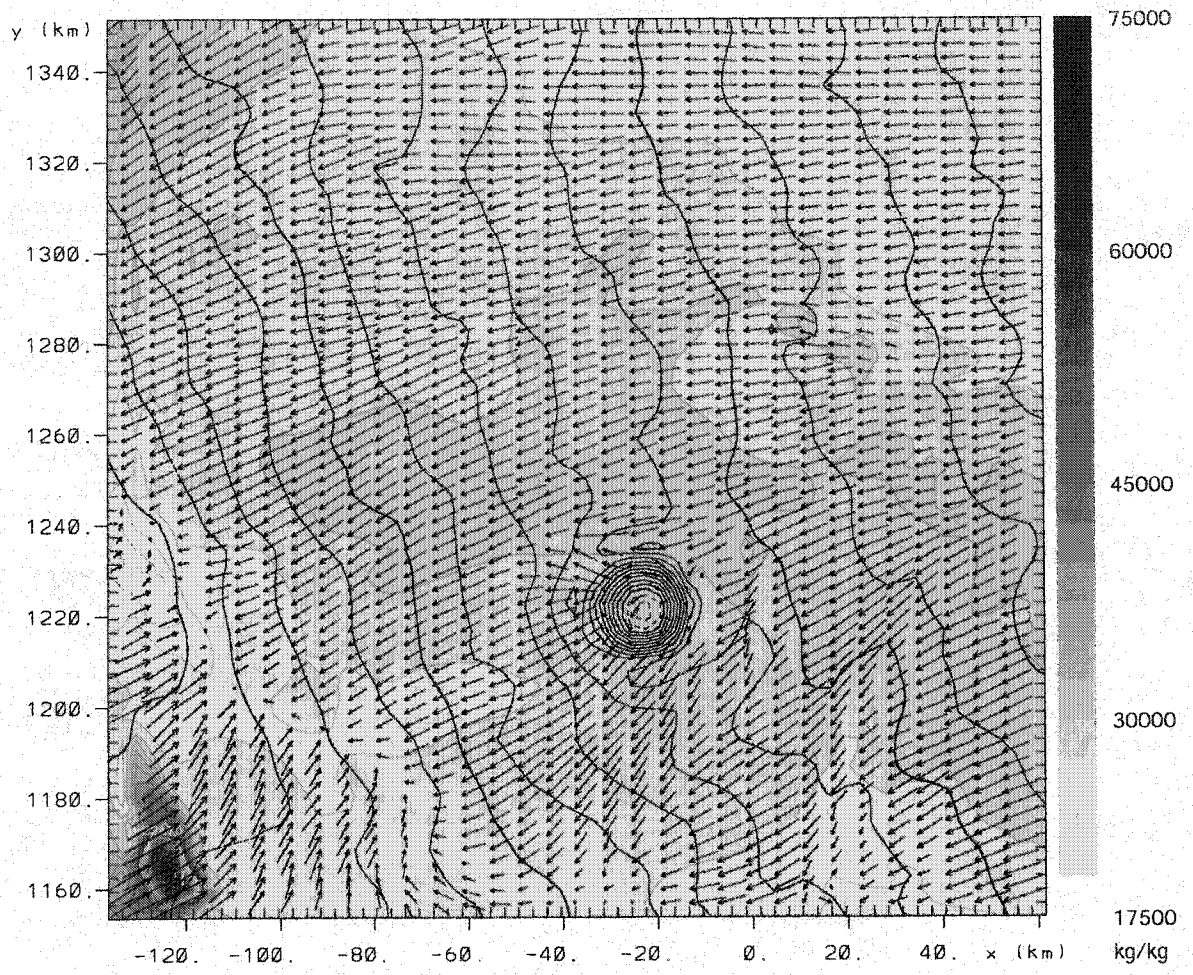
y (km)
1340.
1320.
1300.
1280.
1260.
1240.
1220.
1200.
1180.
1160.
-120.
-100.
-80.
-60.
-40.
-20.
0.
20.
40.
x (km)
75000
60000
45000
30000
17500
kg/kg

Fig. 31a

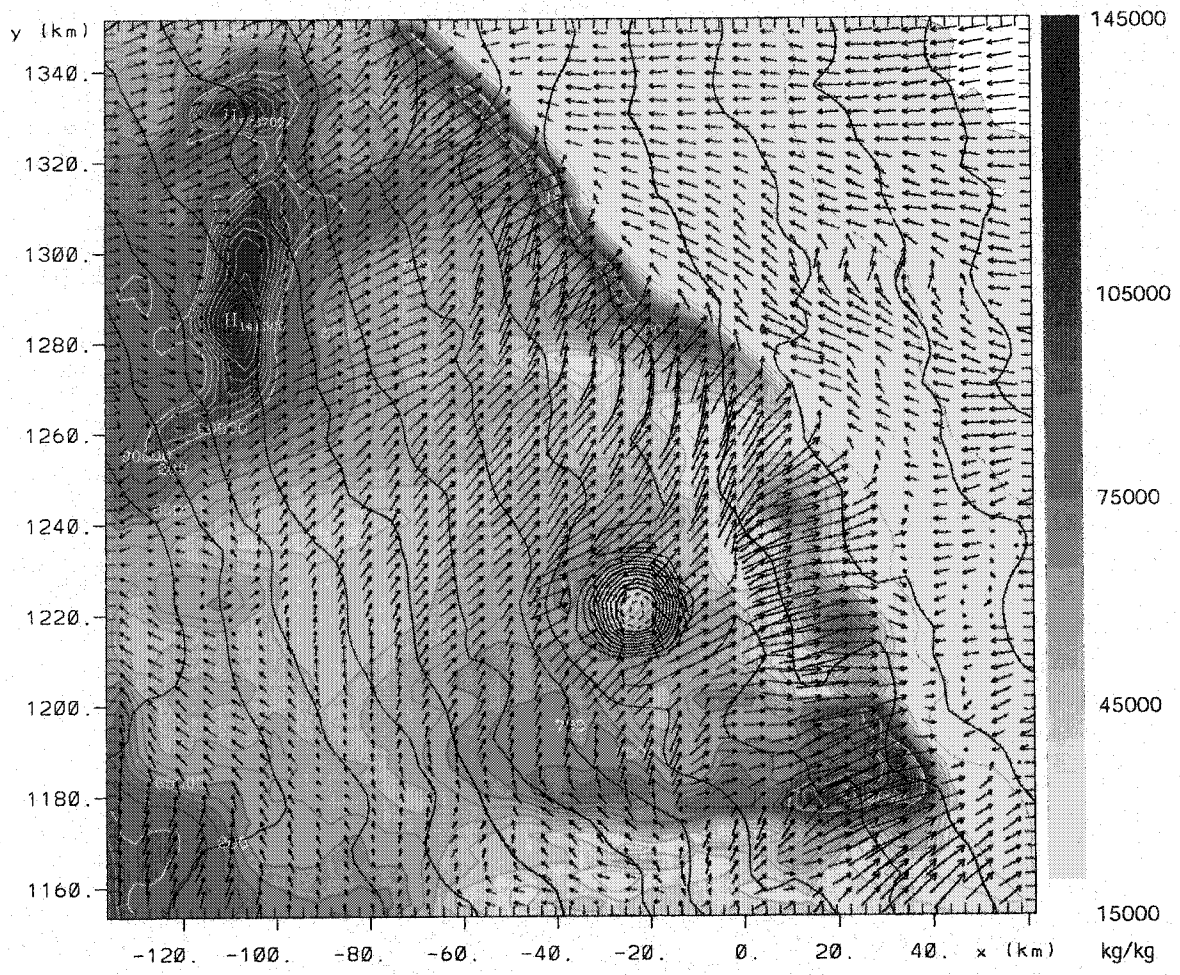
y (km)
1340.
1320.
1300.
1280.
1260.
1240.
1220.
1200.
1180.
1160.
-120.
-100.
-80.
-60.
-40.
-20.
0.
20.
40.
x (km)
145000
105000
75000
45000
15000
kg/kg

Fig. 31b

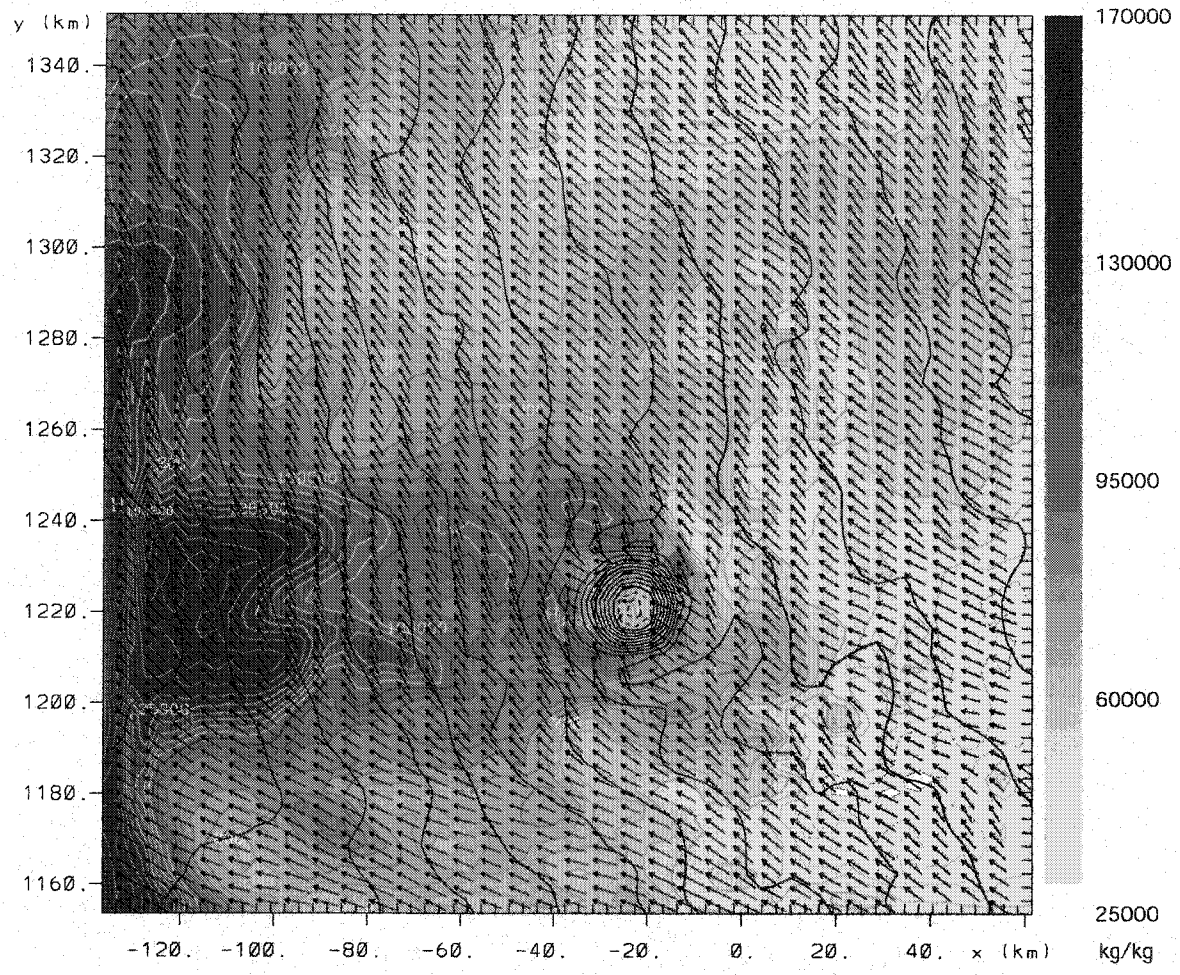
y (km)
1340.
1320.
1300.
1280.
1260.
1240.
1220.
1200.
1180.
1160.
-120.
-100.
-80.
-60.
-40.
-20.
0.
20.
40.
x (km)
170000
130000
95000
60000
25000
kg/kg

Fig. 31c